UNIVERSITAT DE BARCELONA

Monitoring the subsurface elastic properties using ambient seismic noise: 2011 El Hierro eruption and Reykjanes geothermal reservoir

Pilar Sánchez Sánchez-Pastor

Monitoring subsurface elastic properties using ambient seismic noise: 2011 El Hierro eruption and Reykjanes geothermal reservoir

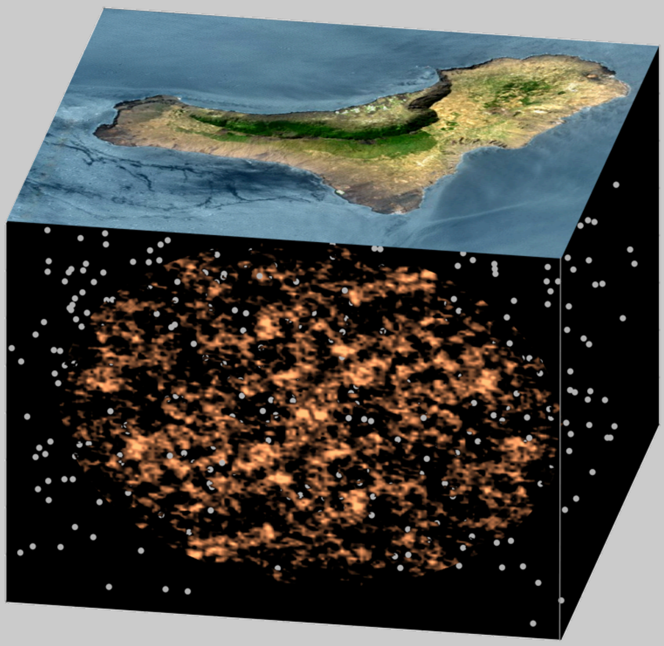

Pilar Sánchez Sánchez-Pastor

Department of Earth and Ocean Dynamics

Universitat de Barcelona

A thesis submitted for the degree of

Doctor of Earth Science

Barcelona, May 2019

CSIC
CONSEJO SUPERIOR DE INVESTIGACIONES CIENTÍFICAS

ICTJA
INSTITUT DE CIÈNCIES DE LA TERRA JAUME ALMERA

UNIVERSITAT DE BARCELONA

Monitoring the subsurface elastic properties using ambient seismic noise: 2011 El Hierro eruption and Reykjanes geothermal reservoir

A dissertation submitted to

Doctorate Program in Earth Sciences

Universitat de Barcelona

for the degree of

Doctor of Earth Sciences

presented by

Pilar Sánchez Sánchez-Pastor

Supervisors

Dr. Jordi Díaz Cusí

Institute of Earth Sciences Jaume Almera

Spanish National Research Council (CSIC)

Dr. Martin Schimmel

Institute of Earth Sciences Jaume Almera

Spanish National Research Council (CSIC)

Tutor

Dr. Alejandro Marcuello

Departament Earth and Ocean Dynamics

Universitat de Barcelona

CSIC CONSEJO SUPERIOR DE INVESTIGACIONES CIENTÍFICAS

ICTJA INSTITUT DE CIÈNCIES DE LA TERRA JAUME ALMERA

UNIVERSITAT DE BARCELONA

To those who never give up.

Acknowledgements

”He conseguido la beca!” - grité hace poco más de cuatro años a mi familia y amigos. En ese momento, llena de ilusión, incertidumbre y energía, empezaba una nueva etapa que ahora con estas líneas intentaré contextualizar, resumir y cerrar.

Soy de Madrid, estudié en el colegio Jesús-María y desde pequeña adoraba la Física. Solía suspender las asignaturas de ciencias, así que me daba vergüenza decir que algún sería una gran científica. En muchos momentos dudé de mí, sobre todo cuando se acercaba el final del instituto. Pero Roberto, mi profesor de física y matemáticas durante algunos años, daba unas clases llenas de pasión y cariño que me hicieron querer saber más y más. Con él dejé de intentar memorizar asignaturas, aprendí a razonar y conseguí seguir con mi idea. Quería darte las gracias porque, quizá sin saberlo, has sido un referente para mí.

Acabé el instituto y empecé a estudiar Física en la Universidad Complutense. Fueron cinco años muy intensos, es una carrera muy exigente y además tenía que trabajar como profesora particular en mi reducido tiempo libre. Contratiempos y adversidades tampoco faltaron, pero conseguimos aprobar año tras año. Y digo conseguimos porque sin ti, Rafa, es muy probable que no lo hubiera hecho. Tu apoyo incondicional, tu afán por ayudarme y tu paciencia lo han hecho posible. Mil gracias.

Acabé la Universidad y de esa etapa me llevé, a parte de los títulos, grandes personas que no dudaron en aminarme y abrazarme cuando lo necesitaba. Seguro que si alguna de ellas lee estás líneas sabría que las he escrito pensando en ella. Por si acaso menciono algunos nombres: Borlaff, Carlos, Cristian, Jorge, Dani y por supuesto mi todavía compañero de fatigas Ángel. No me puedo olvidar de mi Ro, Guille y Ainhoa, aunque os tengo en mi vida desde hace muchos más años, quería daros las gracias sobre todo por aguantarme y mantener nuestra amistad, que me ha ayudado mucho, aunque a veces la haya descuidado.

Empecé la tesis en el Jaume Almera una vez me dieron esa beca. Lo primero quiero agradecer a mis directores, Jordi Díaz y Martin Schimmel, el haberme metido en este bonito mundo de la sismología, haberme dado la libertad de elegir el camino de mi tesis y por haber personalizado vuestra labor como directores a mis necesidades, ya sea con horas de enseñanza o dejándome pasar semanas desaparecida inmersa en nuevas ideas que no siempre llegaban a buen puerto. Además, son de agradacer los consejos para no perder la bondad dentro de este mundo tan competitivo en el que estoy entrando. También quería dar las gracias a mi tutor, Alex Marcuello, que estos últimos meses me ha ayudado mucho con la elaboración de este manuscrito.

Tengo que decir que no hubiera sobrevivido a la tesis sin esos divertidos momentos que me han regalado todos compañeros del instituto, todos los de *Almejas*. Muchas gracias chicos, aunque haya estado meses fuera o encerrada en el despacho, hacéis todo muy fácil y siempre me recibís con una bonita sonrisa. En especial quiero agradecer a Evelyn, Mari, Encarni, Laura, Lluch, Paula, Raquel, Clara... todas mis chicas a las que adoro y que juntas nos hemos ayudado, apoyado y sobre todo **reído**.

Como decía he estado meses fuera, en concreto en el ETH Zürich durante dos estancias de cuatro y seis meses. De esta etapa, me gustaría dar las gracias a Anne Obermann por la oportunidad de trabajar en SED, en especial por el primer año, cuando sin a penas saber inglés y sin conocerme me aceptó con los brazos abiertos. También por integrarme en el mundillo y ayudarme a difundir mi trabajo, pero mayormente, por confiar en mí :) No me puedo olvidar de las geniales personas que he conocido en Zúrich: Naira, Alejandro, Amaneh, Ali, Thamy, Mehrdad, Matteo and many more friends that made the ETH a beautiful place for working.

De la última etapa del doctorado me llevo a una persona que se ha volcado en ayudarme y sacarme una sonrisa desde el primer día que nos conocimos, mi proofreader, mi malagueño favorito, mi compañero, Antonio. Gracias por hacerlo posible.

A quienes no puedo encajar en ninguna etapa porque han estado siempre en mi vida es a mi familia. En concreto a mis padres que, aún sin ser nada fácil, nunca han consentido que pierda mi norte. A mi querido hermano, te adoro. Queriendo ser un buen ejemplo para ti me he convertido en lo que soy y me doy cuenta, que el ejemplo lo has sido muchas veces tú para mí. Juntos me habéis enseñado lo más valioso que tengo, y sois vosotros. Mil gracias por tanto.

Y la beca de investigación que ha hecho posible que sea científica me fue otorgada por el Ministerio de Economía y Competitividad dentro del proyecto nacional MISTERIOS (CGL2013-48601-C2-1-R) y bajo el nombre de *ayudas para contratos predoctorales para la formación de doctores* (BES-2014-069419) que pertenece al *Programa Estatal de Promoción del Talento y su Empleabilidad en I+D+i*.

Abstract

Monitoring the elastic properties of the subsurface is of a special interest to mitigate the associated risk with natural and artificial hazards. In the last decade, coda-wave interferometry has become an excellent tool to characterize the subsurface in a large variety of environments. Additionally, coda-wave interferometry applied to the ever-present seismic ambient noise enables a continuous retrieval of virtual-source responses that allows monitoring structural and mechanical changes of media.

Throughout this thesis, we perform a comprehensive study of seismic noise interferometry employing all the currently used methodologies to observe lag-time changes: Time evolution of waveform similarity, waveform stretching and moving window cross-spectrum technique. Furthermore, we introduce some improvements in order to increase the temporal accuracy and sensitivity of said methodologies to detect tiny medium changes.

In particular, we carry out the study in two scenarios with very different tectonic settings: the 2011 El Hierro eruption and the Reykjanes geothermal system (RGS). We compute the phase auto- and cross-correlation (PCC) of 1.5 years of continuous seismic noise records of all available seismic stations in both cases. The PCC provides an accurate and amplitude-unbiased measure of coherence between two seismic traces and allows obtaining detailed daily seismic response of media.

In the case of the 2011 El Hierro volcanic eruption, through the analysis of waveform similarity time series of auto-correlations we clearly identify different pre-eruptive phases, as well as the end of the main magmatic emission and three magmatic intrusions that occurred in 2012. We use probabilistic sensitivity kernels to locate the places of the highest dynamics, providing that the most affected areas correspond to the magmatic accumulation zone

and the extinct volcanic area of Tiñor. In this study, we also introduce the change point analysis approach in order to automatically detect significant changes in time series.

The second scenario consists in studying stress changes and potential deformations of the subsurface caused by geothermal well operations at RGS. For that purpose, we retrieve and analyse time series of waveform similarity values and seismic velocity variations. However, the continuous production over a large area and various injection wells make challenging the detection of time-lag changes in the coda. To tackle this issue, we decompose the similarity time series into the time-frequency domain through the S-transform, which allows us to discriminate fluctuations associated to injection and production rate drops. Furthermore, we observe a slow seismic velocity decrease in the reservoir due to the water deficit as well as seasonal variations associated with the energy production demand.

Contents

List of Figures

List of Tables

Glossary

CCG Classical cross-correlation geometrically normalized

CCN Classical cross-correlation geometrically normalized applying one-bit amplitude normalization and spectral whitening

CPA Change point analysis

CWI Coda-wave interferometry

EGS Enhanced geothermal system

IGN Instituto Geográfico Nacional

IHM Instituto Hidrológico de la Marina

INVOLCAN Instituto vulcanológico de Canarias

MAR Mid-Atlantic Ridge

MWCS Moving window cross-spectral analysis

PCC Phase cross-correlation

PEVOLCA Regional government emergency committee

PSD Power spectral density

RGS Reykjanes geothermal system

SI Seismic interferometry

1 Introduction

1.1 General context

Geophysical methods are typically based on the resolution of inverse problems since most of the observables are limited to just a few kilometres of the crust. Inverse problems allow us to infer the causal factors that explain the observational data through forward operators, which describe the physical system under study. A classical exemplary inverse problem was the inference of the solid inner core of the Earth from the observation of P' waves in seismograms through the ray theory (Lehmann, 1936). Nowadays, Earth's subsurface imaging is the focus of many research branches such as magnetotellurics, electrical resistivity imaging and seismic tomography.

Seismic imaging constitutes a powerful approach to estimate the properties of the Earth's interior at different scales. Traditionally, earthquakes have been the main source of seismic waves used for sampling the subsurface. The relationship between the travel time and distance describes the propagation of the ballistic waves and is the key to classical seismic imaging techniques. On the other hand, in high heterogeneous media the seismic waves suffer numerous scattering processes along their travel path and the initial direction of propagation vanishes over time. Thus, the wave propagation become very complex and such relationship unachievable.

In seismograms, those multiply scattered waves form the so called *coda* and arrive after the ballistic waves. Coda waves spend more time in the propagation medium and are therefore more affected by medium changes. This high sensitivity can be used for monitoring the scattering properties of media. However, the inhomogeneous spatial distribution of earthquakes, together with their intermittent occurrence, encourage the increasing attention to *ambient seismic noise*. This noise is the continuous vibration of the ground caused mainly by oceanic and atmospheric interactions and recorded continuously everywhere on the planet.

The way to obtain information about the subsurface using seismic noise is through correlating the seismic wavefields recorded by two receivers (e.g. Weaver & Lobkis, 2001a; 2001b; Derode et al., 2003; Campillo & Paul, 2003). The correlation can be understood as another wavefield that travels from one receiver to another and is directly related to the seismic response of the medium (Green's function). Hence, ballistic and coda waves constitute the correlation wavefield as well.

The high sensitivity of coda waves to medium alterations along with the continuous Green's functions that offer the seismic noise, lead to the *coda-wave interferometry* (CWI, Snieder et al., 2002). This approach has been applied successfully on various scales (e.g., Stähler et al., 2011; Obermann et al., 2014) and in a variety of environments (Sens-Schönfelder & Wegler, 2011) for monitoring purposes.

In particular, the study of waveform changes in the coda of seismic noise correlations emerged in the last decade as a complementary tool to gain information about ongoing deformations in the subsurface due to the movement of pressurized volcanic fluids that alter the elastic and scattering properties of the medium (e.g., Brenguier et al., 2008; De Plaen et al., 2016; Obermann et al., 2013b).

1.2 Interest and motivation

Despite the increasing popularity of CWI in the last decades, some aspects require to be investigated in detail. For instance, the effects of the seismic network distribution or the choice of the reference period on quantifying medium changes, whether this approach can be automated or which geological information may be needed *a priori*. Moreover, the common goal of all the above mentioned studies is to monitor medium changes in order to mitigate or prevent natural or artificial hazards. Therefore, the temporal accuracy is crucial in this type of studies.

The main goal of this thesis has been performing a comprehensive study of seismic noise interferometry in the framework of monitoring the elastic properties of the crust. I have learned, coded and applied the all the current methodologies that quantify temporal changes in the subsurface to two different scenarios that I briefly introduce below. With them, we seed light to some previous questions with special emphasis on increasing the temporal accuracy and sensitivity of those methodologies to detect medium changes.

The first case of study is the 2011 El Hierro eruption that leads to a new small volcano in the Canary Archipelago, called Tagoro. The volcanic eruption was submarine and took place in the southern tip of El Hierro island. It was preceded by surface deformations and intense seismic unrest, which initially was located in the central part of the island and migrated southward till the final eruption site. Several geophysical instruments were distributed around the island to monitor this anomalous seismicity, turning this eruption into the first in the Canary Archipelago tracked in real time since its onset. The eruption has been studied in great detail through various geophysical approaches except CWI.

Therefore, the first particular objective of this thesis is to assess the potential of CWI to infer scattering changes in the subsurface due to the 2011 El Hierro eruption. This scenario shows some particularities with respect to other volcanoes monitored with this approach (e.g. Brenguier et al., 2008; Obermann et al., 2013b; Sens-Schönfelder & Wegler, 2006), for instance, the seismic network could not be distributed around the volcano since was submarine, its dimensions are small and furthermore the dataset prior to the eruption sparse.

We evaluate the time evolution of the scattering changes throughout 2011 and 2012 beneath El Hierro island. The obtained results are in good agreement with previous studies and besides, we provide new information about the volcanic eruption. In addition, we also introduce some improvements in the common signal processing procedure in order to improve the accuracy in monitoring temporal changes.

In view of the successful results of this research, we tackle the following study that form the second part of the thesis. In this case, the target is a hydrothermal system located on the southwestern tip of the Reykjanes peninsula in Iceland. Recently, the use of seismic interferometry in a geothermal context has received considerable attention. Thanks to the enhancement of geothermal conditions such as rock permeability, the number of exploitable geothermal reservoirs has increased exponentially in last decades.

The Reykjanes geothermal system (RGS) was deployed in the fifties and currently is still working. In 2006 a new power plant was developed increasing significantly the system's power capacity. Consequently, a man-made subsidence of around 10 cm was measured in the area among other repercussions. In 2009 the re-injection of water into the rock mass began in order to counteract the effects.

It is the first time that a hydrothermal system is studied using seismic interferometry. Thus, the main goal of this study is to prove the capability of this method for monitoring hydrothermal systems. We obtain the time evolution of the mechanical and structural properties of the medium and find some other byproducts caused by the heat mining of the reservoir.

These two research lines lead us to the following scientific articles, which in turn constitute the present thesis. Due to the short format of the peer-reviewed journal, I have elaborated on the methodology and the obtained results in this manuscript in order to give a better understanding.

Sánchez-Pastor, P., Obermann, A. & Schimmel, M. (2018). Detecting and locating precursory signals during the 2011 El Hierro, Canary Islands, submarine eruption. *Geophysical Research Letters*, 45(9), 10288-10297. https://doi.org/ 10.1029/2018GL079550

Sánchez-Pastor, P., Obermann, A., Schimmel, M., Weemstra, K., Verdel, A., & Jousset, P. (2019). Short- and long-term variations in the Reykjanes geothermal reservoir from seismic noise interferometry. *Geophysical Research Letters*. Accepted.

Throughout the four years of my PhD thesis, I have collaborated in other research lines based on studying and monitoring different seismic sources as river discharges associated with snowmelt episodes in the Pyrenees as well as peculiar signal sources recorded within a city such as road traffic, football games and music concerts. These studies have enriched my understanding in signal processing and seismic wave propagation; allowing me to realize the large variety of seismic waves that we can find and study within a seismogram. Additionally, this research line has yielded the following two scientific publications, in which my main contributions have been the participation in the interpretation of results, elaborating some figures and revising the manuscripts:

Díaz, J., Ruiz, M., Sánchez-Pastor, P. & Romero, P. (2017). Urban seismology: on the origin of Earth vibrations within a city. *Scientific Reports*, 7(1), 15296. doi:10.1038/s41598-017-15499-y

Díaz, J., Ruiz, M. & Sánchez-Pastor, P. (2019). Hierarchical classification of snowmelt episodes in the Pyrenees using seismic data. *Scientific Reports*. Under review.

1.3 Thesis outline

This thesis is presented as a scientific article compendium under the regulation of the Faculty of Earth Sciences and the *Departament de Geodinàmica i Geofísica* to which I belong.

Firstly, I briefly contextualize the seismic noise and seismic interferometry, which constitute the base of this work. I then continue explaining the two scenarios of study, in particular, their geological framework, previous studies in the matter and particularities of both of them. In addition, the data used to tackle the investigations is described at the end of each point.

In Chapter 3, I explain the relationship between the Green's function and seismic noise correlations. The techniques employed here for detecting and quantifying temporal changes in the subsurface are reviewed as well. Then, I will explain the use of sensitivity kernels for locating those changes in 2D.

The obtained results and their interpretation are presented together for each study case in order to ease the reading in Chapter 4. The discussion of the thesis (Chapter 5) is then focused on the methodology, which is the common aspect in both studies. Moreover, I include some avenues to improve the obtained results in future studies.

Finally, I will remark and summarize the most important findings and contributions of the two addressed research lines of this manuscript in Chapter 6.

I hope you enjoy this thesis and if you have any suggestion, question or advice I would love to know (psanchezsp@gmail.com) :)

2

Framework and scenarios of study

2.1 Seismic noise interferometry

Instrumental seismology dates back to the eighteenth century although we find in the literature numerous attempts to build effective seismometers that recorded the ground motion and time of earthquakes. Among them stand out John Milne, James Ewing and Thomas Gray, who develop the first successful seismographs in Tokyo at the end of the nineteenth century. An important advance in this matter was performed by Wiechert (1899), who introduced a proper damped seismometer to lessen the effects of the pendulum eigen-oscillations. A change in the paradigm was brought by the Rusian physicist B. B. Galitzin (Golicyn) in 1903 when, instead of using mechanical devices, he applied electrodynamic sensors and photographically-recording galvanometers to build a seismometer of high sensitivity. The first to express mathematically a seismometer behavior in presence of an earthquake was Forbes (1844).

Besides the recording of earthquakes, the first seismometers measured a continuous ground shaking with frequencies between 0.04 and 1 Hz, which composes the microseismic band. This ground motion was related to regional weather conditions (Bertelli, 1872) and later on, to ocean swell on coasts as well (Wiechert, 1904). Omori (1913) pointed out that this recorded 'noise' provides information about the medium of propagation. Although to study in detail its origin and sources, it was needed a decomposition of the seismic signal in the frequency domain that was nearly impossible by hand. Years later, Aki (1957) analysed the cross-spectra of microseisms and inferred shear wave velocities in the shallow crust thanks to the arrival of computers. On average, the power spectral densities of seismic noise worldwide show similar behaviour and Peterson (1993) summarised them in the 'New Low and High Noise Models'.

The microseismic band contains two energy peaks in the frequency domain that correspond to different source mechanisms. The primary microseism in observed between 0.05 and 1 Hz, which is the dominant frequency in ocean gravity waves. Generally, its origin is related to the interaction of ocean waves with sloping sea floor (e.g. Ardhuin et al., 2015; Hasselmann, 1963; Saito, 2010). The secondary or double-frequency microseism is more energetic than the primary and appears between 0.1 and 0.3 Hz. It is caused by the interaction of ocean wave trains with similar frequencies and opposite directions (e.g. Longuet-Higgins, 1950; Tanimoto et al., 2006; Stutzmann et al., 2011). Body waves are also present in this microseism (e.g., Backus et al., 1964; Iyer & Healy, 1972) and are often associated with local storms (e.g., Gerstoft et al., 2006; 2008).

As both microseisms are generated by atmospheric and oceanic processes, the ambient seismic noise shows clear seasonal variations (Figure 2.1) (Stehly et al., 2006; Landès et al., 2010). At lower frequencies, the Earth's hum is recorded from 2 to 15 mHz and consist of Earth's free oscillations (e.g. Nishida et al., 2010; Suda et al., 1998). The normal mode peaks are similar to the 'tones' of musical instruments and are observed isolated approximately between 2 and 7 mHz (Tanimoto et al., 2005). At high frequencies (above 1 Hz), anthropogenic activity predominates specially in urban places (Díaz et al., 2017). Besides these main features that are observed in spectra, the variety of seismic signals recorded extents over a broad frequency range whose sources can be very diverse. An idea of the rich signal content in spectra can be found in Díaz et al. (2016).

Seismology is classically referred to the study of the propagation of seismic waves through the Earth that are typically caused by earthquakes. Those waves has been widely used to study the Earth's interior although an important limitation is the inhomogeneous and limited distribution in space and time of earthquakes. Thus, the ambient seismic noise has been gaining popularity since the extraction of Green's functions is possible from correlating diffusive wavefields, being this the base of seismic interferometry (SI). This approach has been exploited in different study areas to infer characteristics of diverse processes such as in the subsurface of the Sun (Duvall et al., 1993), microbaroms (Haney, 2009, Fricke et al., 2014), shallow water environments (Roux & Fink, 2003) and buildings (Snieder and Safak, 2006; Kohler et al., 2007).

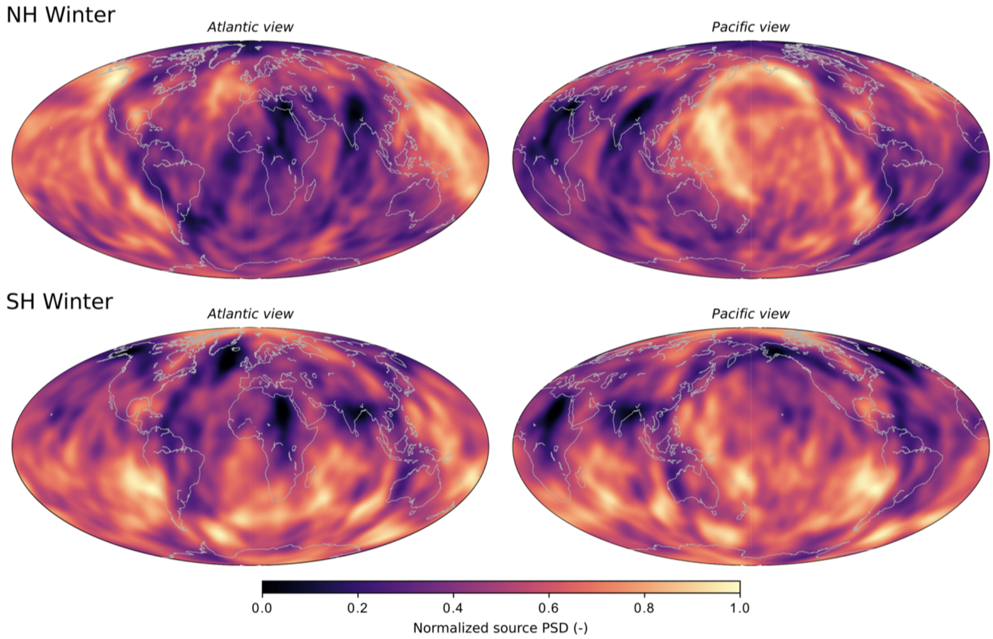

Figure 2.1: Global PSD models - The top two maps show two views of the normalized source PSD model for North Hemisphere winter, the two bottom ones for austral winter (modified from Ermert, 2017)

To understand better the relationship between correlations and Green's functions of media, let me consider a wavefield ($u(\mathbf{x}, \omega)$) governed by the acoustic wave equation

$$\mathcal{L}u(\mathbf{x}, \omega) = -\omega^2 u(\mathbf{x}, \omega) - c^2 \Delta u(\mathbf{x}, \omega) = N(\mathbf{x}, \omega) \tag{2.1}$$

where $\mathcal{L}$ is the wave equation operator, c the acoustic wave speed, ω the angular frequency and $N(\mathbf{x}, \omega)$ the noise source distribution. Linear ordinary differential equations can be easily solved by the Green's function, which represents in this scenario the impulse response of the medium to seismic wave propagation. Thus, the seismic displacement field created at $\boldsymbol{\xi}$ and recorded at $\mathbf{x}$ is given by

$$u(\mathbf{x}, \omega) = \int G(\mathbf{x}, \boldsymbol{\xi}, \omega) N(\boldsymbol{\xi}, \omega) d\boldsymbol{\xi} \tag{2.2}$$

being $G(\mathbf{x}, \boldsymbol{\xi}, \omega)$ the Green's function with source at position $\boldsymbol{\xi}$. The correlation in frequency domain of two recordings at positions $\mathbf{x_1}$ and $\mathbf{x_2}$ is then:

$$\mathcal{C}(\mathbf{x_1}, \mathbf{x_2}) = u(\mathbf{x_1}, \omega) u^*(\mathbf{x_2}, \omega) = \iint G(\mathbf{x_1}, \boldsymbol{\xi}_1, \omega) G^*(\mathbf{x_2}, \boldsymbol{\xi}_2, \omega) N(\boldsymbol{\xi}_1, \omega) N^*(\boldsymbol{\xi}_2, \omega) d\boldsymbol{\xi}_1 d\boldsymbol{\xi}_2 \tag{2.3}$$

where * denotes complex conjugation. As Green's functions describes the seismic response of the medium can be considered time invariant. On the contrary, seismic sources vary over time, however if they are spatially uncorrelated, the average over time tends to zero. Therefore, the expected value of the noise sources is

$$< N_1(\boldsymbol{\xi}_1) \cdot N^*{}_1(\boldsymbol{\xi}_2) >= S(\boldsymbol{\xi}_1) \cdot \delta(\boldsymbol{\xi}_1 - \boldsymbol{\xi}_2) \tag{2.4}$$

with S being the power spectral density (PSD) and δ the Dirac delta function. Assuming sources spatially uncorrelated, the expected correlation takes the next form:

$$C(\mathbf{x_1}, \mathbf{x_2}) =< \mathcal{C}(\mathbf{x_1}, \mathbf{x_2}) >= \int G(\mathbf{x_1}, \boldsymbol{\xi}, \omega) G^*(\mathbf{x_2}, \boldsymbol{\xi}, \omega) S(\boldsymbol{\xi}) d\boldsymbol{\xi} \tag{2.5}$$

Thus, comparing the equations 2.2 and 2.5, $C(\mathbf{x_1}, \mathbf{x_2})$ can be interpreted as a correlation wavefield with $G^*(\mathbf{x_2}, \boldsymbol{\xi}, \omega)S(\boldsymbol{\xi})$ as deterministic source. This assumption is commonly used in seismic interferometry studies (e.g. Fichtner 2014; Snieder, 2004; Tromp et al., 2010) and in practice achieved stacking over time $\mathcal{C}(\mathbf{x_1}, \mathbf{x_2})$ (Bensen et al., 2007; Seats et al., 2012). Incoherent signals product of other sources or instrumental noise are also averaged out in the stacking process and the convergence to an approximated Green's function improves.

The Earth's lithosphere is heterogeneous at different scales, from the distinct atoms that compose a material to topographic variations. The medium's heterogeneities act as scatterers for the seismic waves yielding the later-arriving multiply scattered waves; so-called coda waves. They are observed after the arrival of the ballistic P- and S-waves in seismograms. Note that all these seismic waves are present as well in correlograms since the correlation can be understood as a seismic wavefield.

Aki (1969), followed by other authors (e.g. Sato, 1977; Herraiz and Espinoza, 1997), were the pioneers in studying coda waves to obtain information about the regional scattering and attenuation properties. These waves sample the subsurface very densely and hence are more sensitive to weak changes than direct waves. A change in the mechanical properties (e.g. seismic velocity, pore pressure) yields a dilatation or contraction of the waveform (Figure 2.2a), and structural variations (e.g. altered seismic discontinuities, fracturing) are translated into the correlograms in waveform distortion (Figure 2.2b).

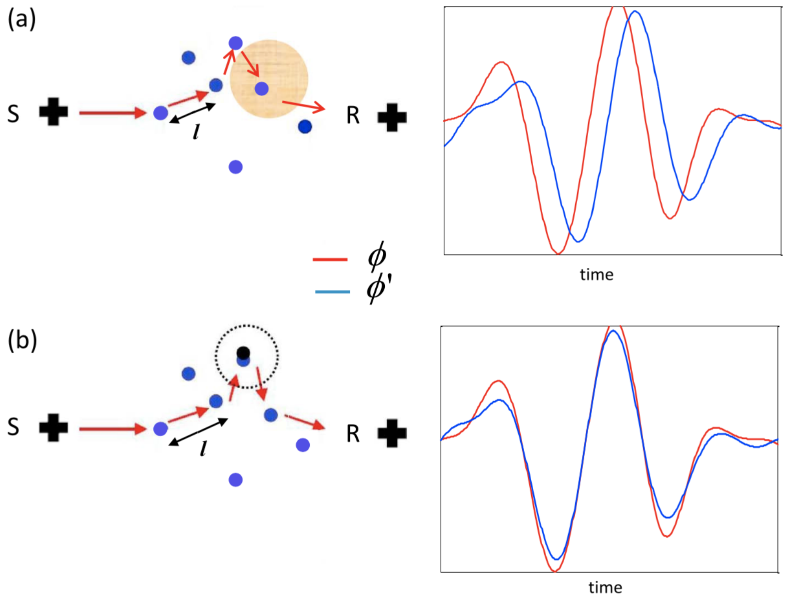

Figure 2.2: Schematic representation of a structural and mechanical change - (a) Velocity change and (b) structural change on the left and their effect on a seismic signal on the right. The blue dots represent the scatterers, S and R are the source and receiver respectively and l the scattering mean free path (see text for further details). The blue and red curves represent the perturbed and original signals respectively. (Figure modified from Obermann, et al., 2014).

The degree of heterogeneity can be quantified through the scattering mean free path (l), which represents the travelled distance by seismic waves between two consecutive scattering processes (Figure 2.2). The multiply scattering regime can be assumed when either the medium has many scatterers or the distance between the source and receiver (D) is large, i.e., when $D >> l$. So the seismic waves are diverted several times and its initial direction of propagation is lost before being recorded. The travel time – distance relationship of such waves is here unachievable. Furthermore in elastic media, this multiply scattering regime is characterised by energy equipartitioning of coda waves. Seismic waves are converted from P- to S- waves and viceversa at each scatterer and tend to be equally present; reaching a stationary regime after some scattering processes (Hennino et al., 2001).

Under these conditions, coda waves probe the propagation medium very densely and become quite sensitive to variations in the scattering properties of media. This idea, together with the retrieval of seismic responses from wavefields correlations, turns the coda-wave interferometry (CWI, Snieder et al., 2002) into an excellent technique to monitor changes in the subsurface. In Chapter 3, I will explain in detail the Green's function retrieval as well as the currently used approaches to detect and locate mechanical and structural changes.

Below, I introduce the two study scenarios that will be addressed in the context of coda wave interferometry: The 2011 El Hierro eruption and the Reykjanes geothermal reservoir. I describe their geodynamical and geological framework as well as the seismic data used in both cases.

2.2 Scenario 1: The 2011 El Hierro eruption

The Canary Archipelago is comprised of seven major volcanic islands located 100 km off the Northwest African coast. They are the result of a long-term volcanic and tectonic activity on the passive margin of the African Plate whose origin is still controversial. Several contrasting models have been proposed to explain it, from a presence of a hot spot (e.g. Carracedo et al., 1998) to model of uplifted tectonic blocks (Araña & Ortiz, 1986). The most recent theory is based on the idea of a shallow mantle upwelling that produces recurrent melting anomalies since the Late Jurassic; making the Canary Island Seamount Province the most long-lived hot spot preserved on earth (van den Bogaard, 2013).

El Hierro is the south-western most, youngest and smallest island of the archipelago. The island is a perfect example of a triple-armed rift system (Carracedo, 1996; 1998). The three main edifices correspond to the Tiñor volcano, El Golfo-Las Playas Edifice and the island's Rift volcanism (Guillou et al., 1996; IGME, 2010). Several debris avalanches in the past 900 ka have built the characteristic Y-shape morphology of El Hierro (Figure 2.3) (e.g. Masson, 1996; 2002; Longpré et al., 2011).

The Canary Archipelago has been volcanically active with several eruptions in the last five centuries (Carracedo, 1994). Since the arrival of the Spaniards in these islands there are historical records of volcanic eruptions. All of them were basaltic and monogenetic and their duration ranged between weeks to a few months, excepting the 1730 Timanfaya eruption in Lanzarote which lasted for six years (Romero, 2000). Over the

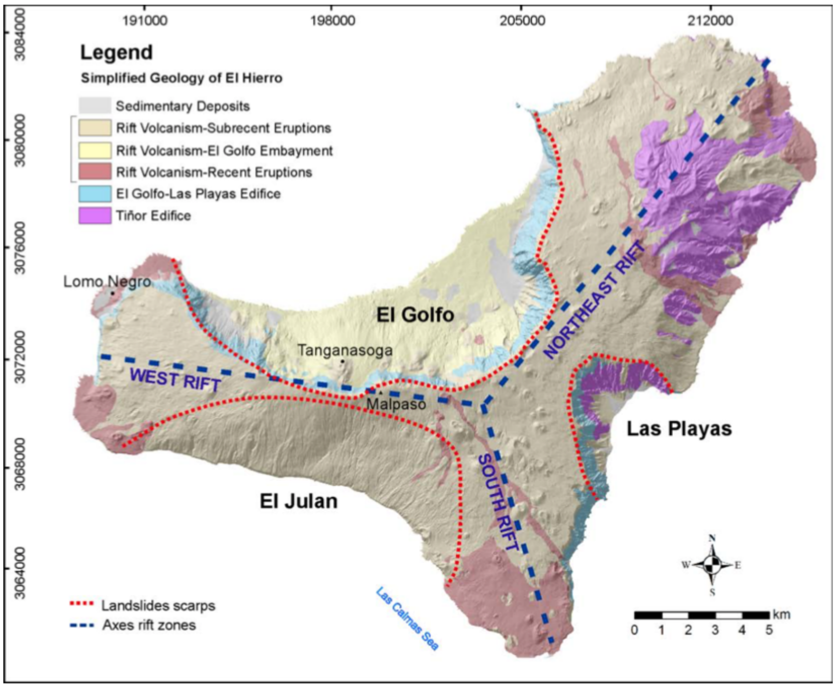

Figure 2.3: Simplified geological map of El Hierro Island - (modified from IGME, 2008)

past few thousand years, the most important eruptions in El Hierro are related to the extinct volcanic area of Tiñor in the east/northeast part of the island and the Tanganasoga volcano, which is located inside the El Golfo depression (Figure 2.3). After the 1971 eruption of Teneguia in La Palma (Martí et al., 2013), the archipelago remained in quiescence for four decades.

In July 2011, a sudden onset of microseismic activity was recorded in El Golfo depression, which was caused by a magmatic intrusion at around 5 km from the town La Restinga (e.g. Martí, Castro et al., 2013; Carracedo et al., 2012). The seismicity reached a maximum rate of 450 events per day in one month. Most of the events were located between 10 and 15 km of depth. In September, the seismicity migrated southward crossing the island (Figure 2.4) and the GPS data showed a significant increase of surface deformation (López et al., 2012). At the end of this month, there was a drastic increase of seismic events that were located between 15 and 25 km depth. On the 1st of October, a sudden deflation and re-inflation process was inferred from the GPS measurements. The seismic unrest culminated after a few days of system stabilization in the volcanic eruption of El Hierro submarine volcano on 10 October 2011; currently known as Tagoro. The previous pre-eruptive phases follow the study of López et al. (2012) and are summarized in Table 2.1.

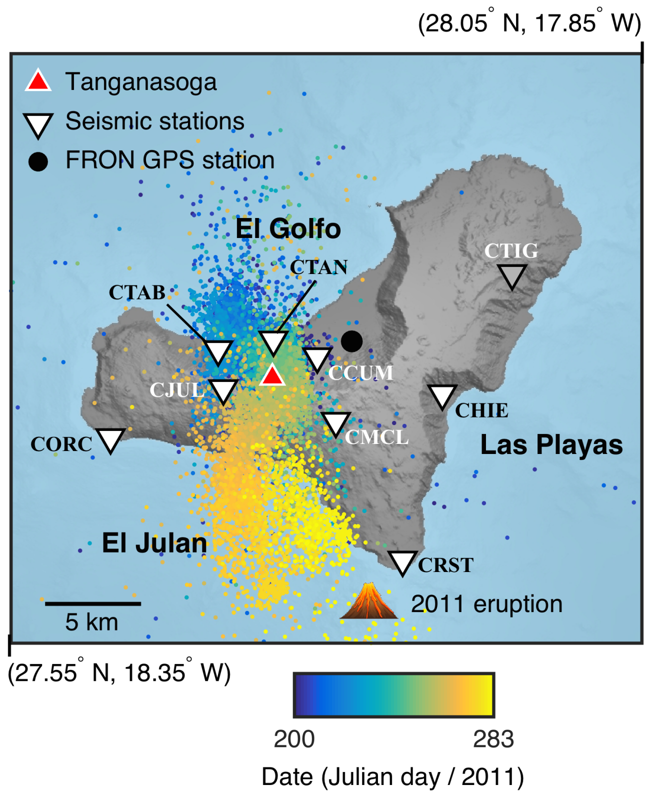

Figure 2.4: Location of the seismic stations in El Hierro and representation of the pre-eruptive seismic unrest - Inverted triangles mark the location of the seismic stations. The station in gray has been discarded due to problems with its frequency content. The black dot marks the GPS station FRON. The time evolution of the seismicity prior to the eruption in 2011 is marked with colored dots.

The eruption took place in a north-south trending fissure in the southern flank of the island at around 5 km from the town La Restinga (Martí, Pinel, et al., 2013). The first surface manifestations appeared a few days later than the strong seismic tremor and were in terms of strong bubbling due to the degassing of rocks, which was recorded by all seismic stations working at that moment (López et al., 2012). The frequency range of the tremor was very wide, reaching frequencies above 10 Hz, although its dominant frequency oscillated between 0.5 and 1.9 Hz (Tárraga et al., 2014). The Tagoro volcano grew from 375 to 89 m depth in two main phases, separated by a period of collapse in

Pre-eruptive phase	Main feature	Dates
I	Slight deformation	07 Jul - 18 Jul 2011
II	Beggining of the unrest	19 Jul - 03 Sep 2011
III	Seismic migration southward	04 Sep - 26 Sep 2011
IV	Acceleration of the process	27 Sep - 07 Oct 2011
V	Forthcoming eruption	08 Oct - 10 Oct 2011

Table 2.1: Pre-eruptive phases of 2011 El Hierro eruption - (Based on López et al. (2012).

early December, 2011 (Somoza et al., 2017). The end of the eruption was announced on 5 March 2012 by the regional government emergency committee (PEVOLCA) although the erratic decrease of the seismic tremor and activity complicated the decision of such date (Figure 2.5).

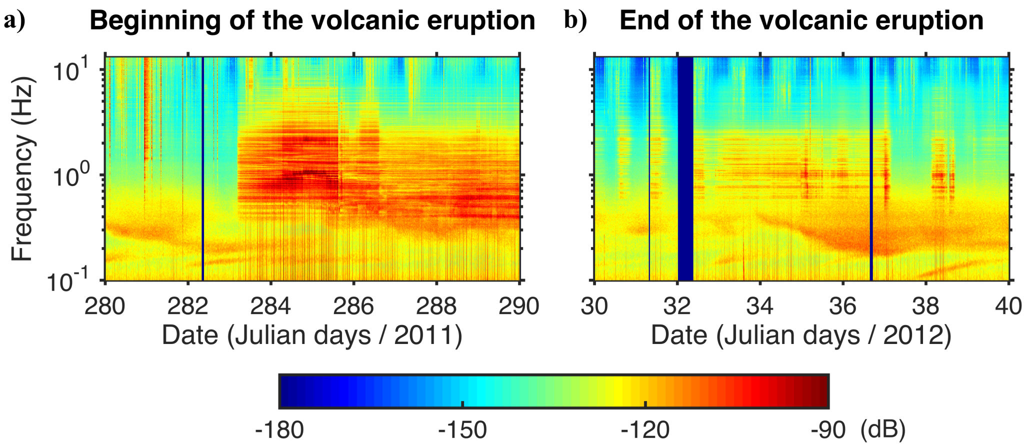

Figure 2.5: Spectrogram of the beginning and end of the 2011 El Hierro eruption - Ground motion spectrogram for the vertical component of the CCUM station during 10 days around (a) the beginning of the eruption and (b) its end.

In the post-eruptive period, deep magma upwelling trapped in the Moho discontinuity at 14-16 km depth caused several episodes of large deformations and seismic swarms (Lamolda et al., 2017). In particular, based on seismic records and surface deformation estimations, six post-eruption magmatic intrusions have been inferred at different parts of the island since June 2012 till March 2014, which, however, did not culminate in eruptions (e.g. Díaz-Moreno et al., 2015; García et al., 2014; González et al., 2013; Telesca et al., 2016). These intrusions were more energetic and cause larger surface deformations than the pre-intrusion of July 2011 that yields the formation of

Tagoro (Table 2.2). The total cumulative uplift due to the post-eruptive activity was around 20 cm (e.g. Klügel et al., 2015; Lamolda et al., 2017).

Tomography and microseismic sounding studies reveal high velocity zones beneath the Tanganasoga volcano and the extinct volcanic area of Tiñor, which are connected trough feeding channels down to 10 km. (García–Yegüas et al., 2014; Gorbatikov et al., 2013; Martí, Pinel et al., 2013). The magma accumulation zone of Tagoro is located below the central part of El Hierro island. The intrusive bodies and rheological discontinuities acted as stress barriers guiding the magma from El Golfo region to the Southern tip of the island (Martí et al., 2017).

The 2011 El Hierro eruption is the first on the Canary Islands that has been monitored in near real-time by the Instituto Geográfico Nacional (IGN) and the Instituto Vulcanológico de Canarias (INVOLCAN). Besides the seismic stations, instruments such as a gravimeter and several GPS, geochemical and magnetic stations, were installed on the island to monitor the evolution of the seismic unrest and following eruption (López et al., 2012). In order to elucidate its structure and improve the volcanic risk assessment, this eruption has been analysed in depth since its onset. It therefore offers a good scenario to asses the capability of seismic interferometry to detect and locate structural and mechanical changes in volcanic environments. We focus on the three magmatic intrusions inferred throughout 2012 and the pre-eruptive period in 2011.

Unrest label	Dates	Nº earthquakes	Max deformation (cm)
Jul 2011	16 Jul - 15 Oct	10069	5.4
Jun 2012	22 Jun - 11 Jul	2329	11.3
Sep 2012	13 Sep - 18 Sep	584	4.5
Dec 2012	30 Dec - 03 Jan	127	3.3
Mar 2013	17 Mar - 01 Apr	2192	15.5
Dic 2013	21 Dec - 24 Dec	333	5.4
Mar 2014	13 Mar - 18 Mar	303	3.4

Table 2.2: Characteristics of the post-eruptive episodes of unrest - Based on Lamolda et al. (2017)

We use seven broadband stations and one short-period station deployed by the IGN in 2011 (white triangles, Figure 2.4). Two stations covered the beginning of the unrest in July 2011; a total of six stations were running by mid-August, and additional two were set up in October, including the station at the southern tip of El Hierro

Island. We compare our results with surface deformation measurements from a GPS station (FRON), belonging to the Canarian Regional Government (black circle, Figure 2.4). There was an additional seismic station (CTIG, marked in gray in Figure 2.4), which was located in direct vicinity of a wind park and therefore affected by perturbed waveforms in some frequency bands. All of those seismic stations recorded with a sample rate of 100 samples/s; excepting CHIE with 50 samples/s.

One of the goals of this study is to analyse the pre-eruptive period with the aim of finding precursory signals. The seismic network was placed on land, which impeded a distribution around the volcano and besides, the network was completed shortly before the eruption. Consequently, the precursory signal quest represents a particular challenge due to the scarce and limited seismic data in this period. The obtained results together with their interpretation are detailed in Section 4.1.

2.3 Scenario 2: Reykjanes geothermal reservoir

The Iceland volcanic province is formed by the interaction of the Icelandic hotspot and the Mid-Atlantic Ridge (MAR). This interaction promotes the tectonics and causes the intense magmatisms characteristic of this region. The MAR crosses Iceland and currently is represented on land by the Western and Northern Volcanic Zones (WVZ and NVZ), which are bounded through the Mid-Iceland Volcanic Zone (MVZ). The two extreme sides of MAR on Iceland are the Reykjanes and Kolbensey Ridges. WVZ, NVZ and the Eastern Volcanic Zone (EVZ) forms the inverted Y shape of post-glacial lavas on Iceland (Figure 2.6a).

The Reykjanes peninsula is divided into two tectonic plates by the Reykjanes Ridge and part at an average velocity of 2cm/yr. The main features on this peninsula are the NE-SW normal faults and NE- trending eruptive fissures (Figure 2.6b). The active volcanic systems derive their energy from cooling magma bodies in the crust, such as magma chambers and dykes (Flóvenz et al., 2015; Gudmundsson, 1995; Gudmundsson & Thórhallsson, 1986). This volcanic activity and intrusive rocks provide an important heat source that reaches the surface and has been exploited since the settlement of Iceland in the 9$^{\text{th}}$ century.

Since 1928, the utilization of geothermal sources has been on commercial scale in Iceland for house heating (Flóvenz et al., 2015) playing nowadays a fundamental role

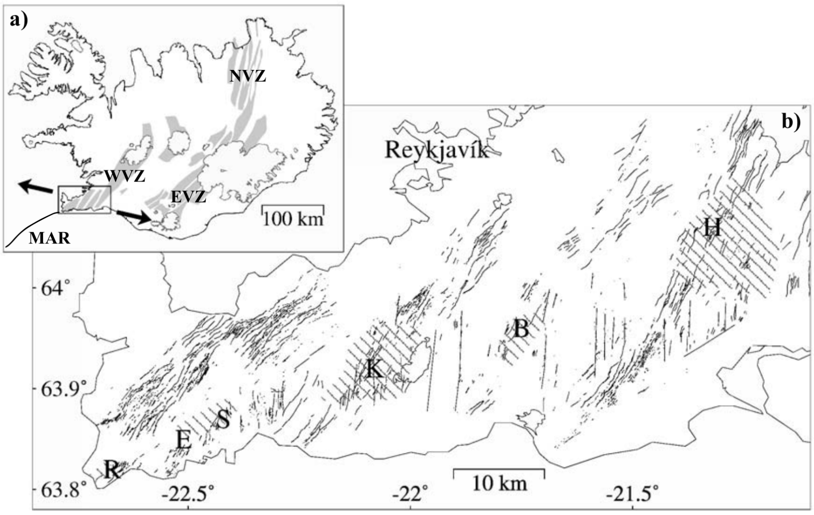

Figure 2.6: Tectonic map of Reykjanes peninsula - The hatched areas show the locations of high-temperature geothermal fields, labelled as R: Reykjanes, E: Eldvorp, S: Svartsengi, K: Krisuvik, B: Brennisteinsfjoll and H: Hengill. The Iceland inset shows the neovolcanic systems (grey shades) and the location of the Reykjanes peninsula. The arrows show the direction of the 2 cm/yr spreading across the peninsula between North America and Eurasia (DeMets et al., 1994). (Modified from Keiding et al., 2010).

in the energy economy of the country (Ragnarsson, 2013). In 2017, global geothermal power generation was estimated in 84.8 TWh, while the cumulative capacity reached over 14 GW. This power capacity is expected to rise over 17 GW in 2023 (International Energy Agency (IEA), 2018). The geothermal systems are distinguished attending to different aspects, such as the reservoir temperature or enthalpy, physical state, their origin and geological setting (Saemudsson et al., 2013). A general classification differentiates two types: hydrothermal and enhanced geothermal systems (EGS). The first term is employed when a system contains heat, fluid and high permeability naturally and are mainly limited to plate boundaries and volcanic environments. However, by far most geothermal energy accumulated within the crust is located in dry and low-permeability rocks. The permeability of rocks is improved in EGS through engineered fluid flow paths, which allows expanding the exploitable geothermal resources to numerous areas on Earth.

Geothermal resources are typically classified as renewable energy sources but in some cases the renewability is questionable. For instance, in Iceland, where geothermal energy utilization involves heat-mining (Sanyal, 2010). The energy flow and the vast storage of energy are the two main factors analyzed in order to define the renewability of a geothermal system. These factors vary with the type and conditions of each system and require an examination of their long-term behaviour (Axelsson et al., 2015).

The high heat flow generated at the Reykjanes Ridge together with the flat topography, highly permeable rocks and intense precipitations in the Reykjanes peninsula, favors the development of geothermal systems (Jousset et al., 2016). Currently, there are six geothermal systems of high-temperature around the peninsula (see Figure 2.6b). They are mainly placed at the intersections of the eruptive fissures and the strike-slip faults (Keiding et al., 2010). The Reykjanes Geothermal System (RGS) is one of them and is located on the southwestern tip of this peninsula (Figure 2.7). The high-temperature term is employed when the reservoir temperature is above 200°C at 1 km of depth (Saemudsson et al., 2013).

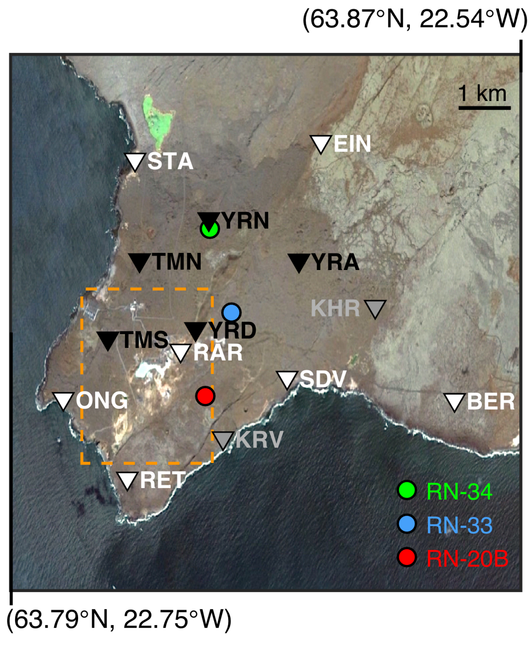

Figure 2.7: Satellite map of the RGS and seismic stations - The triangles stand for the selected seismic stations. The colors indicate the different type of sensors: Trillium 120 s (white), Mark sensors (grey) and Lennartz (black). The three injection wells running during the study period are shown by circles, RN-20B (red), RN-33 (blue) and RN-34 (green). The approximate location of production area of RGS is represented by the dashed orange square.

The RGS has been exploited since 1956 with a shallow drilling well (∼160m) and expanded in 2006 with 14 deep production wells (around 2 km of depth) and the development of a 100 MW capacity geothermal plant. A gravity change anomaly during the period 2008 - 2010 indicated that the reservoir fluid renewal was between 30 and 50 % (Axelsson et al., 2015). In 2009, the re-injection of sea water into the system began to counteract the pressure drop in the reservoir and reduce the environmental effects of surface disposal. Another important consequence of the increased production is a subsidence of around 10 cm in the area (Keiding et al., 2010).

We focus on the years 2014 and 2015 when the European Community's project IMAGE (Integrated Methods for Advanced Geothermal Exploration) was deployed. During this time, only one drilling well was running at 1.2 km of depth (RN-20B) and two were operating for tracer tests at around 2 km of depth. We use a subset of thirteen seismic stations from the Reykjanes Array (RARR; Weemstra et al., 2016) with different type of sensors: seven Trillium compact 120s, five Lennartz 5s and two Mark sensors (Figure 2.7). All of them were recording at 100 samples/s.

The production and injection rates of the three drilling wells during those years are depicted in Figure 2.8a. The number of recorded seismic events within and outside the production area are represented through histograms in Figure 2.8b. As can be seen, there is no apparent seismicity increase after the abrupt production rate variations of day 230 (2014). The recorded seismic events were located outside the production area.

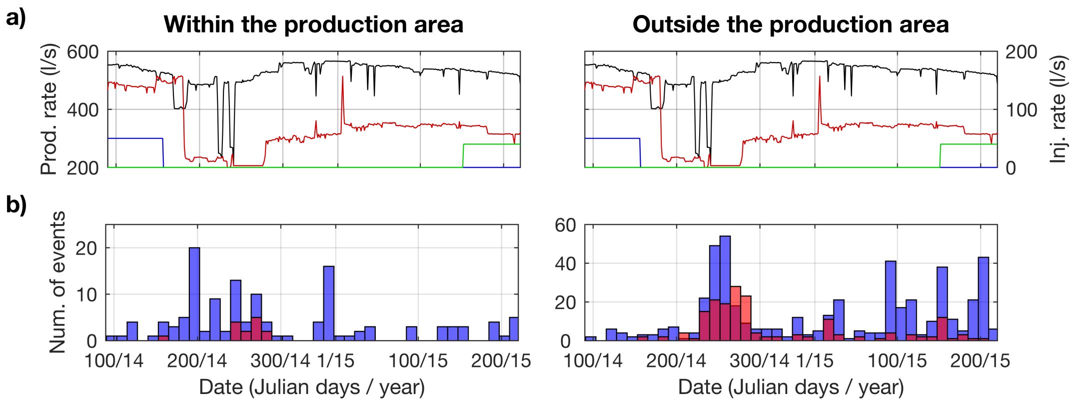

Figure 2.8: RGS activity and seismicity in the Reykjanes peninsula - (a) Production and injection rates of RGS are represented following the colours of Figure 2.7 during the period under study. (b) Histograms of the number of events recorded within (left) and outside (rigth) the production area. Blue bars represent seismic events of magnitude (mbLg) below 5 and reddish bars above 5.

Studying the rapid and slow response of the surrounding medium to production and injection rate variations is of special importance to monitor geothermal reservoirs. Typically, the rapid effects are monitored through the induced seismicity in the medium and the long-term consequences are investigated through variations in several observables such as resistivity, surface deformation, reservoir pressure and seismicity as well. Seismic interferometry has been used for monitoring enhanced geothermal systems (e.g. Hillers et al., 2015; Lehujeur et al., 2015; Obermann et al., 2015) and for the first time it is employed in a hydrothermal system. Thanks to this, we obtain a combined vision of the short- and long- term variations of the structural and mechanical properties in the sub-surface associated with the RGS. The results and their corresponding interpretation are explained in detail in Section 4.2.

3

Methods and data processing

In this Chapter, I explain the basic principles for Green's function retrieval from coda waves including the assumptions required for seismic monitoring. Then, I detail the current methods for detecting and locating temporal changes in the scattering properties of the Earth's crust. I further propose and explain some innovations with the aim of improving the monitoring of such temporal changes.

3.1 Green's function retrieval

From correlations between seismic wavefields, it is possible to obtain the Green's function between the source and each corresponding receiver (equation 2.5). Although the Green's function of interest is that which describes the medium response between both receivers and does not depend on the source positions. In the following, I show the analogy between the correlations and the desired Green's function through an intuitive way given by Derode et al., (2003).

To simplify the equations, let me consider only one source at $\boldsymbol{\xi}$ whose PSD is equal to one and two receivers located at $\mathbf{x_1}$ and $\mathbf{x_2}$ (Figure 3.1a). The correlation between their signals in the time domain is then:

$$\mathcal{C}(\mathbf{x_1}, \mathbf{x_2}) = G(\mathbf{x_1}, \boldsymbol{\xi}, t) * G(\mathbf{x_2}, \boldsymbol{\xi}, -t) \tag{3.1}$$

where $*$ denotes convolution.

In acoustics, focusing a wave on a target point through an inhomogeneous medium is an important problem that can be solved by mirror points (Fink, 1989; 1992). These points receive a signal, which is time-reversed and re-emitted back to the source point. Using this concept, consider now the source placed at $\mathbf{x_2}$ and in the point $\boldsymbol{\xi}$, a mirror point (Figure 3.1). The recorded displacement at the latter point is $G(\boldsymbol{\xi}, \mathbf{x_2}, t)$, this signal is time reversed and transmitted to $\mathbf{x_1}$, which records $G(\boldsymbol{\xi}, \mathbf{x_2}, -t) * G(\mathbf{x_1}, \boldsymbol{\xi}, t)$. Since the scatterers do not move and there is no flow within the medium, the wave propagation is reciprocal and then $U(\mathbf{x_1}) = G(\mathbf{x_1}, \boldsymbol{\xi}, t) * G(\mathbf{x_2}, \boldsymbol{\xi}, -t)$. Note that this time-reversal is identical to the correlation (equation 3.1). In this way, the mirror points can be seen as virtual sources. This concept is widely used in nearly all SI methods and the Green's function is therefore referred to as virtual-source response (e.g. Schuster, 2001; Bakulin & Calvert, 2014; 2006).

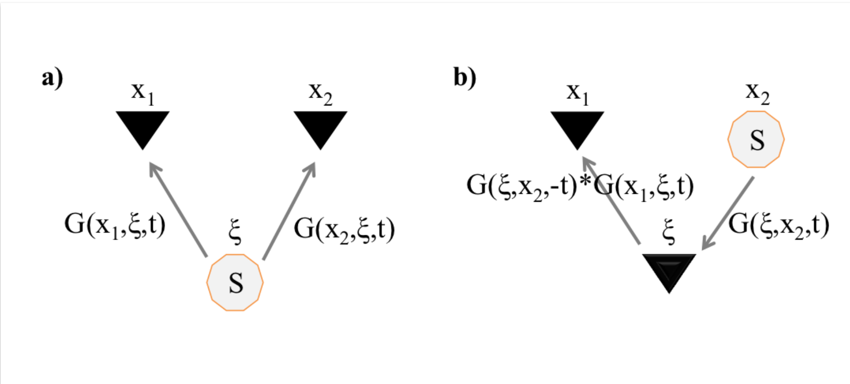

Figure 3.1: Illustration of the principle of time reversal - (a) The source placed at ξ emits a pulse recorded by the receivers located at x_1 and x_2. (b) The source placed now at x_2 emits a pulse received by ξ, which inverse the signal and re-emits it to x_1.

Helmholtz-Kirchhoff theorem offers a method to determine the wavefield within a volume if the wavefield is determined in all points on its surface. So now we consider a distribution of sources that acts like mirror points around the receivers instead of only one. $\mathbf{x_2}$ emits again an impulse but now in all directions, $\mathbf{x_1}$ records G($\mathbf{x_1}$, $\mathbf{x_2}$,t), which is the Green's function that we are looking for. All sources placed at $\boldsymbol{\xi}_\mathrm{i}$ invert the time of the signal received and re-emit it to $\mathbf{x_2}$. By reciprocity, $G(x_1, x_2, -t)$ is re-emitted as well. Once the wave is focused at x_2, the wavefield diverges again since there is no 'acoustic sink' in x_2. Therefore, the time-reversal experiment corresponds to the sum of Green's functions in positive and negative times and, as we have seen before, to the correlation between both receivers. Thus, we can write:

$$C(x_1, x_2) = \sum_i G(x_1, \boldsymbol{\xi}_i, t) * G(\boldsymbol{\xi_i}, x_2, -t) \cong G(x_1, x_2, t) + G(x_1, x_2, -t) \qquad (3.2)$$

Numerical experiments are in good agreement with the previous equation 3.2 (Derode et al., 2003). Often the sources are not symmetrically distributed around the receivers forming a perfect time-reversal device. In this scenario, the lack of symmetry is observed in the correlations as well and then the Green's function is not fully recovered. In highly heterogeneous media, the scatterers act like secondary sources and randomize the wavefield even in the presence of only one source. In any case, for seismic monitoring purposes a perfect reconstruction of the Green's function is not necessary (Hadziioannou et al., 2009).

In practice, the classical approach to compute correlations of wavefields recorded by two receivers in the time domain is given by the next well-known equation

$$CCG(t_{lag}) = \frac{\sum_{t=t_0}^{t_f} U_1(t + t_{lag}) \cdot U_2(t)}{\sqrt{\sum_{t=t_0}^{t_f} U_1(t + t_{lag})^2 \sum_{t=t_0}^{t_f} U_2(t)^2}} \qquad (3.3)$$

where $U_{\mathrm{j}} \equiv U(x_{\mathrm{j}})$ for j=1, 2. The denominator is the geometric mean of the energy, t is the recording time that varies within the time window [$\mathrm{t_0}$ - $\mathrm{t_f}$]. $\mathrm{t_{lag}}$ is the lag or lapse time, which represents the shift time applied to one of the records in order to obtain the positive (causal) and negative (anti-causal) contribution of the approximated Green's function. As have be seen, correlations can be interpreted as a travelling wavefield from one receiver to another. In this scenario, the lag time can be seen as the travel time of such wavefield.

Typically, the presence of spurious amplitudes and transient perturbations in the noise sources disturb the correlograms. In order to mitigate those effects, the correlations are computed in 1-hour-long segments and then, averaged (or stacked) during some days until a stable response of the medium is retrieved. For monitoring purposes, a fast stabilization is necessary that can be improved restricting the frequency band before correlating the signals (Roux et al., 2005).

To estimate the proper stacking duration, we can examine the waveform convergence to a reference response of the medium. This reference is commonly computed stacking the whole available period of correlations. Although in some cases, external perturbations can dominate the spectrum and we rather avoid that period, for instance, the strong volcanic tremor of the 2011 El Hierro eruption. The convergence is computed as the similarity between such reference and traces chosen randomly within the period under study as function of the stacking length. The longer the stacking, the more similar the resultant trace is to the reference. The similarity is quantified as the correlation at zero t_{lag} between the entire traces. In Section 4.2.1, we will show some examples of waveform convergences for different inter-station distances, frequency bands and type of correlation used.

The stacking process does not eliminate the influence of large signals such as earthquakes and instrumental issues. The classical correlation (eq. 3.3) depends on the amplitudes and large ones are therefore over-weighted. Furthermore, persistent monochromatic sources can also affect the correlations. As an example, the 26-s-period microseism from Gulf of Guinea is observed in correlations of seismic noise records on Europe, Unite States and Africa (Shapiro et al., 2006; Gaudot et al., 2016). The two methods typically applied before correlating signals to reduce those effects are: *one-bit normalization* and *spectral whitening* (e.g., Bensen et al. 2007). The first consists in a signal normalization sample by sample and the latter provides a frequency normalization giving the same weight to all frequencies. We refer to the correlations obtained applying these techniques as CCN in order to differentiate them from those computed without such pre-processing (CCG). The clear disadvantage that involves the aforementioned techniques is the loss of waveform details in terms of waveform distortion that can be crucial in some type of studies (Schimmel et al., 2011; 2018).

An alternative to the classical formulation of correlations is the phase cross-correlation (PCC; Schimmel, 1999). This approach measures the coherence between the instantaneous phases of two signals (ϕ_1 and ϕ_2), which are the phases of their corresponding analytic signals (S(t)). This analytic signal is formed by the seismic trace itself (s(t)) as the real part and its Hilbert transform (H) as the imaginary one. That is:

$$S(t) = s(t) + H[s(t)] = A(t) \cdot e^{i\phi(t)} \tag{3.4}$$

where A(t) is the instantaneous phase. Normalizing sample by sample, the summation of two analytic signals provides an amplitude-unbiased measure of the coherence. This formulation corresponds to the *phase stack* (Schimmel and Paulssen, 1997), which offers as well an alternative to the classical lineal stack that consists in a simple average. Following the same principles, the PCC takes the next form:

$$PCC(t_{lag}) = \frac{1}{2T} \sum_{t=t_0}^{t_f} \{ |e^{i\phi_1(t+t_{lag})} + e^{i\phi_2(t)}|^{\nu} - |e^{i\phi_1(t+t_{lag})} - e^{i\phi_2(t)}|^{\nu} \} \tag{3.5}$$

where T is the correlation window length. The power ν controls the sensitivity of the PCC and increases the signal-to-noise ratio. We use $\nu = 1$ throughout this thesis and the PCC is computed using the software package created by Martin Schimmel (`http://diapiro.ictja.csic.es/gt/mschi/index.html`).

Besides the advantage of amplitude-unbiased measures, the PCC is more sensitive to weak signal perturbations than the CCG and permits to discriminate close-by similar waveforms (Schimmel, 1999). Furthermore, there is no need to apply any of the previous pre-processing techniques and to remove recorded earthquakes from the data to ensure a reliable and accurate correlation analysis. In addition, the seismicity does not affect the PCC when it is located randomly around the selected receivers (D'Hour et al., 2016; Schimmel et al., 2011). Although strong seismicity gathered in a specific area can disturb the wavefield and yield thus variations in correlations.

Despite using the PCC, stacking correlations and applying a pre-processing, correlograms may be influenced by instrument issues, lack of samples in seismic traces (gaps) or unusual large amplitudes and yield misinterpreted result. For this reason, it is advisable to perform a (visual or implemented) inspection of the data and discard traces with anomalously big amplitudes and numerous long gaps.

It is worthy commenting that the most suitable method depends essentially on the study goals and other factors such as the chosen frequency band. In the two research lines of this thesis, we have compared thoroughly the results of the different correlation and stacking approaches in several frequency bands, lag-time windows and inter-station distances in order to select the appropriate approaches.

3.2 Temporal changes detection

The capability of SI to infer mechanical and structural changes in media can be summarized in the idea of that the retrieved Green's functions are time-invariant whenever the medium does not change over time. Hence, there is a reference response of the medium to seismic waves that can be used to compare it with correlations at different times and therefore infer variations. The two current techniques to monitor changes are the waveform similarity (e.g. DHour et al., 2015; Sánchez-Pastor et al., 2018) and waveform stretching (e.g. Brenguier et al., 2011; Hadziiounou et al., 2011; Obermann et al., 2014). The latter is older, more popular and derives from the doublet method (Poupinet et al., 1984) as well as the moving window cross-spectral technique (MWCS). In the following, I explain these techniques in detail arguing the advantages and downsides of each of them.

In both study cases, auto- and cross-correlations are computed for the vertical component of all seismic stations. Since the main and common goal is to monitor structural and mechanical changes, temporal accuracy is of upmost importance. For this reason, we employ the PCC instead of the classical approach (CCG and CCN). Stable noise responses are achieved in both cases stacking correlations linearly in a 3-day sliding window with a 2-day overlap obtaining daily noise responses of the medium. We expand the data processing steps proposed by Bensen et al. (2007) in Figure 3.2.

The type of correlation, stacking and other specifications chosen for the computation of stable correlations in both study cases are summarized in the following table:

Parameters	**Case 1**	**Case 2**
Frequency band	(2 - 6) Hz	(0.1 - 1)Hz
Correlation type	PCC	
Trace length	1 hour	
Lag time window	(-50, 50) s	
Nyquist frequency	25 Hz	
Gap samples threshold	10^4	
Stacking procedure	Linear	
Stacking length	3 days	

Table 3.1: Parameters used for the correlation computation

3.2.1 Waveform similarity

Structural changes in the medium entail variations in the location of the scatterers, which involve a change in the medium response as waveform distortions at a specific lag-time window. Those changes can be for instance an alteration of seismic discontinuities,

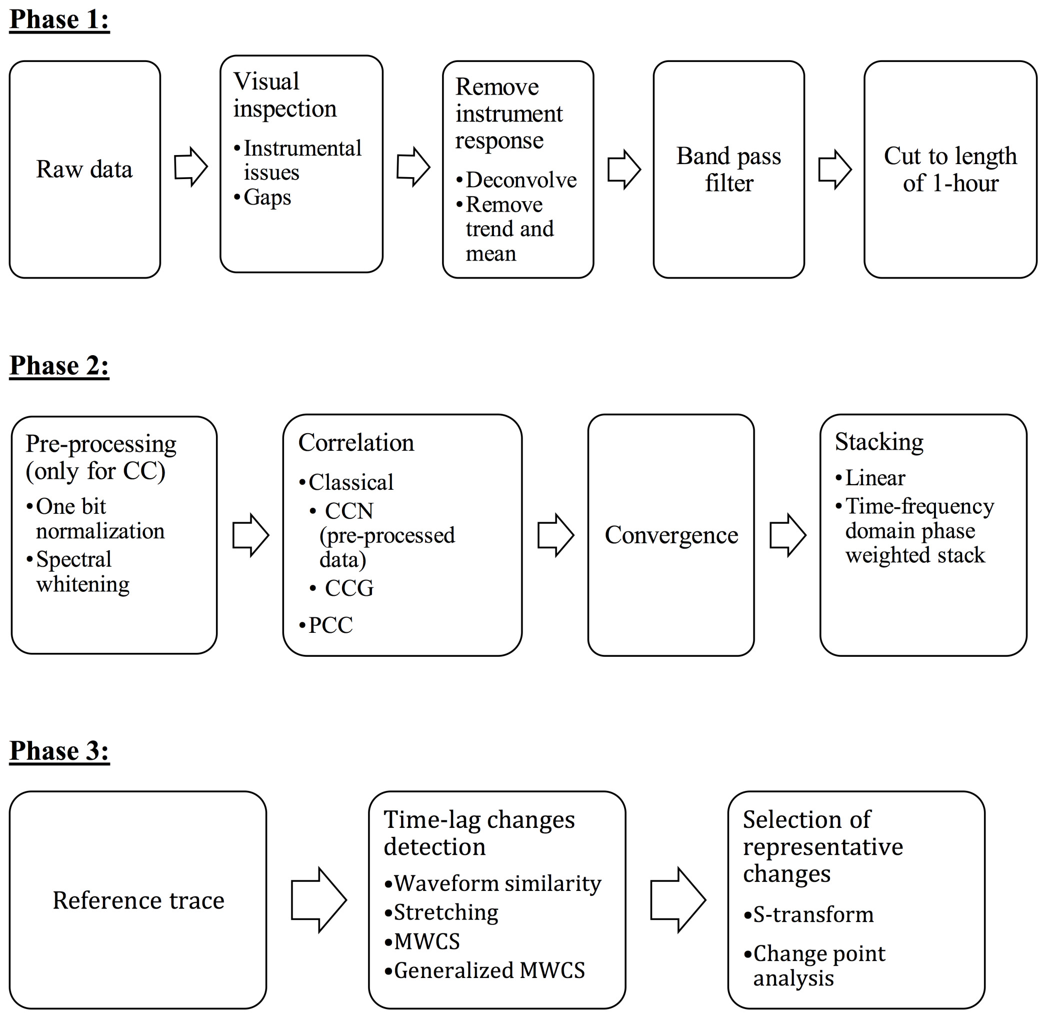

Figure 3.2: Workflow diagram of the data processing scheme. - Phase 1 outlines the steps involved before correlating signals. Phase 2 shows the steps needed for retrieving stable seismic noise responses. Phase 3 includes the steps for detecting lag-time changes.

new fractures and/or pore collapses. D'Hour et al. (2015) proposed to infer those changes through the analysis of the waveform similarity evolution. This similarity is computed as the zero-lag classical correlation between a reference function (CC^{ref}) and every 'current' correlation ($CC_i{}^{curr}$) at particular lag-time windows. These current correlations are obtained stacking 1-hour-long correlations during several days, those needed to achieve a stable response (3 days in our cases).

In this thesis, we employ this method with two slight modifications. The first, performing similarities using the PCC instead of CCG in order to increase the accuracy and, secondly, computing this observable in a sliding lag-time window (j) that goes across the entire coda. The waveform similarity then follows the equation:

$$S_{ij} = PCC[CC_j^{ref}, CC_{ij}^{curr}] \tag{3.6}$$

giving a NxM matrix where N is the total number of current traces and M the number of lag-time windows.

The use of PCC allows computing with great accuracy similarities and identifying tiny changes over time. Moreover, there are neither restrictions for applying this technique nor assumptions concerning medium perturbations are needed unlike with the next methods. On the other hand, the obtained results can vary depending on the reference function choice, which is a clear disadvantage. In the study of the 2011 El Hierro eruption we will show a comparison of the similarity results obtained from six different references (Section 4.1). Furthermore, it is worth mentioning that mechanical changes are observed as well through this approach although they cannot be distinguished from structural changes using only this technique.

3.2.2 Waveform stretching

Mechanical changes in the subsurface generally involve a time shift in coda waves (δt). Variations in seismic velocity, pore pressure and rock saturation are typical examples of mechanical changes. Assuming the same variation homogeneously distributed in the medium, the ratio $\frac{\delta t}{t}$ increases linearly in the coda and is equal to $-\frac{\delta v}{v}$, being v the seismic velocity of the medium (e.g Snieder & Hagerty, 2004; Sens-Schönfelder & Wegler, 2006; Minato et al., 2012). The traces are stretched and compressed until the correlation with the reference is maximum. The resulting stretched quantity (ϵ) corresponds to the relative velocity change in the medium $\epsilon = \frac{\delta v}{v}$ at day i. Following the CCG's equation, the correlation to maximize is referred to as correlation coefficient and takes the next form (Hadziioannou et al., 2009):

$$CC_i(\epsilon) = \frac{\sum_{t=t_0}^{t_f} CC_i^{curr}(t(1-\epsilon)) \cdot CC^{ref}(t)}{\sum_{t=t_0}^{t_f} CC_i^{curr}(t(1-\epsilon))^2 \sum_{t=t_0}^{t_f} CC^{ref}(t)^2} \tag{3.7}$$

A disadvantage of this technique is that it assumes a linear stretching of the waveform, which is not valid for spatially heterogeneous changes. To cope with this assumption, it is possible to calculate the velocity change in a moving lag-time window (j) and impose thus the linearity to a restricted area given by the lag-time. This way, we obtain a matrix $\mathrm{CC_{ij}}$, similarly to the previous technique. This correlation coefficient provides additional information about the structural changes; typically inferred from correlation losses, which are known as de-correlation (DC). Mainly, the coherence between the reference and current correlations should be high (>0.8) to obtain realistic and reliable velocity changes. A good reference choice therefore becomes essential.

Typically, studies based on stretching focus on one frequency band and lag-time window, where the mechanical changes are expected (Hadziioannou et al., 2011; Obermann et al., 2013b; 2015). Obermann et al. (2016) shows the importance of the lag-time window to measure perturbations in coda waves. At early lag times, surface waves are dominant in the wavefield and they are more sensitive to shallow depths, whereas at later lags body waves dominate the coda and these waves probe deeper. Hillers et al. (2015) emphasise the relevance of the frequency band on detecting velocity variations.

3.2.3 Generalized MWCS formulation

A preceding technique to estimate velocity changes is the doublet technique (Poupinet et al., 1984) that is also known as moving window cross-spectrum technique (MWCS, Frechet et al., 1989; Ratdomopurbo et al., 1995). The time shift between the possibly-altered correlation (at day i) and the reference, can be measured more precisely in the frequency domain. The phase of the cross-spectrum between both correlations depends linearly on the frequency and its slope is proportional to δt in the form:

$$\phi_j = 2\pi\delta t_j \tag{3.8}$$

where the subscript j indicates the samples in the frequency range of interest.

Each phase point is weighted during the linear regression through the coherence between the correlations (C_i) by the factor $C_i^2/(1-C_i^2)$. Clarke et al., 2011 modified such factor in $\sqrt{\frac{C_i^2}{1-C_i^2}} \cdot \sqrt{S_i}$, being $\mathrm{S_i}$ the corresponding cross-spectrum, in order to use weights as a function of the coherence and spectral energy. As previously mentioned, the velocity variation is the opposite of $\delta t/t$ under the assumption of a spatially homogeneous perturbation. Thus, the slope of δt_j versus t_j provides the relative velocity change. The results are more robust introducing a factor $1/e^2_{\delta t_i}$ to take into account the uncertainties of every δt_i during the inversion, which are calculated using the rule of propagation of errors (for further details, Clarke et al., 2011, Appendix A).

An important advantage of this technique is the scarce influence of clock errors in origin time of instruments, which is a common error in field experiments (Stehly et al., 2007). The waveform amplitude changes barely affect the results since the time shifts are estimated through the phase of cross-spectra. On the other hand, important disadvantages are the high signal-to-noise ratio required and the high coherence between reference and current correlations needed, which often is hard to achieved. Moreover, the selection of the lag-time window is of much importance and some preliminary tests have to be perform to avoid uncertain velocity estimations (Lecocq et al., 2014).

The reference bias of this technique was removed by Brenguier et al. (2014). The relative velocity changes are retrieved comparing the velocity estimates from MWCS beween all possible combination of days. In particular, the goal is to obtain a continuous time series of velocity changes ($\mathbf{m}$), whose components are defined as $\delta v_i = (v_i - v^{ref})/v^{ref}$. The difference between the velocity changes at day i and j is then:

$$\delta v_j - \delta v_i = \frac{v_j - v_i}{v^{ref}} = \frac{v_j - v_i}{v_i} \cdot \frac{v_i}{v^{ref}} = \delta v_{ij}(\delta v_i + 1) \cong \delta v_{ij} \tag{3.9}$$

where these values are given by $\delta v_{ij} = \frac{v_j - v_i}{v_i} = mwcs(CC_i^{curr}, CC_j^{curr})$. Repeating this procedure for all combination of days, the resulting values can be related to the desired vector $\mathbf{m}$ through

$$\begin{pmatrix} \delta v_{12} \\ \delta v_{13} \\ \delta v_{14} \\ \vdots \\ \delta v_{n-1\,n} \end{pmatrix} = \begin{pmatrix} -1 & 1 & 0 & 0 & 0 & ... \\ -1 & 0 & 1 & 0 & 0 & ... \\ -1 & 0 & 0 & 1 & 0 & ... \\ \vdots & & & & & \\ 0 & 0 & 0 & -1 & 1 & ... \end{pmatrix} \cdot \begin{pmatrix} \delta v_1 \\ \delta v_2 \\ \delta v_3 \\ \vdots \\ \delta v_n \end{pmatrix} \tag{3.10}$$

Identifying terms, the above equation is a typical inverse problem ($d = G \cdot m$), which can be solved by using a Bayesian least squares inversion (Tarantola, 2005). The vector $\mathbf{m}$ is thus

$$m = (G^t C_d^{-1} G + \alpha C_m^{-1})^{-1} G^t C_d^{-1} d \tag{3.11}$$

with α being a weighting parameter to balance both terms of the bracket. C_d is a covariance matrix formed of the uncertainties of δv_{ij} and C_m is *a priori* covariance matrix for the model **m**, which controls how the day i is correlated to day j by the characteristic correlation length (β) and whose expression is:

$$C_{m_{ij}} = e^{-|i-j|/2\beta} \tag{3.12}$$

The parameter β therefore allows us to calculate the velocity variations comparing more or less distant days in time and hence compute short- and long- term variations. The uncertainties of the velocity variation estimates are determined with the diagonal of the matrix $(G^t C_d^{-1} G + \alpha C_m^{-1})^{-1}$. The trace of the resolution operator ($R = m \cdot d^{-1} \cdot G$) quantifies how many variables are resolved by the dataset in comparison with the variables resolved by the matrix C_m. This value for a perfectly resolved system of equations is equal to the number variables.

3.2.4 S-transform

Passive monitoring requires to achieve a good balance between signal-to-noise ratio (SNR) and temporal accuracy. Stacking correlations for long periods of time increases the SNR but also involves a loss of temporal accuracy. In order to tackle this issue, several techniques have been developed such as adaptive filters (Hadziioannou et al., 2011; Schimmel & Gallart, 2007) and time-frequency stackings (Baig et al., 2009; Schimmel & Paulssen, 1997). These techniques are based on the S-transform (Stockwell et al., 1996), which is a multiresolution analysis relied on the Fourier theory that decomposes time series in the time-frequency domain (e.g. Gibson et al., 2006; Schimmel et al., 2011; Ventosa et al., 2008). The S-transform takes the next form:

$$S(\tau, f) = \int_{-\infty}^{+\infty} s(t) w(\tau - t, f) e^{i2\pi f t} dt \tag{3.13}$$

where s(t) is the time series of interest at a specific lag-time window, $w(\tau - t, f)$ is a Gaussian function centered at time τ and width proportional to 1/f.

Despite improving the SNR, the above mentioned techniques imply waveform distortions and loss of information in signals with rich-frequency content. The PCC contains an intrinsic filter that mitigates the incoherent signals in a careful way and generally, there is no need to process the data more through other techniques (Schimmel et al., 2011; 2018). Even then, time series of velocity variations and waveform similarity become very complex in some scenarios where the subsurface is continuously disturbed, i.e., where a stable seismic response of the medium is arduously retrieved. In this thesis, we propose applying the S-transform as a final processing step to such time series (Figure 3.2). Hence, the identification of potential changes becomes easier. I will show an application in the Reykjanes reservoir study (Section 4.2.1).

3.2.5 Change point analysis

Determining whether changes in the mean, standard deviation or median (among other statistics) occur in a function is the aim of the wide-studied 'change point problem'. The solution of this problem is a powerful tool that detects and characterizes function changes (Taylor, 2000). Typically in monitoring studies, a change stands out among other fluctuations that contain the time series of interest. However, those changes are identified visually and a change point analysis (CPA) would provide an unbiased discrimination of them. Different strategies have been proposed to address it such as binary segmentation (Scott & Knott, 1974), segment neighbourhood (Auger & Lawrence, 1989) and optimal partitioning (Jackson et al., 2005).

The common denominator of those strategies consists in minimizing a 'cost function' over several change points in different positions in the time series. This cost function is related to the statistical property under question. If the number of change points in the time series is known (K), this method searches in an interactive process K+1 segments among which the statistical property varies significantly (Figure 3.3). When N is unknown, a 'penalty function' is required in order to avoid overfitting. Otherwise, in the extreme case all points become change points. There exist several formulations of penalty functions as well (e.g. Akaike 1974; Schwarz 1978; Picard et al. 2005).

In particular, considering the mean as the statistic of interest, penalized contrast as penalty function (Lavielle, 2005), a linear computational cost (Killick et al., 2012) and K change points to be found, the function for minimizing turns into:

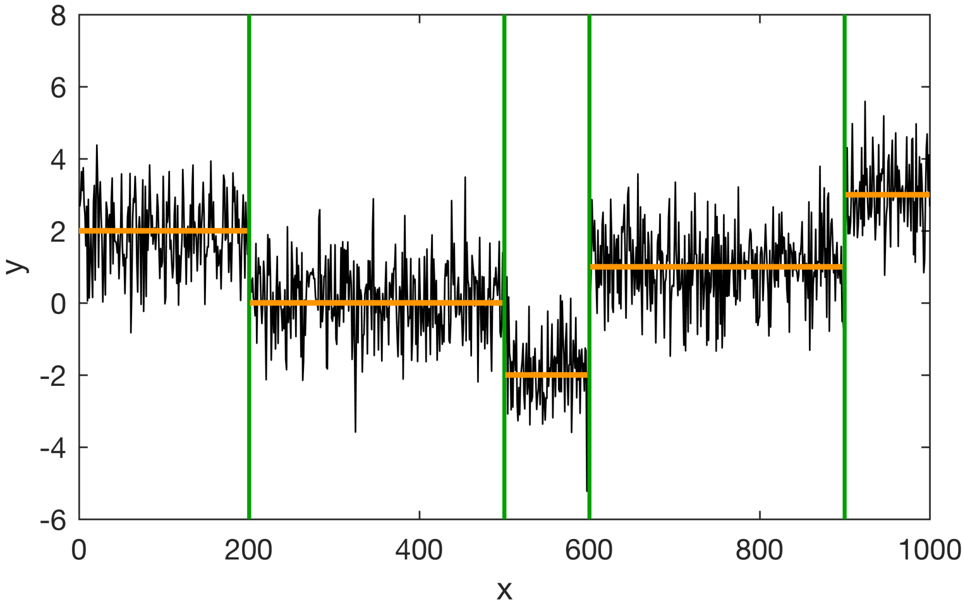

Figure 3.3: Example of changepoints in a time series - Function $(y(x))$ with four significant changes in the mean. These changepoints are represented by orange vertical lines and the mean of the different segments is shown as horizontal green lines.

$$J = \sum_{i=1}^{k-1}(x_i - \langle x \rangle_1^{k-1})^2 + \sum_{i=k}^{N}(x_i - \langle x \rangle_k^N)^2 + \beta K \tag{3.14}$$

being β the residual error threshold, βK the penalty function, N the total number of samples, k the change points and $<>$ denotes the expected value.

In this thesis, we propose this procedure in order to detect in which moments the mean of velocity variations or waveform similarities vary significantly. Thus, the identification of scattering properties of the subsurface can be automated with low computational cost. In the El Hierro eruption study (Section 4.1.1), we will show an application of this procedure.

3.3 Temporal changes imaging through sensitivity kernels

Studying the spatial distribution of subsurface properties is the main goal of a wide range of studies in Geophysics. In particular, imaging temporal changes in the scattering properties of media becomes essential for monitoring purposes such as volcanic eruptions. As explained before, CWI allows analysing the time evolution of scattering properties and quantifying the changes by de-correlation and time-shift variations. For locating the temporal variations, it is necessary to solve an inverse problem that relates those observables to perturbations in the subsurface ($\mathrm{x_0}$).

Coda waves are multiply scattered waves that travel through very complex paths from one station ($\mathbf{s_1}$) to another ($\mathbf{s_2}$) and therefore, there is no direct relationship between distance and travel time, unlike as in the classical seismic imaging using earthquakes. The desired relationship should describe the sensitivity of coda waves to changes in the subsurface, which will depend on the spent time in the perturbation. Pacheco & Snieder (2005) introduced the sensitivity kernels for acoustic media as a measurement of the volumetric density of travel time that multiply scattered waves spend at $\mathbf{x_0}$, which follows:

$$K(\mathbf{s_1}, \mathbf{s_2}, \mathbf{x_0}, t_{lag}) = \frac{\int_0^{t_{lag}} p(\mathbf{s_1}, \mathbf{x_0}, u) \cdot p(\mathbf{x_0}, \mathbf{s_2}, t_{lag} - u) du}{p(\mathbf{s_1}, \mathbf{s_2}, t_{lag})} \tag{3.15}$$

where $p(\mathbf{a}, \mathbf{b}, t_{lag})$ denotes the probability that waves travel from **a** and arriving to **b** during time $\mathrm{t_{lag}}$.

The previous probability can be approximated by the wavefield intensity measured in **b** and created by **a** at that time. Considering a highly heterogeneous medium, the energy transport of seismic waves can be seen as a diffusive process similar to the heat diffusion (e.g. Pachecho & Snieder 2005; Page et al., 1995; Schriemer et al., 1997). So, those probabilities can be described as intensity propagators, which can be approximated to the solution of the diffusion wave equation for 2D infinite media (Obermann et al., 2013b):

$$p(\mathbf{s_1}, \mathbf{s_2}, t_{lag}) = \frac{1}{4\pi D t_{lag}} e^{\frac{-||\mathbf{s_1} - \mathbf{s_2}||^2}{4Dt_{lag}}} \tag{3.16}$$

with D being the diffusion constant that depends on the heterogeneity degree. For semi-infinite media, the solution is composed by the sum of the infinite medium solution and its image from the free surface (Obermann, 2013).

This diffusion approximation is valid whenever the degree of heterogeneity of the propagation medium is high or the distance between stations is large enough. In other words, it is reached for $t_{lag} >> l^*/c$, being c the wave speed and l* the transport mean path, which represents the characteristic distance along which the seismic waves keep memory of its initial direction of propagation. The relationship between this parameter and the scattering mean free path is given by: $l^* = \frac{l}{1-\langle cos(\theta)\rangle}$, with θ being the angle between the incident and scattered waves.

A less restricted approximation is to consider as intensity propagator the two-dimensional solution of the radiative wave equation for isotropic scattering (Obermann et al., 2013b; Paasschens, 1997; Sato, 1993; Shang and Gao, 1988). The analytical solution for surface waves becomes:

$$p(\mathbf{r}, t_{lag}) = \frac{e^{-ct_{lag}/l^*}}{2\pi r}\delta(ct_{lag} - r) + \frac{1}{2\pi l^* ct_{lag}}\Big(1 - \frac{r^2}{c^2 t_{lag}^2}\Big)^{-1/2} exp\Big[l^{*^{-1}}\big(\sqrt{c^2 t_{lag}^2 - r^2} - ct_{lag}\big)\Big]\Theta(ct_{lag} - r) \quad (3.17)$$

where $\mathbf{r}$ is the distant between stations and Θ is the Heaviside function. The validity of this approximation is based on the isotropic scattering conditions, i.e., $l \cong l^*$. Note that the equation 3.17 tends to the diffusion solution (eq. 3.16) for $t_{lag} >> r/c$.

Implementing the previous equation for a cross- and auto-correlation (r=0), we obtain the Figure 3.4. As the maximum values depend on the inter-station distance, among other parameters, this figure shows a qualitative comparison of sensitivity kernels using different values of transport mean free path and lag time. As expected, at later lag times (Figure 3.4a and 3.4b), seismic waves probe larger areas beneath and around the seismic stations. In the same way, for larger transport mean free paths, seismic waves can travel further at the same lag time (Figure 3.4a and 3.4c).

Thus, the relationship between the measured de-correlation (DC) for two receivers ($\mathbf{s_1}$ and $\mathbf{s_2}$) and a local perturbation in the subsurface at $\mathbf{x_0}$ is given by:

$$DC(\mathbf{s_1}, \mathbf{s_2}, \mathbf{x_0}, t_{lag}) = \frac{c\sigma}{2} K(\mathbf{s_1}, \mathbf{s_2}, \mathbf{x_0}, t) \quad (3.18)$$

where c represents the wave speed of a effective mode composed by S and P waves (Obermann et al, 2013a; Planès et al., 2014) and σ is the scattering cross-section. This observable measures the likelihood of the seismic waves suffer scattering in the perturbation of interest, and it is quantified as an effective area. In other words, it is a proxy for the capacity of the perturbation to deviate waves. This measure depends

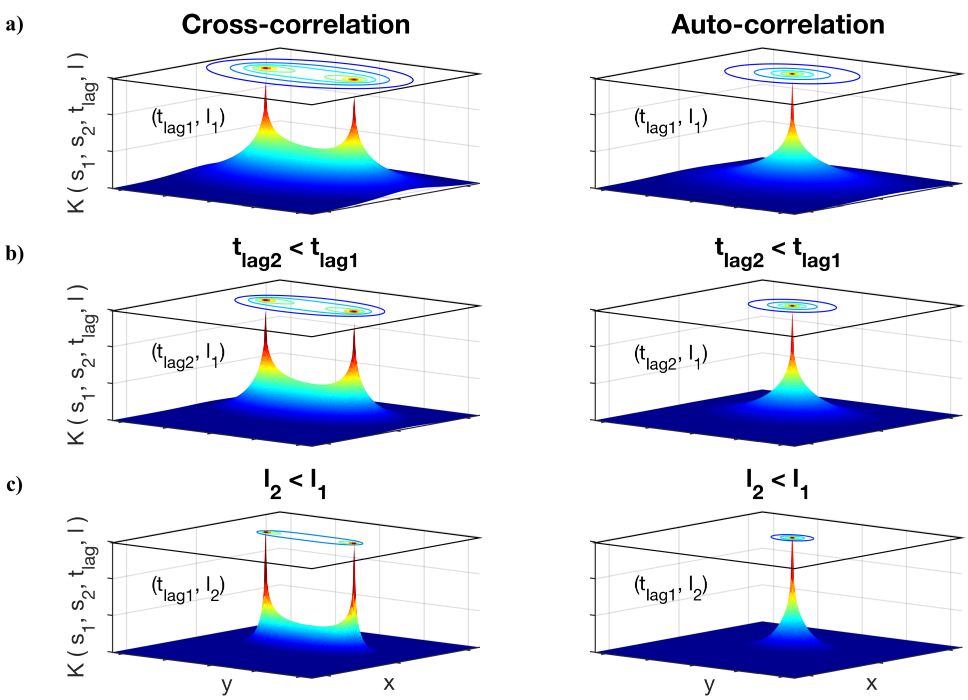

Figure 3.4: Sensitivity kernels - Comparison of spatial representation of the sensitivity kernels in the radiative transfer approximation for cross- (left) and auto-correlations (right) using different parameters. (b) Sensitivity kernels with same mean free path as (a) and shorter lag time. (c) Sensitivity kernels at same lag time as (a) and shorter mean free path. On top of every panel we show the sensitivity kernels by 2D contour lines. The two peaks indicate the position of the two seismic stations.

therefore on the size and strength of the perturbation. Note that the cross section has units of length since we use the radiative transfer solution in 2D.

The equation 3.18 can be re-written as $\mathbf{DC} = \mathbf{G} \cdot \mathbf{m}$, where $\mathbf{m}$ is the vector that contains the scattering cross-section in every point of the considered spatial grid and G is a matrix with components $G_{ij} = \frac{cK_{ij}}{2}$. The sensitivity kernels are weighted by the cell area of the input grid in order to obtain cross-section densities (km/km^2). The vector $\mathbf{m}$ can be retrieved by using a formulation of the minimum square method for linear problems as proposed by Tarantola & Valette (1982). This approach can be applied to relative velocity variations as well (for further information see Obermann et al., 2013a; Planès, 2013). We code and use this procedure in both study scenarios of this thesis to locate temporal similarity changes.

A more realistic description of the wave propagation intensity in scattering media can be achieved considering elastic media, non-diffusive energy transport and anisotropically scattering processes. Nevertheless, the sensitivity kernels do not have analytical solutions and should be computed numerically. On the other hand, we have considered surface waves although is well-known that coda waves are composed by a combination of body and surface waves (e.g. Margerin et al. 1999; Hennino et al. 2001; Obermann et al. 2013b). Recent studies build combined sensitivity kernels as a linear combination of surface and body wave sensitivities (Kanu & Snieder, 2015; Obermann el al., 2016; 2018).

4

Results and interpretation

In this chapter, I will show and explain the obtained results from the two different scenarios under study: The case of the 2011 El Hierro eruption and the Reykjanes reservoir. These are based on the same physical concepts of SI explained in the previous section. In the first scenario, we focus on the similarity analysis and use the change point analysis to detect temporal changes automatically. In the other, we combine the results of three different methodologies and show the advantages of using the S transform to better identify potential structural changes.

4.1 The 2011 El Hierro eruption

4.1.1 Results

The entire eruptive period of the 2011 El Hierro eruption was accompanied by a strong volcanic tremor with dominant frequencies oscillating from 0.5 to 1.9 Hz, although in some eruptive phases this tremor reached frequencies higher than 10 Hz (Tárraga et al., 2014). For monitoring purposes, noise sources should barely vary over time in order to avoid misinterpretations of the similarity changes. To this end, we select the frequency band (2 - 6) Hz, which does not overlap with the dominant frequencies of the tremor. Despite this, we exclude the eruptive period for the reference response computation in order to ensure avoiding signal contamination by the tremor. Prior to the eruption, the recorded seismicity was very intense and the PCC turns to be optimal since it provides amplitude-unbiased correlograms. Several tests have been performed to assure the PCC is not disturbed by the recorded seismic events and therefore, the no need of any extra pre-processing technique.

The waveform similarity evolution is calculated following the equation 3.6 and using a moving 7-s-long lag-time window with 3-s overlap. We average positive and negative lag time similarity values. An example of an auto- and cross-correlation are shown in Figure 4.1c and 4.1d. The reddish colors of the similarity mean that, given at specific day, the reference and the current response are well correlated whereas cold colors mean little correlated traces. The surface deformation modulus of the GPS station FRON is overlapped in black. We divide the two years of the study into nine periods (indicated with roman numbers below the Figure 4.1c). Comparing these two figures, the waveform similarity values from the auto-correlation vary between -0.5 and 1 and the cross-correlation shows values in a narrower range. Thereby, the AC seems to be more sensitive and shows the similarity variations clearer over time.

The correlations, or virtual-source responses, are no correlated with the selected reference at any lag time during the period II (Figure 4.1c and 4.1d). This period corresponds to the eruption and in turn, to the strong volcanic tremor. To analyze the effect of the tremor on the similarity analysis in detail, we calculate the seismic energy for the station CCUM at 1 and 4 Hz and represent those curves together with the similarity time-series in a window of 50 days length at the beginning (Figure 4.1a) and end (Figure 4.1b) of the eruption. 1 Hz is the average dominant frequency of the tremor and 4 Hz the center frequency of the chosen frequency band. The seismic tremor started suddenly and at the same time as the eruption whereas its end was erratic. The similarity values around day 35 (2012) show a clear increase that coincides with a rise in seismic energy, which indicates that similarity values are affected by the seismic tremor. At all lag-time windows and for all stations couples, the similarity values increase abruptly on 46 (2012), around 20 days before the official end of the eruption announced by PEVOLCA.

The sudden surface deformation raise in periods IV and VI coincide with low waveform similarity values in a wide lag-time range (Figure 4.1c and 4.1d) and match in time with two magmatic intrusions inferred throughout 2012. While the similarity values in period VI are low below 12 seconds of lag time, the low values in period IV extend in all lag times; quite similar to the eruptive period (II). The 5 cm decrease on the surface deformation at the beginning of period VIII is accompanied by a loss of

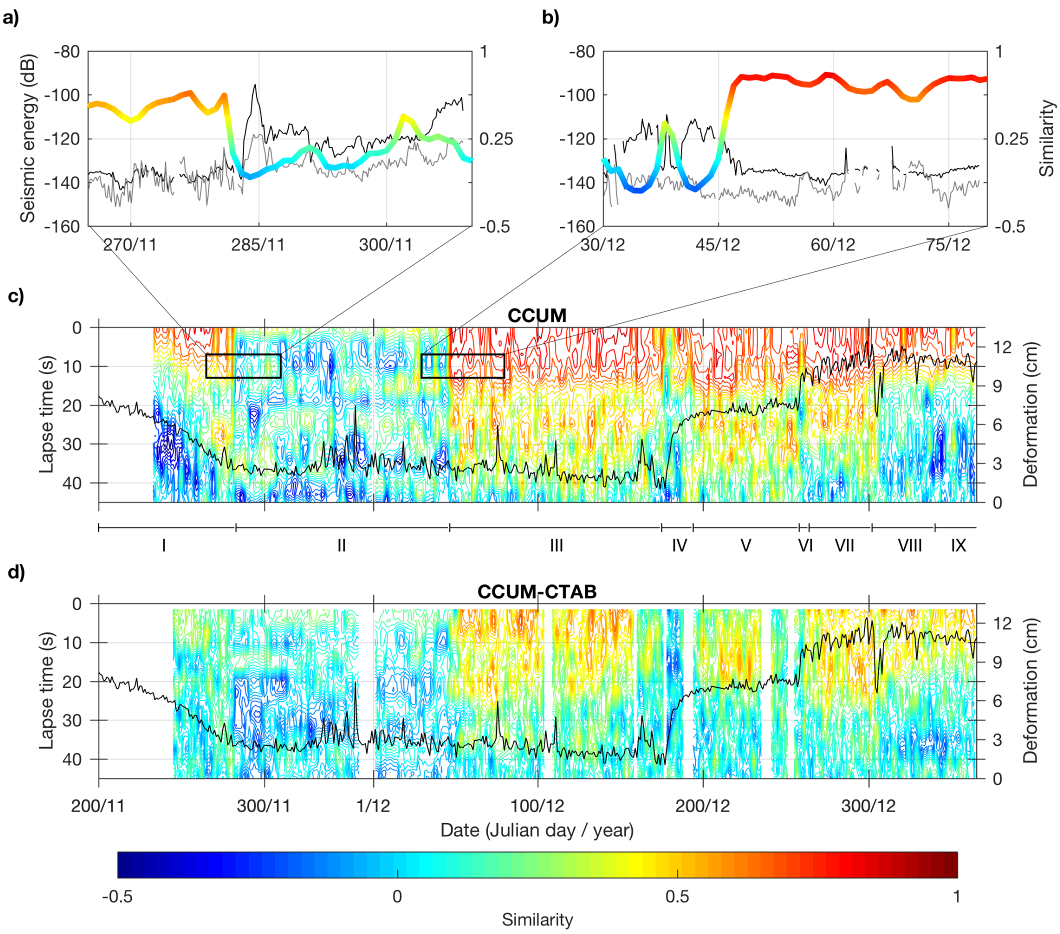

Figure 4.1: Time evolution of waveform similarity during the 2011-2012 El Hierro eruption - (c, d) Lag time-dependent waveform similarity for the 2 years of study from auto-correlation (CCUM) and cross correlation (CCUM-CTAB). The black line represents the modulus of the three components of the surface deformation estimated from GPS station FRON. We mark nine periods of volcanic activity (IIX). (a, b) Zoom into the waveform similarity around 10-s lag time for the beginning and end of the volcanic eruption. The seismic energy calculated for CCUM is shown at 1 (black) and 4 Hz (gray).

similarity for lag times below 12 seconds. Furthermore, it can be observed in Figure 4.1c that the auto-correlation shows a rich similarity time series in the pre-eruptive period (I). In particular, the change around day 274 (2011) that concurs with a small but clear surface deformation increase (Figure 4.1, I, 25- to 30-s lag time).

As we have be seen in the similarity equation (eq. 3.6), the waveform similarity depends on a reference. To asses the robustness of our results, we compute five refer-

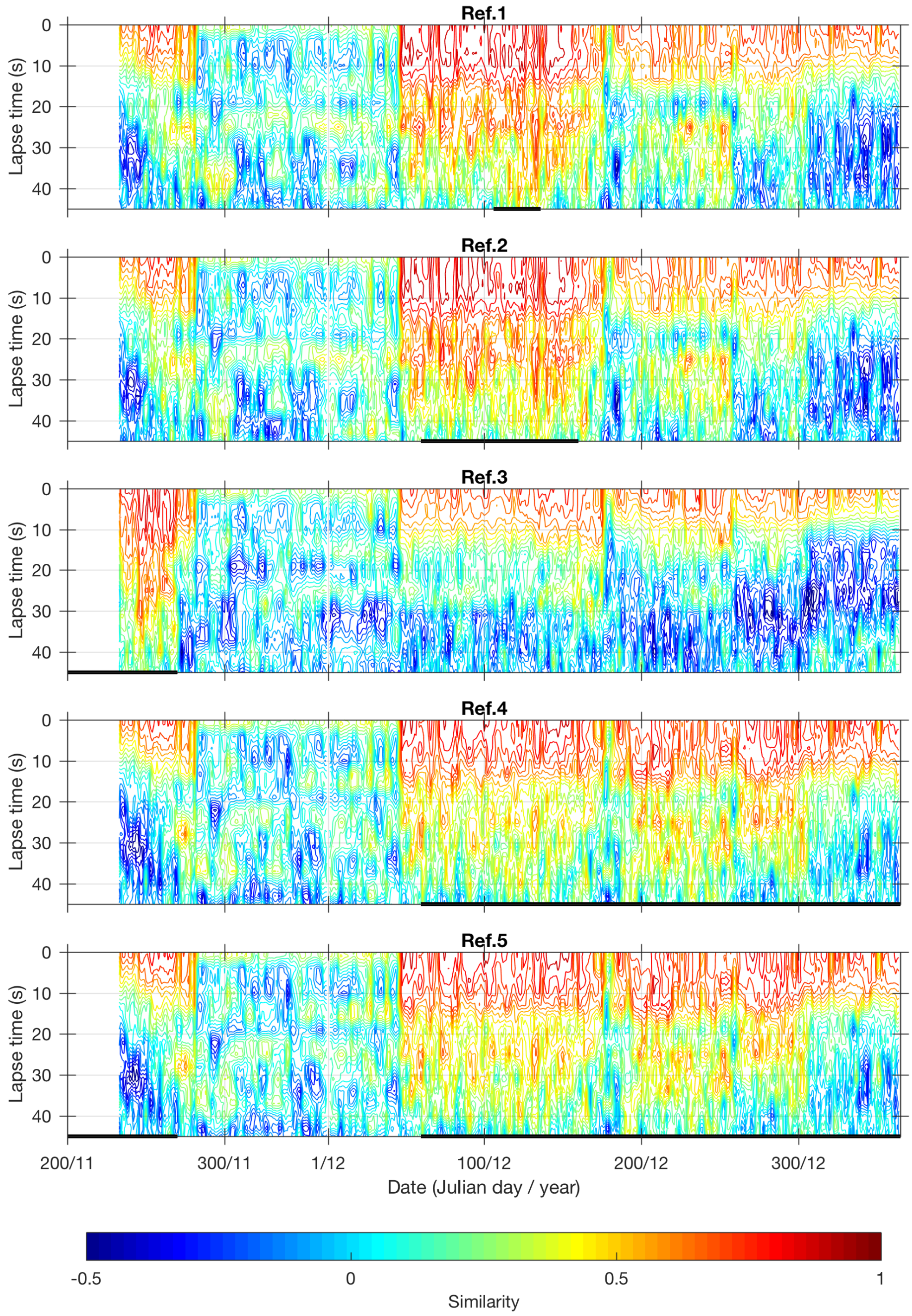

Figure 4.2: Comparison of time evolution of waveform similarity for five different reference traces. - The seismic station used is CCUM. The days stacked to obtain the references are highlighted by the black and thick line in the horizontal axes.

ences (besides the one used in the Figure 4.1) and calculate the time evolution of the similarity values for the whole period under study (Figure 4.2). As can be seen, the aforementioned features remain for all references. However, the reddish colors (high waveform similarity) appeared around the stacked period for computing the reference as expected. Consequently, the absolute values are hardly interpretable and we focus on the relative changes.

We now focus on the pre-eruptive period in order to discriminate precursory signals. Most of seismic events recorded prior to the eruption were at around 10 km of depth, at which the largest structural and mechanical variations are expected. We consider an apparent velocity for scattered waves of 1 km/s for this area and selected frequency band (Gorbatikov et al., 2013; Garca-Yegas et al., 2014; Meier et al., 2010). We address the study focusing on auto-correlations since they seem to be more sensitive to medium changes. The lag-time window should be therefore around 20 seconds to reach the target depth.

In Figure 4.3, we show the similarity curve computed between 16 and 22 seconds of lag time in the pre-eruptive period for all available seismic stations. In some of them, we can distinguish clearly a change around day 274. In particular, a similarity drop in CTAB and CHIE, and a similarity rise in CTAN and CJUL. The CPA explained in Section 3.2.4 allows us to know the statistical relevance of such change and also detect time periods with average similarity statistically different between each other.

We fix the significance of that method in 1.5-fold the characteristic standard deviation, here defined as the standard deviation of the similarity time series in a calm period. In this case we choose the period III as calm period since the volcanic activity was absent and the seismicity was very scarce. The obtained results are represented by orange lines in Figure 4.3. For all stations excepting for CCUM, the change on day 270 marks a period of 10 days length statistically different from the others. The CPA finds other periods consistent in several auto-correlations where the waveform similarity is different. For instance, a brief period of a few days before the eruption is discerned in all auto-correlations.

At this point, we have obtained the time evolution of the waveform similarity during the 2011 El Hierro eruption in 2011 and 2012. We have further detected some pre-eruptive phases where the scattering properties of the medium change. In the following, we map the probabilistic spatial distribution of the location of all similarity

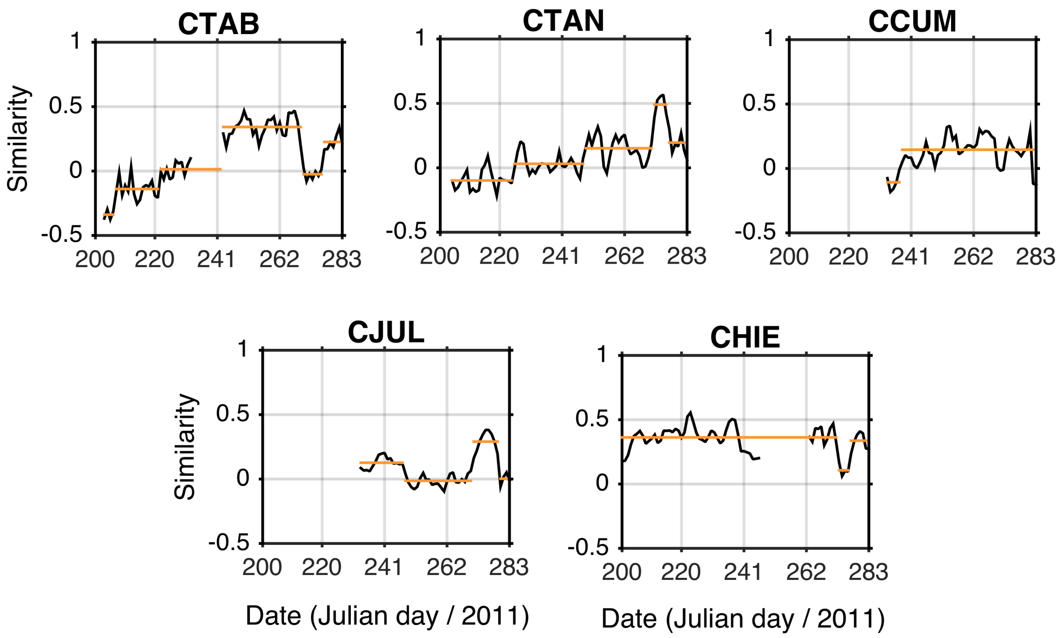

Figure 4.3: Statistical discrimination of pre-eruptive phases for the 2011 El Hierro eruption - Similarity time series at 16-22 seconds of lag time for all auto-correlations. Orange, horizontal lines mark time periods delimited by abrupt changes in the average of the waveform similarity, as obtained from the change point analysis.

variations for both years (supporting information M1, Sánchez-Pastor et al., 2018), which are obtained through probabilistic sensitivity kernels (see Chapter 3). For their construction, we need to assume two main parameters: the scattering mean free path and the wave speed in the studied area.

We use a rough approximation of the transport mean free path of 30 km that we estimate comparing with attenuation studies in other volcanoes (Del Pezzo et al., 2001; Obermann, Planès, Larose & Campillo, 2013; Prudencio et al., 2013). We also consider dominance of surface waves whose effective wave speed is 1 km/s as we commented previously. Hence, such kernels can be built by the two-dimensional radiative transfer theory (equation 3.17).

We invert the similarity changes measured as the absolute difference between the current similarity at a specific lag-time window and the average similarity in the calmest period (III) at the same lag time. In this way, we compare the waveform similarities of each station with their corresponding maximum values. The sampled region in the subsurface by seismic waves depends on the selected lag-time window. The larger the lag time, the larger the travel path. We then consider lag times from 5 to 45 s and sliding lag-time windows of 10-s length with a 50% overlap.

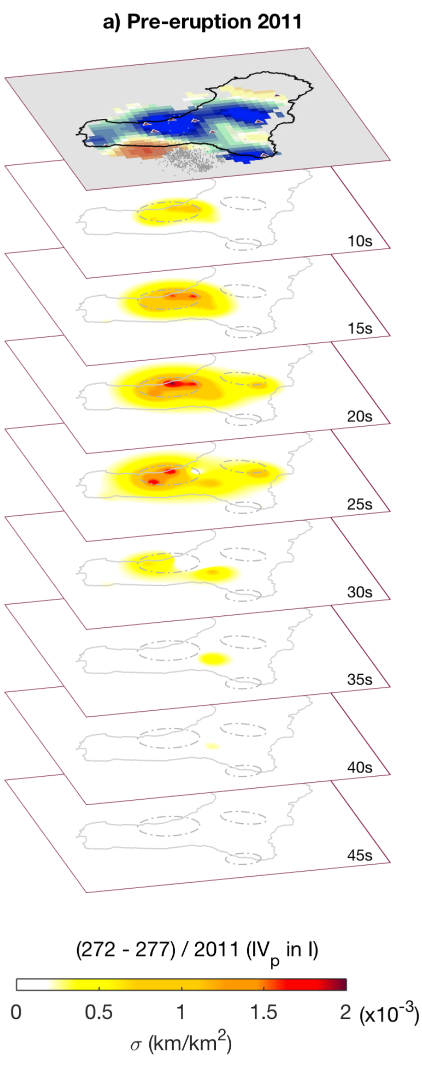

Figure 4.4: Scattering cross-section density maps at various lag times for different periods of the volcanic eruption - (a) Prior to the eruption. (b, c) Premagmatic and comagmatic intrusion of June 2012. (d, e) Premagmatic and comagmatic intrusion of September 2012. (f) Calmest period. (g) Preintrusion of January 2013. The days averaged are indicated below every panel together with their corresponding time period. The seismicity of the corresponding time periods is marked by gray dots. First panel in (a) represent a P wave tomography at 4- to 5-km depth (adapted from Martí et al., 2017). The gray dashed circles in subsequent panels highlight the regions with 8% of Vp perturbations.

In Figure 4.4, we show the scattering cross-section density maps for the pre-eruptive change around 274/2011 (a), as well as the intrusive periods throughout 2012 (c, e) and their previous stage (b, d), including for the intrusion of January 2013 (g). Furthermore, we show the results in the calm period III for comparison. We adapt the P-wave tomography at around 5 km of depth from Martí et al. (2017) in Figure 4.4a and highlight the regions with 8% of Vp perturbations. The time windows in which the inversions are computed are indicated below each panel in addition to the period of Figure 4.1c to which they belong. For pre-intrusions, the time period is selected from the day when the scattering cross-section becomes significant until the day before the corresponding intrusion.

We can clearly see in Figure 4.4 that the location of the similarity changes in all cases is in the interior of El Golfo Valley; in particular, around the Tanganasoga volcano, the scattering cross-section density values are up to $2 \cdot 10^{-3}$ km/km^2. The cross-sections are also significant in the extinct volcanic area of Tiñor at larger lag times although with smaller values. As can be seen in Figure 4.4a, those regions coincide with the location of seismic velocity perturbations. The subsurface effects due to the magmatic intrusions were noticeable 24 and 14 days before the intrusions of June and September 2012 respectively. In all the studied periods the maximum values are reached between 15 and 25 seconds of lag times and vanish at larger lag times. Also note that the seismic events recorded during the intrusions do not appear in the regions with high cross-section density (Figure 4.4a, 4.4c and 4.4e), confirming that the PCC measurements are not affected by the local seismicity.

For some volcanoes, the mean free path is determined to be less than 1 km by cause of strong heterogeneity in the medium (Wegler & Lühr, 2001, Yamamoto & Sato, 2010). Due to the lack of estimates of transport mean free path at $(2 - 6)$ Hz and the effective wave speed in El Hierro, we test several values and compare the resulting scattering cross-sections regarding the change on day 274 (2011), when the largest similarity change within the pre-eruptive period occurred. Concretely, we use l=1 and 120 km (Figure 4.5b and 4.5c) and c=3 and 5 km/s (Figure 4.5d and 4.5e), and compare them with the results for the previously chosen parameters (Figure 4.5a). The difference between the obtained cross-sections are basically the size of the sampled portion of the subsurface and the absolute value estimates. The most important result is that the horizontal location of the changes remain in the interior of El Golfo Valley.

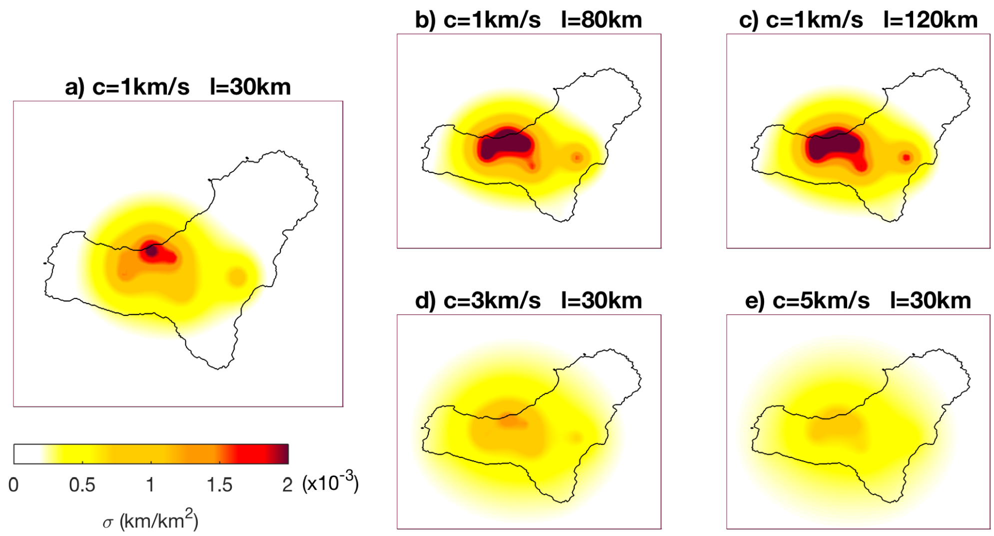

Figure 4.5: Comparison of the scattering cross-section distribution with different parameters of the medium - (a) Parameters chosen in the study. (b-c) Transport mean free path of 80 and 120 km respectively and wave speed fixed at 1km/s. (d-e) Wave speed of 3 and 5 km/s respectively and transport mean free path fixed at 30km. The time period of these inversions is 272 - 277 (2011). The lag-time window is centered at 20 seconds.

The seismic records in this study are scarce before the eruption and the seismic network is inhomogeneously distributed around the island. The bulk of the stations is located in the central-north part of El Hierro; around the Tanganasoga volcano. This can yield a preferential location of the temporal changes during the inversion. To check this possible effect, we calculate the inversion by removing systematically every single station of the same change analysed in Figure 4.5 (Figure 4.6). The distribution of the cross-sections varies slightly despite the sparse seismic network. The seismic station that has more influence in such distribution is the one on top of the main change, as expected. Although the maximum values and their location barely change.

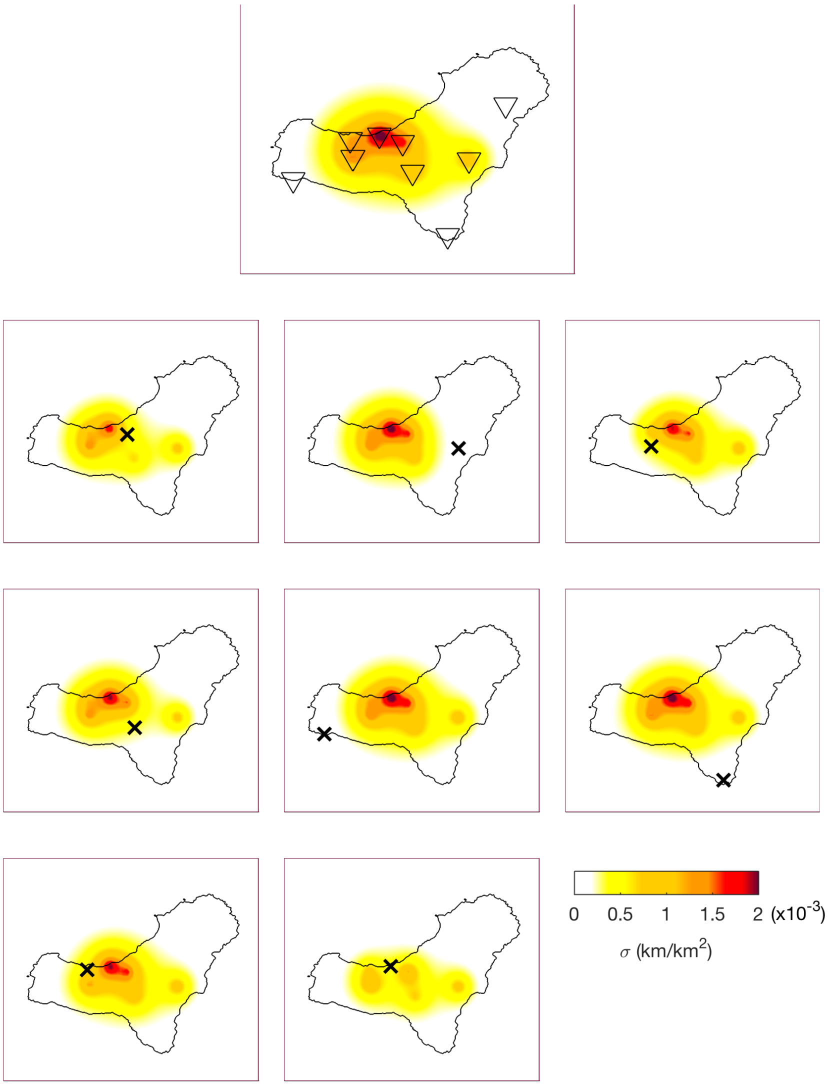

Figure 4.6: Seismic network distribution effects on the location of temporal changes - Scattering cross-section density maps of the same temporal change and lag-time window of Figure 4.5. The black cross indicates the seismic station discarded for every inversion. At the top, the original cross-section map and all the seismic stations, which are depicted by inverted triangles.

4.1.2 Interpretation

The volcanic eruption in El Hierro that led to the young Tagoro volcano was the first eruption in the Canary Islands tracked in near real-time through different instrumentation since its beginning. Several research groups have studied in great detail the processes associated with this eruption employing different geophysical approaches, such as tomography models (García-Yeguas et al., 2014; Martí et al., 2017), ultrasound methods (Gorbatikov et al., 2013) and geodetic analysis (López, et al., 2017b) among others. However, this volcano is submarine and the seismic unrest started in El Golfo and was migrating till the final place where the eruption took place. The seismic network was therefore placed on land a few weeks prior to the eruption and could not be distributed around the volcano, as it is typical in studies based on CWI. Besides, the volcano dimensions are smaller than those typically monitored using this approach. Thereby, working with seismic noise recorded on the island during this widely studied eruption has provided an excellent opportunity to show the potential of SI in volcanic monitoring under particular conditions.

The waveform similarity evolution during 2011 and 2012 has provided valuable information about the interior dynamics of the Tagoro volcano. For instance, PEVOLCA notified the official end of the eruption on 5 March 2012 (day 65), when most seismic and volcanic activity ceased. The abrupt similarity change observed on the 15th of February (46/2012) marks the end of the main magma emission; 20 days before the official end. This reflects the importance of using CWI in places where the data acquisition is restricted, such as the case with submarine volcanoes.

The pre-eruptive period was analysed in depth by López et al. (2012). In this study, the authors discriminate five pre-eruptive phases based on the evolution of seismicity, surface deformation, and ^{222}Rn emissions, among other measurements. Those phases are summarized in Table 2.1 and compared to our pre-eruptive phases, discriminated by the change point analysis, in Figure 4.7.

As can be seen, both results are in great concordance. The first days of seismic records for the seismic stations CTAB and CCUM compose a period with similarity average different than the next ones. This may be due to the sensor stabilization, which often lasts some days and should not be interpreted as a temporal medium change. However, the phase (V_p) is detected by all auto-correlations and corresponds to a short period of calm before the eruption. Some volcanoes show this characteristic feature that can last from several weeks to hours (e.g., McNutt, 1996).

The acceleration of the volcanic processes (IV_p) is observed also by all stations, except for CCUM, as a similarity change of amplitude around 0.5. It is accompanied

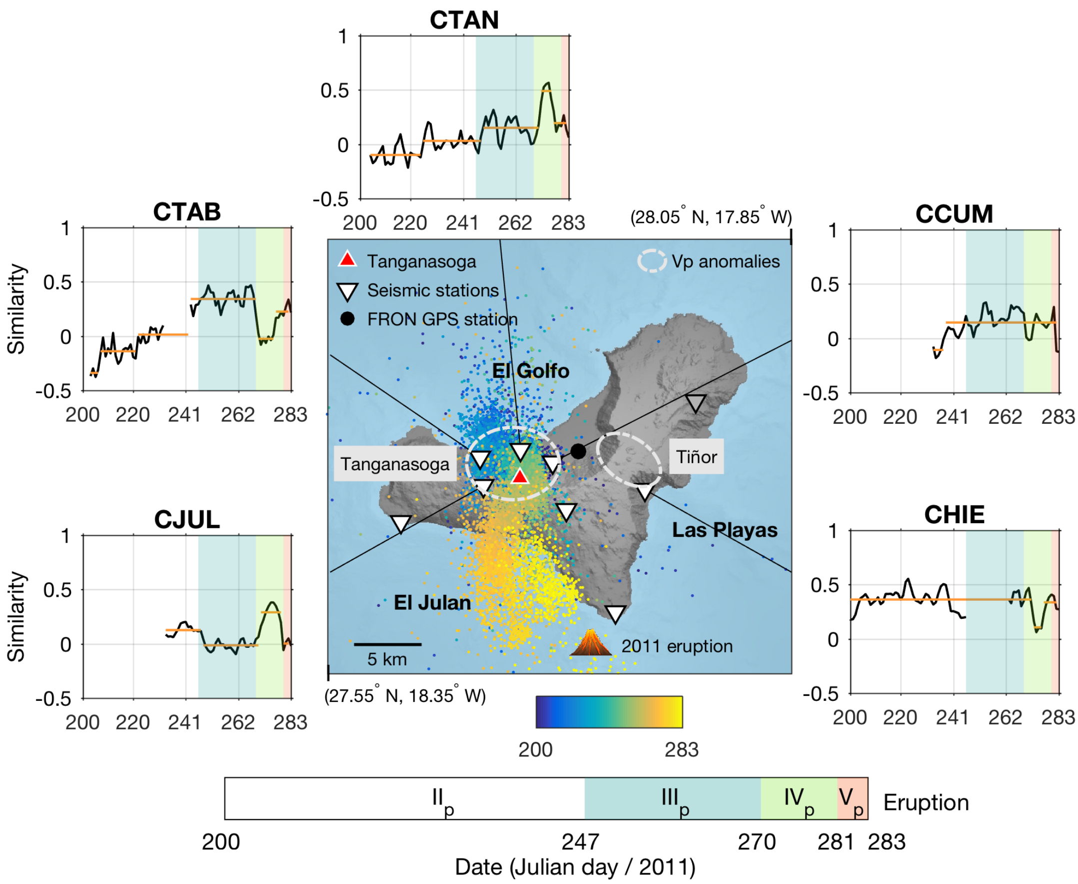

Figure 4.7: Detected pre-eruptive phases of the 2011 El Hierro eruption - Inner part: Map of El Hierro Island. Inverted triangles mark the location of the seismic stations. The station in gray has been discarded due to problems with its frequency content. The black dot marks the GPS station FRON. The time evolution of the seismicity prior to the eruption in 2011 is marked with colored dots. The gray dashed circles highlight the Tanganasoga and Tiñor volcanic areas that are marked by high Vp anomalies (Martí et al., 2017). Outer part: Similarity curves at 1622 s of lag time for various auto-correlations. Orange, horizontal lines mark time periods delimited by abrupt changes in the average of the waveform similarity, as obtained from the change point analysis. Background colors indicate the preeruptive phases of López et al. (2012) and are labeled with the subscript p.

by a surface deformation of 1.5 cm (Figure 4.1, phase I) and a drastic seismic energy release, which have been caused by the over-pressurized magma that crossed the mantle-crust boundary (e.g. López et al., 2017b; Meletlidis et al., 2015). This magma upwelling is detected by the similarity analysis two days before it was perceptible by GPS stations.

Several stations show a similarity change on day 220 (2011); in the middle of II_p

(Figure 4.1). López et al. (2017b) performed a detailed study of the pre-eruptive period of this eruption through Real-time Seismic Amplitude Measurement (RSAM) analysis. They observed a variation around this date in several frequency bands although they left the underlying processes uncommented (further details in Figure 5 of López et al., 2017b). We therefore consider the change on day 220 to be reliable and it can be interpreted as structural changes derived from volume variations of magma upwelling beneath the crust.

The characteristic seismicity migration marks the beginning of phase $\mathrm{III_p}$. The largest computed scattering cross-section in the two years study was detected around the Tanganasoga volcano three days before the unrest migration started. This subsurface imprint indicates strong structural changes caused by overpressure in the rock matrix due to the magma accumulation below this volcano. After that moment, the magma found paths to travel southward encountering several stress barriers on its way that carried the magma until the final site of the eruption (Martí et al., 2017). Due to the sparse seismic dataset in those days and to the geometry of the seismic network, we cannot track the seismicity migration with our approach.

It is important to highlight that we perform the CPA in one lag-time window, concretely where we expect the largest variations. Despite the obtained results are in great concordance with the bibliography regarding the pre-eruptive period, the results can be more robust by employing the CPA systematically in several lag-time windows and interpreting the results jointly. In future studies, this aspect should be addressed.

With regard to the pre-eruptive change locations, the maximum values of the scattering cross-section are mainly around two areas: The Tanganasoga volcano, below which the magma accumulation zone is inferred, (García-Yeguas et al., 2014; Gorbatikov et al., 2013; Martí et al., 2017), and the extinct volcanic area of Tiñor. We interpret the latter as another point of magma upwelling that could not reach the surface. Furthermore, this anomaly appears at later lag times. So, this second point of magma upwelling should be deeper. This interpretation agrees with several studies that point out a smaller and low seismic velocity zone located in this region (Gorbatikov et al., 2013; Martí et al., 2017).

On 11 October 2011, the eruption started near La Restinga town and the Tagoro volcano grew in two main episodes interrupted by destructive phases in form of collapses (Somoza et al., 2017). These episodes likely produced alterations in the scattering properties of the subsurface. However, the entire eruptive period was accompanied by an intense volcanic tremor (Figure 2.5a) that does not allow us to study these months of magmatic activity using SI, even though the chosen frequency band does not overlap the dominant frequencies of the tremor.

Throughout 2012, two episodes of intense seismic activity and large surface deformations were manifestations of magmatic intrusions beneath El Hierro (Díaz-Moreno et al., 2015; García et al., 2014; González et al., 2013; Klügel et al., 2015; Meletlidis et al., 2015; Telesca et al., 2016). These events correspond to periods of low waveform similarities (IV and VI; Figure 4.1c-d), however they are slightly different. The first, in June, produced a lack of correlation in the entire coda (also in the direct waves recorded at very early lags) and shows a similarity pattern quite similar to the eruptive period (II). This episode has been a focus of controversy and discussed by several authors (Blanco et al., 2015; Nemesio et al., 2014; 2015). The debated question is if the magma upwelling culminated in a small eruption or the magma did not reach the surface. Using only SI, we cannot shed light on this question, although we provide one observation more to consider.

At the end of 2012, other magmatic eruption was inferred (e.g. Díaz-Moreno et al., 2015; Telesca et al., 2016). Some days earlier, a similarity decrease is observed between 12 and 50 seconds of lag time (period IX, Figure 4.1). The previous surface deformation decrease on day 302 (period VIII) is an artefact caused by a strong storm that lasted 10 days and affected the entire Canary Archipelago (Spanish Meteorological Agency, http://www.aemet.es). The seismic stations could be affected by the fast winds yielding some alterations in the measurements although there is no record with this information.

On the other hand, this similarity decrease is observed below 12-s lag time however, instrumental issues are expected to alter completely the correlograms. Accordingly, we do not relate these negative similarity values to atmospheric instabilities. Another reason for considering that similarity decrease reliable is its spatial distribution around the magma accumulation zone (supporting information M1, Sánchez-Pastor et al., 2018). The storm affected the entire archipelago and therefore, the change should be homogeneously distributed around the island.

In general terms, the seismicity does not affect our results since we have used the PCC. In Figure 4.4, we see how the maximum cross-sections and seismic events do not coincide. Moreover, we observe for all intrusive phases, that the locations of the pre-intrusion (with little to no indicative seismicity) correspond to the location of the final intrusion location, highlighting the potential of CWI for precursory alarming.

The mean free path, seismic wave speed and lag time window control the diffusive halo of coda waves (Figure 3.4). Furthermore, in Figure 4.6 we have shown that the results hardly depend on the input parameters since the spatial distribution of the scattering cross-section barely varies. Thus, the similarity analysis using the PCC and the sensitivity kernels allow us to study volcanic eruptions with sparse data sets and limited knowledge of the region. This procedure combined with a statistical analysis such as the change point analysis can be automated and used in early hazard assessment.

4.2 Reykjanes reservoir

4.2.1 Results

The Reykjanes reservoir has been exploited since the fifties and monitored by several seismic networks. The heat-mining in the power plant may cause variations in the elastic properties of the surrounding medium. Here, we focus on the years 2014 and 2015, when the IMAGE project was deployed. In this study, the seismic network is better distributed around the area under study (Figure 2.7) than in the previous case. Moreover, there is not any coherent noise source that limits the frequency band choice. The challenge, in this case, is to find structural and mechanical changes in a constantly perturbed medium for several decades with the absence of a 'calm' period.

As the production and injection rates at RGS often vary abruptly, we need to minimize the days stacked for the stabilization of the correlations. In order to achieve the best accuracy, we analyse the waveform convergence of two seismic station couples with different inter-station distances at three frequency bands. In addition, we compute the correlations through three different approaches, PCC, CCG and CCN (for further information about these methodologies see Chapter 3).

The reference trace is obtained stacking the correlations corresponding to the days with the highest and mostly constant production rate (excluding the days 210-300/2014). In this way, the abrupt production drops that likely have significant effects in the medium are avoided for the reference computation. We then calculate the PCC between the entire reference and the traces chosen randomly within the whole period under study as function of the stacking length. To show the robustness of the convergence, we repeat this procedure ten times for each stacking length. The obtained results are depicted in Figure 4.8.

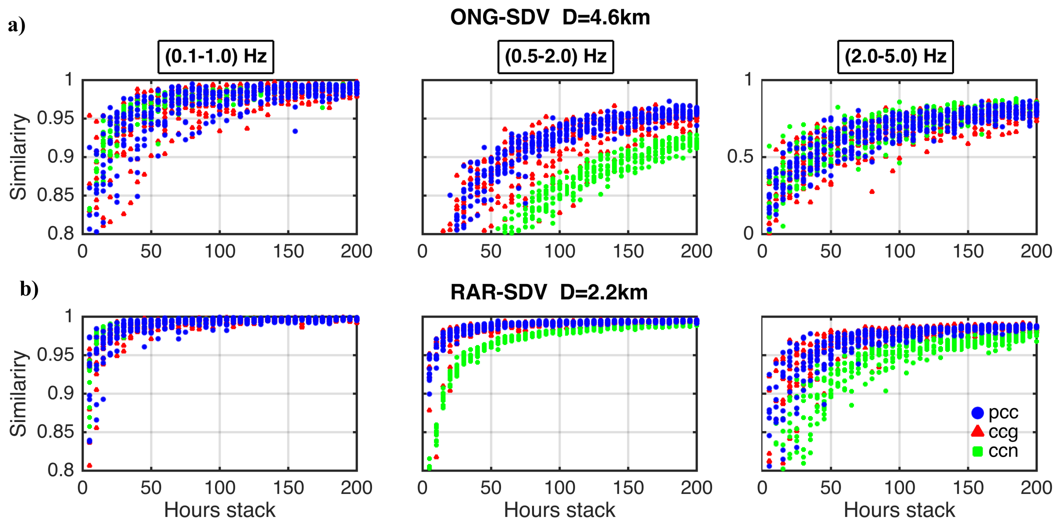

Figure 4.8: Waveform convergence at different frequency bands and inter-station distances - Waveform convergence of cross-correlation stacks as a function of the stack length in three different frequency bands (0.1-1.0 Hz, 0.5-2.0 Hz, 2.0-5.0 Hz) for a distant (top, 4.8 km) and closeby (bottom, 2.2 km) station couple. The similarity is computed as the PCC with respect to a reference trace, which is obtained stacking all traces excluding the days 210-300/2014. The colors distinguish the three correlation approaches employed, phase cross-correlation (blue), classical cross-correlation geometrically normalized without (red) and with pre-processing (green).

Focusing on the station couple RAR-SDV (Figure 4.8b), the higher the frequency, the slower the convergence for the three approaches as expected. However, the pre-processing applied to the classical cross-correlation yields a loss of waveform details that increases with frequency, and generally shows a slower convergence than the classical approach itself. The latter and the PCC have similar behaviour in the different frequency bands, although CCG seems to disperse more.

Focusing our attention now on the couple ONG-SDV (Figure 4.8a), we can see that the selected frequency band also has an important effect on the convergence. Please note the different vertical-axis scale in the highest frequency band. In general, all approaches here show slower convergence and bigger dispersion than the results for closer stations, however the PCC is slightly more robust. Therefore, we compute the

PCC of the vertical component of all seismic stations at (0.1 – 1) Hz. Then, we stack linearly the correlations using a 3-days sliding window, which we consider a proper stacking length for the chosen frequency band. Thus, we obtain daily virtual-source responses of the medium to seismic noise at the Reykjanes reservoir.

We select three seismic station pairs, implement the three methodologies and evaluate the time-lapse changes in their coda through the three methods described in Chapter 3. The obtained results are summarized in Figure 4.9. The first column corresponds to the results of the station pair RAR-RET that crosses the production area. In the second column, we show the results of the couple KRV–RAR that crosses the injection well RN–20B. In the last column, we represent the results of the phase auto-correlations belonging to YRN, which is the closest station to the tracer-test well RN-34. In Figure 4.9a, we highlight the injection rates corresponding to the closest well to the last two station couples (red and green lines) and the production rate in the first one (black line). In the three columns, all rates are depicted in grey for comparison. The obtained lag-time changes for every approach are listed and described below:

- Waveform similarity:

  This observable is computed in various lag-time windows of 6 seconds length (Figure 4.9b). The most prominent feature is the clear seasonal variation, which is maximum in January and minimum in mid-July, and appears between 4 and 16 seconds of lag time. Comparing it with the production rate variation (Figure 4.9a, black line), a similar low-frequency sinusoidal variation is present. The time evolution of this observable shows various fluctuations among which three of them concur with the largest variations in RGS's activity (Figure 4.9b, grey-shaded rectangles). These fluctuations can bee seen at 6, 8 and 14 seconds of lag time respectively for each station.

- Waveform stretching:

  The velocity variations, and their corresponding correlation coefficients, are computed at the same lag-time windows as the similarity, and averaged between 10 and 50 seconds (Figure 4.9c and 4.9d). The stretching technique is quite sensitive to the coherence between the reference and daily correlations. Due to the lack of calm period, the reference is a rough approximation of the seismic response of the medium, causing the low correlation coefficients observed. The results can be

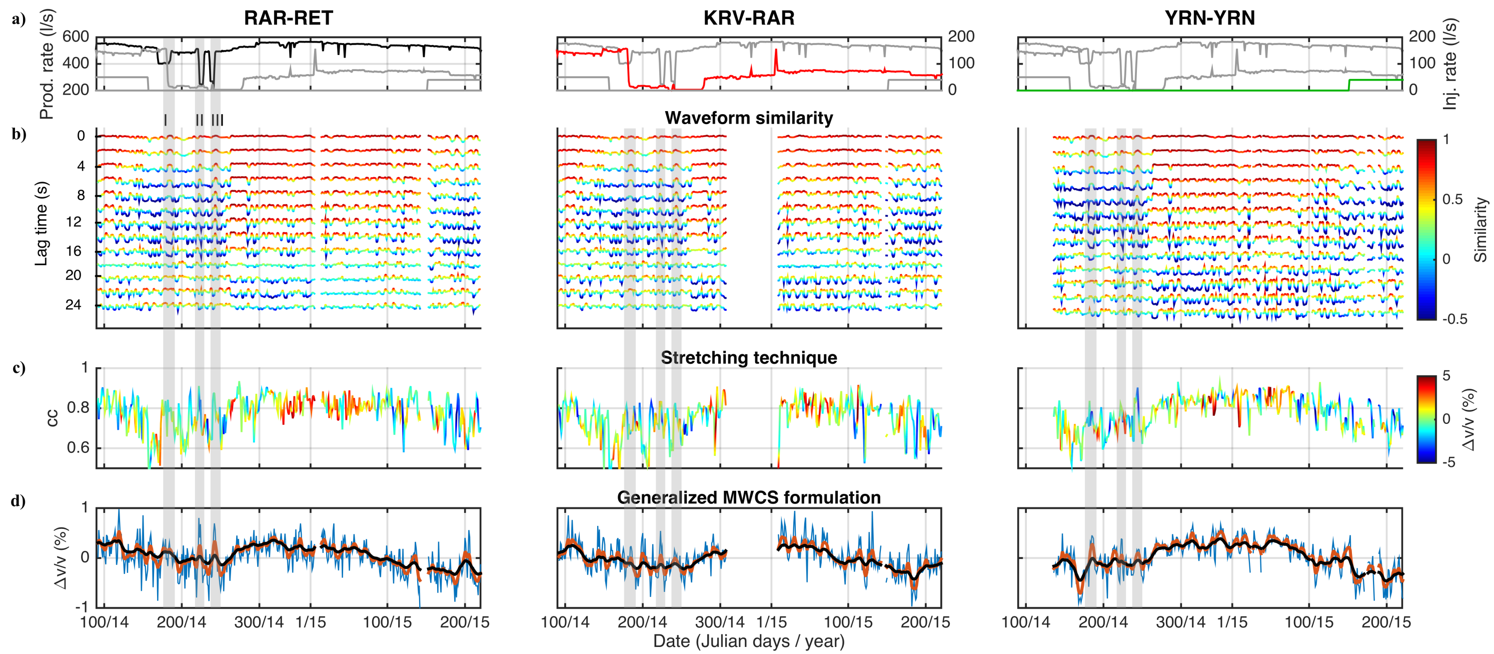

Figure 4.9: Lag-time changes at RGS - Results of the three different methodologies employed for the frequency band (0.1 -1) Hz for three station couples: RAR-RET (crossing the production area), KRV- RAR (crossing RN-20B well) and the autocorrelation of YRN (close to RN-34). (a) Production and injection rates of RGS are represented in grey highlighting the closest-well rate following the colors of Figure 2.7 and the production rate in black. (b) Averaged waveform similarity values for negative and positive lag-time windows of 6 seconds length. (c) Correlation coefficients obtained from the stretching technique, the color scale represents the computed velocity change. (d) Velocity changes computed by MWCS technique for three correlation lengths, $\beta = 5$ (blue), 10^3 (orange) and 10^4 (black). Grey shading indicates the three fluctuations of interest (I, II and III).

improved with larger time-shifts in the coda but the values become unrealistic and lack a physical sense. Nevertheless, the seasonal variation is clear for all station couples and the quick variations (I, II and III) can be observed as well although less clearly.

- Generalized MWCS formulation:

  It allows us to retrieve the velocity variations independently of any reference. Furthermore, the method provides short- and long- term variations controlled by the characteristic correlation length that we fix in 5, 10^3 and 10^4 following Brenguier et al. (2014). We use windows of 6 seconds between the direct surface wave arrivals and 50 seconds. The results obtained from this approach are depicted in Figure 4.9d. The low-frequency sinusoidal variation is clearly visible for the three station couples as it is with the previous methods.

  The velocity variations oscillate with similar amplitudes in the whole period, complicating the detection of significant short-term variations. Nonetheless, the production-rate related variations (II and III) protrude in the time series for the pair RAR-RET. The uncertainties of the velocity change estimates for β=5 are around 0.05% and the misfit around 0.1%. The trace of the resolution operators is 462. In this case, a perfectly resolve velocity variations time series would yield 475, which is the total number of days used in the inversion.

  Another observation is that the relative seismic velocity variations for $\beta = 10^4$ decrease linearly over time throughout the 1.5 years under study (Figure 4.9d, black line). This observation is slightly more pronounced in the station couple RAR–RET, which are located within the production area.

The time evolution of the previous observables contain numerous changes that hinder the clear identification of variations related to RGS. However, the three approaches show the rapid fluctuations (I, II and III) and a seasonal variation in their time series, increasing the reliability of the findings. Even so, the similarity analysis seems to be more robust. In order to distinguish the rapid variations clearer and with no need of employing several approaches, we decompose the similarity curves in the time-frequency domain through the S-transform. We first split the seismic network into two groups: Station couples within and outside the production area. Then, we average the similarity curves for each group and compute the S-transform for the 1.5 years of study (Figure 4.10c). The standard deviation corresponding to the similarity average is represented as grey shading (Figure 4.10b).

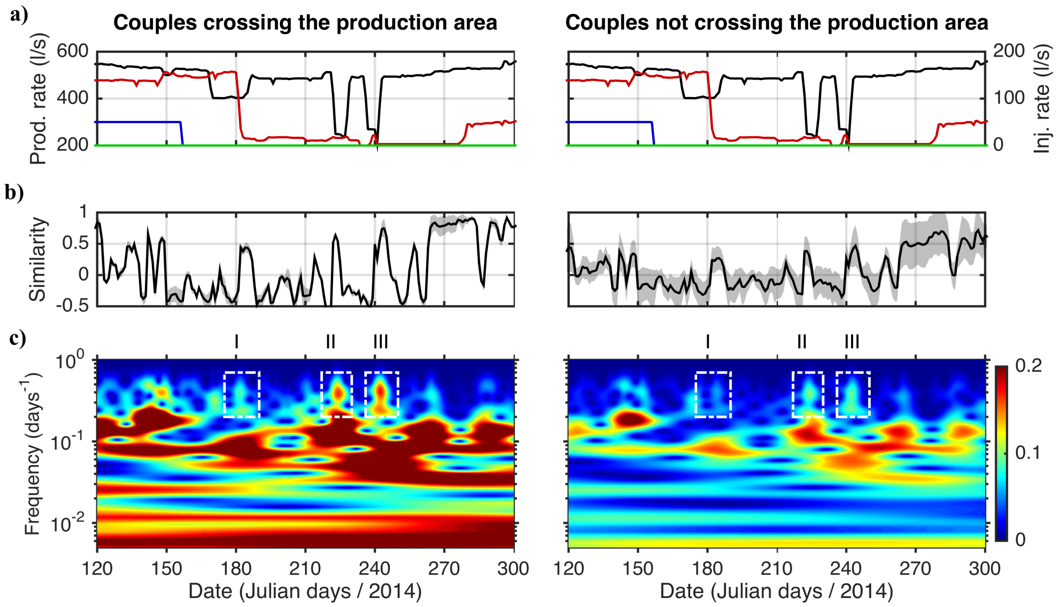

Figure 4.10: S-transform of waveform similarity time series at RGS - (a) Production and injection rate of RGS. The colors are the same as on Figure 2a. (b) Average of similarity values of station couples that cross (left) and do not cross (right) the production area at 6 seconds lag time. Standard deviation is shown as gray shading. (c) Time-frequency amplitude spectra of the above similarity curves. The white boxes highlight the fluctuations I, II and III.

The highest frequency retrieved in this analysis is limited by the Nyquist frequency; in this case 0.5 days^{-1}. The resolution at low frequencies is expected to be poor since the seismic records are only 1.5 years long. In between, we observe the three short-term similarity variations (Figure 4.10b, I-III) clearly in the S-transform from 0.2 Hz up to the Nyquist frequency (Figure 4.10c). Such variations are more prominent for the station couples that cross the production area and the estimates show less variability. In a similar way, the seasonal variation that appears below $6{\cdot}10^{-3}$ days^{-1} is present in both station groups but it is more intense within the production area.

The largest structural changes are located closer to the power plant, as expected. For verification purposes and further details, we compute and map the scattering cross-section distribution associated with the three analysed fluctuations (Figure 4.11, a-c) as well as the seasonal variation (Figure 4.11e). For comparison, we also compute such distribution during 10 days without abrupt variations in the RGS activity (Figure 4.11d).

In the construction of sensitivity kernels, we use an approximation of the scattering mean free path of 30 km, inferred from attenuation studies in Reykjanes (Menke et al., 1995), and the effective wave speed is fixed at 3km/s. As we saw in El Hierro study, the horizontal location of the changes hardly depends on those two input parameters and a rough approximation should be sufficient. The decorrelation is quantified as the similarity amplitude of the peaks of interest since they occur at a the minimum of the seasonal variation. On the other hand, the seasonal change is estimated as the difference between the averaged similarity in winter and summer.

Indeed, all structural changes, including the seasonal, are located around the production area. Consistently, the larger the similarity variation, the larger the scattering cross-section (please note the different color scales). The maximum scattering cross-section is $4 \cdot 10^{-4}$ km/km^2 and is caused by the seasonal change at the left edge of the production region.

4.2.2 Interpretation

Geothermal energy is the largest source of energy worldwide and has been increasingly exploited since 1911, when the first geothermal plant generated successfully electricity in Larderello, Italy. Improving the permeability of rocks and injecting pressurized fluids into the system enable the heat mining for a much larger portion of the Earth's crust; this is the fundamental idea of EGS. To our knowledge, SI has only been employed to probe and monitor this type of geothermal systems (Hillers et al., 2015, Lehujeur et al., 2015; Obermann et al., 2015). Hence, studying RGS using seismic noise has provided an attractive opportunity to asses the capability of SI to monitor hydrothermal systems.

In this scenario, we discern short- and long- term variations in the scattering properties of the subsurface. We use the same similarity analysis as we did in El Hierro island and the PCC as well, in addition to the stretching technique and the generalized MWCS formulation. In this case, there is not a coherent noise source in the time period under study, what let us work in a wide range of frequency bands. Since the

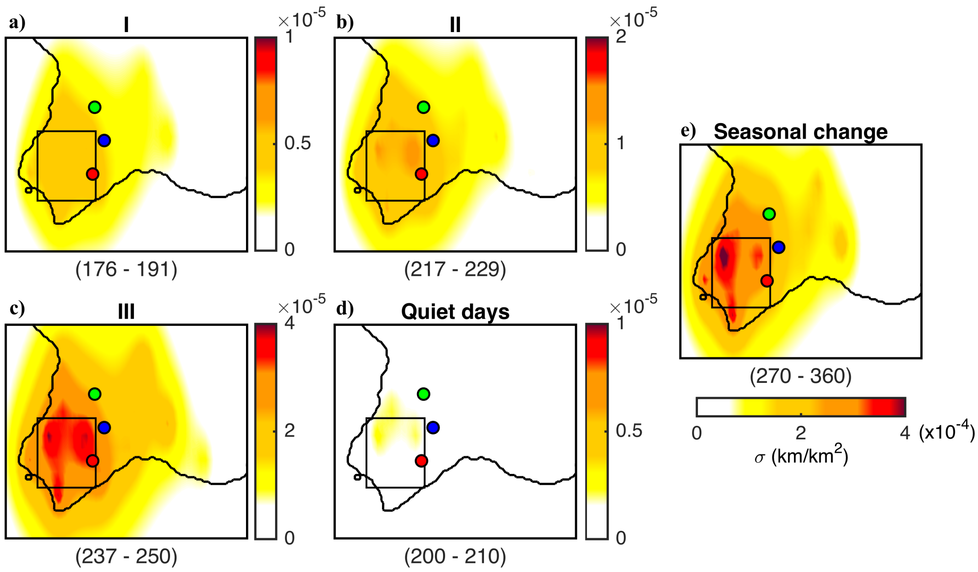

Figure 4.11: Scattering cross-section density maps related to RGS activity - Scattering cross-section density maps at 6 seconds of lag time for (a, b, c) the three highlighted periods in Figure 4.10 (I, II, III), (d) an example of calmest days and (e) the seasonal change.

activity of RGS changes abruptly within hours (Figure 4.9a), we need an even higher accuracy in our measurements than in El Hierro case. As we showed in Figure 4.8, the waveform convergence becomes slow for high frequencies and distant stations. High-frequency waves interact with more medium perturbations and suffer lager waveform distortions. Hence, longer stacking lengths are needed in order to achieve a stable response. Consequent, wlye work in the band $(0.1 - 1)$ Hz.

Combining the results of the three approaches (Figure 4.9) and the time-frequency decomposition of similarity (Figure 4.10), two rapid alterations in the subsurface were observed as relative velocity variations and waveform similarity changes (II and III). The abrupt production rate drops in the power plant change the state of stress abruptly and distort the wave propagation. Furthermore, the largest injection rate variation (I) is observed as well in both estimates.

The production and injection effects on the seismic response are observed in different lag-time windows. The similarity change I, which is related to the largest injection-rate drop of RN-20B, appears at earlier lag times than the others. The associated structural changes may be therefore shallower than those caused by production-rate drops, which affect likely a deeper and wider zone of the surrounding medium. The probed depth ranges between 0.5 and 12 km, since the seismic velocity of surface waves is roughly 1.2 km/s in the Reykjanes peninsula for frequencies of (0.1 1)Hz (Jousset et al, 2016). The water injection into the rock mass takes places at approximately 1.2 km. The changes are therefore expected to be constrained to the first few kilometres of the crust.

The rapid medium seismic responses (I, II and III) seem ambiguous when observed in the time series of Figure 4.9b, which contains numerous fluctuations with similar amplitudes. Hereby, the decomposition in the time-frequency domain through the S-transform allows identifying variations that *a priori* seem confusing. The S-transform has been used in other studies as a filter for *denoising* seismic noise, increasing the signal-to-noise ratio (Hadziioannou et al., 2011; Schimmel & Gallart, 2007; Schimmel & Paulssen, 1997). For first time, here the S-transform is employed as a final step in SI in order to elucidate meaningful variations in time series. This procedure has been tested for waveform similarity values and can be extended to seismic velocity changes as well.

Since the heat-mining started some decades ago, the rock matrix of the peninsula should be highly altered and likely unstable. Thus, a structural change in a particular point can trigger variations in the surrounding medium. This would explain the large-scale effects caused by the local variations (Figure 4.11). On the other hand, the values are smaller than those of other studies where volcanic eruption volumes (Obermann, Planès, Larose, Sens-Schönfelder, et al., 2013; Sánchez-Pastor et al., 2018), or 10^5 liters of injection were studied (Hillers et al. 2015).

Focusing now our attention on long-term observations, highlight that the seasonal variation is observed clearly through the three approaches (Figure 4.9). There are two possible sources that yield such variation: The seasonality of seismic noise sources and the energy production in the power plant, which shows a seasonality as well. For comparison, the Figure 4.12 shows the temperature measured in a meteorological station placed in Reykjavik (`https://www.vedur.is/`) together with the production rate of RGS (Figure 4.12a) and the velocity variation time series retrieved for RAR-RET (Figure 4.12b).

The production rate varies depending on the power plant demand of the Icelandic population, which is clearly maximum in winter and minimum in summer (Figure 4.12a). This can produce seasonal structural changes in the reservoir. On the other

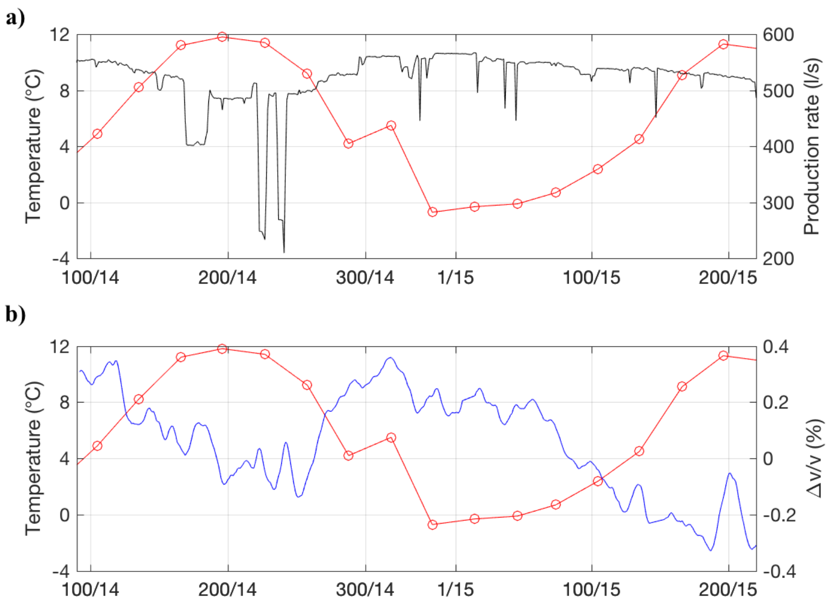

Figure 4.12: Seasonal variations in Reykjanes - Comparison between the mean temperature in Reykjavik (red) and (a) the production rate (black line) and (b) the relative velocity variations from RAR-RET (blue line).

hand, seasonal variations of the ocean noise directivity affect the ballistic waves of the cross-correlations (e.g. Froment et al., 2010; Hadziioannou et al., 2011) and furthermore, crustal seasonal changes are often identified in long time series of velocity variations (e.g. Sens–Sönfelder & Wegler 2006; Meier et al. 2010; Ugalde et al. 2014). Hence, the seasonal variations observed in the similarity values and seismic velocity variations (Figure 4.9b-d; 4.12b) may be a product of both effects overlapped.

The study area is very small and the effects of the seasonal variations are expected to be mostly homogeneous in the peninsula. Nevertheless, we observe a more intense seasonal variation near the power plant (Figure 4.9b; 4.10c). In addiction, the seasonal pattern is restricted to a specific lag-time window and the first arrivals barely show this variation. Besides, looking at day 264 (2014), the similarity values suffer a sign-switch too abrupt to come from a noise-source distribution change and do not coincide with any production rate drop at that time (Figure 4.10). We are however inclined to believe that the production rate variations directly influence the subsurface.

A possible interpretation for the abrupt increases in the similarity values is that the medium exhibits a production rate threshold, estimated at about 520 l/s. Once the energy production exceeds this tolerance threshold, the medium properties change drastically. The permeability could be responsible of such changes since it depends exponentially on the exposition time to hot water flows (Summers et al., 1978). Aside from that, the permeability of porous rocks shows a significant change at a critical pressure, mainly due to pore collapses (David et al., 1994).

Another long-term effect of the RGS in the surrounding medium may be the negative trend in the relative seismic velocities that was pointed out in Section 4.2.1. In order to analyse the robustness of this negative trend result, we compute the velocity variations using the generalized MWCS formulation for all stations couples. Then, we fit the time series to linear regressions and split the stations into two groups, within and outside the production area (Figure 4.13).

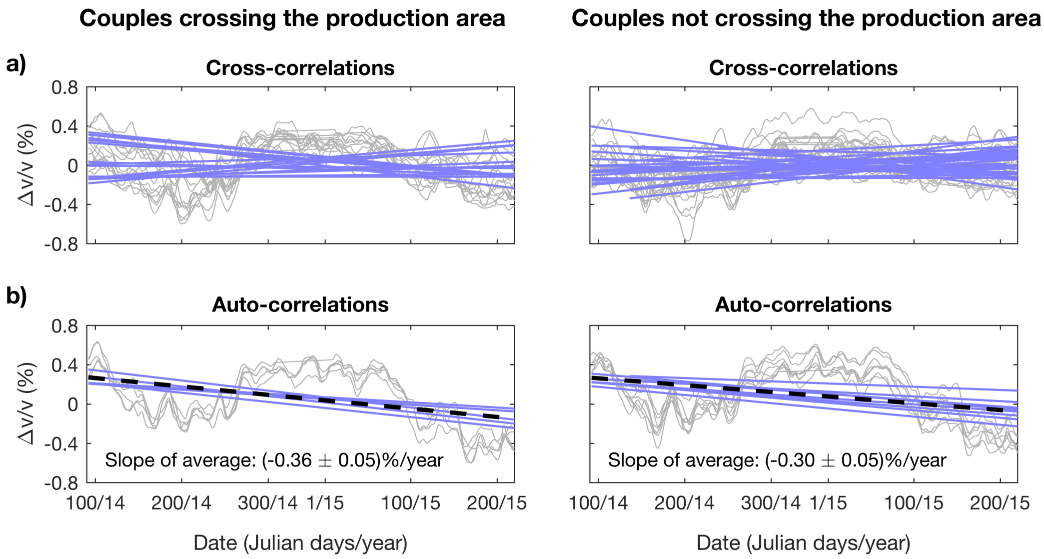

Figure 4.13: Seismic velocity decrease at the Reikjanes reservoir - Velocity variations measured using the generalized MWCS formulation for $\beta = 10^4$ (grey lines) of cross- (a) and auto-correlations (b) for the 1.5 years of study. The blue lines represent their linear regressions of every curve and the dashed-black line the linear regression of the velocity variation average of the station group.

As we can see, all auto-correlations show a negative trend whereas cross-correlations show positive and negative slopes. This discrepancy is currently under debate and require an in-depth analysis of how affect the different dominant type of waves in the depth sensitivity of auto- and cross-correlations. On the other hand, this different behaviour can be related to the computation itself of the velocity variations. We have applied the MWCS technique only in the causal part of the virtual-source responses following Brenguier et al. (2014). Since this method requires highly coherent and stable correlations, using the symmetric responses may decrease the variability of the cross-correlation results.

We also compute the linear regressions of the averaged velocity curves into both groups (Figure 4.13b, dashed black line). The slopes of the lines indicate th eregional velocity decrease. We estimate them in $-0.36 \pm 0.05\%$/year within the production area and outside, a slightly lower value of $0.30 \pm 0.05\%$/year.

The extraction of water during several decades from the Reykjanes reservoir carries short- and long- repercussions in the area. Despite the re-injection of waste fluids into the system, the pressure drop is not counteracted due to the loss of steam to air, resulting in a contraction of the rock matrix and a consequent man-made subsidence of the area (Keiding et al., 2010). Thus, the by-product density increase of the rock matrix may cause the seismic velocity decrease. Furthermore, the water deficit can play a further role in the observed seismic velocity, which decreases in high-porosity pyroclastic rocks as a function of water content (e.g Kahraman et al., 2017).

As a final observation, the system seems to respond differently to short and long timescales. We observed seismic velocity increases for rapid decreases in water extraction (Figure 4.9d) and the contrary, the seismic velocity decreases over a timescale of years due to the water deficit (Figure 4.13b). However, here we have not further analysed the physical processes which cause this different behaviour.

5
Discussion

As the obtained results for both research lines have already been interpreted and discussed, I will now focus in this chapter on the methodology, which is the common denominator for them. I will then remark the limitations, advantages and downsides of the techniques used for monitoring temporal changes in the elastic properties of subsurface media.

Firstly, reliable and accurate Green's functions are retrieved under the assumption that either the noise source distribution is symmetric or the propagation medium is highly heterogeneous. Besides this, the sources should barely change over time. Otherwise, a change in the seismic response of the medium may be wrongly interpreted as a scattering property variation. In other words, the medium perturbations should be illuminated symmetrically and constantly by noise sources. However, different studies (e.g. Hadziioannou et al., 2009; Obermann et al., 2013b; 2014; 2015) have shown that these requirements can be relaxed for monitoring purposes.

Therefore, the frequency band plays an important role in this type of studies and could very well be a limitation. It defines the perturbation size with which the recorded seismic waves interact as well as the probed depth. Furthermore, waveform convergence improves significantly when filtering the seismic data (Roux et al., 2005) and therefore the temporal accuracy is determined by the frequency band as we have shown in Figure 4.8. In the case of El Hierro eruption, the volcanic tremor was a nuisance that does not allow us to draw conclusions during the eruptive period. This tremor acted as a variable and coherent noise source that overlapped the oceanic noise sources in a wide range of frequencies.

Another aspect that is worths commenting, is the possible influence of the local seismicity in correlations. Studies as D'Hour et al. (2016) and Schimmel et al. (2011; 2018) show the effects of large amplitudes in SI studies when using the correlation classical approach without (CCG) and with (CCN) one-bit normalization and spectral whitening. On the contrary, correlograms obtained from PCC remain unaltered in presence of seismic events in the study area. The results of this thesis corroborate this idea. For instance, in Figure 4.4 it can be seen that the seismicity and high values of cross-sections do not match, neither in time nor in space. Since the PCC does not require pre-processing techniques in order to mitigate the amplitude bias of correlations, the temporal accuracy generally is higher than the one achieved through CCN.

Once correlations are computed, we use several techniques for quantifying temporal changes, including waveform similarity, stretching and MWCS (or doublet method). The last two techniques are widely used in monitoring studies to estimate seismic velocity variations in the subsurface (e.g. De Plaen et al., 2016; Duputel et al., 2009; Mordret et al., 2016; Snieder et al., 2002). All of them require a reference function to compare the medium responses at different times and detect perturbations. However, Brenguier et al. (2014) proposed a general formulation of the doublet method in which the variations are computed with respect to all possible combination of days removing thus the reference bias.

On the other hand, the analysis of the time evolution of waveform similarity is a recent approach that allows inferring changes in the seismic response of media, and that we have applied successfully in both scenarios. D'Hour et al. (2016) were the first applying this approach to study the post-seismic effects of a small earthquake swarm in Brazil. The advantage of this technique against the doublet method and its derived methodologies is that assumptions and approximations of the spatial distribution of the changes are not needed. As we have seen in Section 3.2, the velocity variations are estimated through measures of time-shift variations considering they are homogeneously distributed in the medium.

Furthermore, in the waveform similarity analysis there is no restriction regarding the coherence between the reference and current traces. On the contrary, with the other techniques the velocity variations are considered reliable when the coefficient correlation is higher than a given threshold, typically above 0.8. Depending on data quality, this need requires stacking longer periods of time with the consequent loss of temporal resolution. Nevertheless, since a reference trace is needed and the results depend on it (Figure 4.2), we recommend interpreting the relative changes of the observables instead of their absolute values. We also encourage to perform some preliminary tests in order to select a good and reliable reference trace for all techniques that rely on a reference.

The similarity simply quantifies how much similar or different two traces are. The drawback of this approach is that mechanical and structural changes might cause variations in the similarity values and they cannot be distinguished. The correlation coefficient computed through the stretching technique is typically used as a independent measure of structural changes whereas variations in velocity estimates quantify mechanical changes (e.g. Hadziioannou et al., 2009; Obermann et al., 2013b; 2015).

The methodologies currently used for cross-correlations can also be applied to auto-correlations (D'Hour et al., 2016; De Plaen et al., 2016; Nakahara, 2014; Sens–Sönfelder & Wegler, 2006; Wegler & Sens–Schönfelder, 2007). As we have seen in Figure 4.1c, auto-correlations offer higher accuracy detecting tiny changes than cross-correlations. Their sensitivity is limited however to the crust beneath the corresponding seismic station (Figure 3.4) and provides a very local view of the medium. For this reason, we use auto-correlations as a constraint in the inversion procedure for the scattering cross-section computation (equation 3.18).

The two cases discussed in this thesis highlight the importance of the lag-time window choice. Most of the above-mentioned studies compute the velocity variation time series in the expected lag-time window to observe alterations or in a few long windows. Depending on the frequency band and scattering properties of media, correlograms can become very complex and show lag-time changes in narrow specific windows. We therefore perform the methods in sliding windows that go across the entire coda. Consequently, a more complete view is obtained, facilitating the change identification.

In the case of time series composed by a superposition of signals with different frequencies and high variability, the S transform is an useful tool to decompose the signal and it enables the detection of temporal changes. Typically, this transform is used to increase the SNR of noise correlations (e.g. Hadziioannou et al., 2011; Schimmel & Gallart, 2007). In this thesis, we employed the S transform in study of the Reykjanes reservoir in the waveform similarity estimates in order to identify variations with different frequencies (Figure 4.10c). This allowed us to relate short- and long-term variations to the RGS activity. Note that this approach can be applied in velocity variations time-series as well.

Another useful tool proposed in this manuscript is the so called change point analysis, which provides the points of a function where a statistic, such as the mean, changes significantly. In the case of El Hierro eruption, we applied this analysis to the pre-eruptive period in order to discriminate periods of time in which the elastic properties of the medium remain invariant. Thus, we could identify the pre-eruptive volcanic phases inferred by López et al. (2012) automatically and using only seismic ambient noise. It is worth commenting that monitoring studies usually identify changes without showing their significance against other fluctuations in the time series. The change point analysis can be applied as well to velocity variations time series. Furthermore, the low computation cost makes it a potential tool for this type of studies.

Besides identifying scattering changes in time, their locations are especially important in monitoring as well. Tomography studies reveal structures in the subsurface, whereas the scattering cross-sections quantify temporal changes in structures. The main input parameters for computing this observable are the transport mean free path and an approximation of the wave speed. An important observation is also that the horizontal distribution of the changes hardly depends on this parameters and only controls the size of the probed area (Figure 4.5), which agrees with Obermann et al. (2013b). Thus, monitoring temporal changes in the subsurface through CWI can be employed in poorly studied regions with scarcely geological information.

Finally, remark that the sensitivity kernels used in the computation of the scattering cross-sections are described assuming acoustic media, diffusive energy transport, isotropic scattering processes and surface waves, as the dominant type in the coda. Building more realistic kernels becomes tough as there is no analytical solutions even for the case of elastic media. Sensitivity kernels that combine surface and body waves are recently achieved in order to constraint the depth of temporal changes (e.g. Kanu and Snieder, 2015; Obermann et al., 2016; 2018). The propagation of bulk waves is modeled as well through the (3-D) radiative transfer equation (Obermann et al., 2013a; 2016; 2018) and therefore the solution depends on the same parameters for both types of waves. Consequently, we do not expect significant variations in the 2-D scattering cross-section maps when using combined kernels. However, in future studies those kernels will be used for 3D location of scattering properties variations.

6 Conclusions

The present thesis has been focused on evaluating the capability of seismic interferometry to monitor subsurface elastic properties in two challenging scenarios: The 2011-2012 El Hierro eruption and the Reykjanes Geothermal System. In the first case, the seismic station network was far from optimal in order to monitor the Tagoro volcano through seismic noise correlations. The unexpected eruption occurred undersea and this impeded setting up instruments around the volcanic edifice and well in advance. In the Reykjanes reservoir case the seismic network had a good distribution. However, the identification of time-lag changes was also difficult since the energy production and various injection wells were operating the entire period of study. As a result, there was not a *quiet* period with which to compare the daily responses. In the following, I review the most relevant outcomes of both research lines.

Regarding methodologies, the PCC has been employed for first time in volcanic and geothermal environments and has allowed us to calculate detailed daily seismic responses of the media beneath El Hierro island and the Reikjanes reservoir. We expected rapid variations in the medium due to the high dynamics of both systems. Here, the PCC gains importance due to its most remarkable advantage: It provides coherence measures between two signals regardless of their amplitude. Thus, the effects in the correlations caused by instruments issues, earthquakes and other large-amplitude sources, are mitigated without the need to apply other techniques. Accordingly, the medium seismic responses converge fast to a stable state, increasing therefore the temporal accuracy to detect changes.

The thesis shows that auto-correlations are a good approach to accurately infer local changes, as the recorded seismic wavefield remains confined beneath the seismic stations. All the techniques applicable to cross-correlations for quantifying temporal changes as stretching and waveform similarity, can be applied to auto-correlations as well. This opens the possibility to monitor systems equipped with one or just a few instruments. Moreover, auto-correlations have been used as constraints in the inversion procedure of the scattering cross-sections to determine the spatial distribution of the changes.

Another valuable contribution is the improvement of the waveform similarity analysis by computing the similarity in a sliding lag-time window that goes across the entire coda. Opposite to the stretching and MWCS techniques, where the coherence between the reference and daily responses is required quite high, the similarity analysis does not impose any restriction or assumption for being applied and those responses can be significantly different. The downside of the waveform similarity is the lack of information about the change origin, i.e., mechanical and structural changes cause equal variations in the similarity and they cannot be distinguished. In contrast to the MWCS that does not depend on a reference function, for similarity and stretching methods we encourage performing some preliminary tests in order to select a good and reliable reference trace.

Furthermore, two new procedures have been proposed to improve the monitoring of temporal medium changes: Time-frequency decomposition of time series through the S-transform and the change point analysis. The latter allows differentiating periods of time among which a statistic varies significantly. Its best asset is the possibility to detect automatically relevant changes in time series of waveform similarity or velocity variations; this is essential for forecasting and monitoring purposes. On the other hand, the S transform provides a powerful tool to discriminate fluctuations in very complex time series, where the change point analysis becomes fruitless in the time domain.

The careful and meticulous data processing performed has provided relevant results in both study areas. In the case of El Hierro eruption, we have clearly pinpointed the beginning and end of the submarine eruption to exact dates (10 October 2011 to 15 February 2012); the end of the eruption remained vague in previous geophysical studies. Furthermore, we identified the different pre-eruptive phases thanks to the change point analysis of the similarity time series. Besides this, throughout 2012 we detected and located subsurface changes related to three magmatic intrusions prior to their surface manifestation. It is also worth mentioning that analysing only the time evolution of the similarity values of one single auto-correlation, we observe most of the above-commented results.

In the Reykjanes reservoir study, the time evolution pattern of similarity and velocity changes has a rich frequency content that points to different time scale effects in the subsurface. The lack of seismic records during a calm period causes a strong variability of noise response reference of the medium. However, thanks to the S transform we discriminate three fluctuations associated to injection and production rate drops. In the long term, the power plant subsurface shows a seasonal variation that might be associated with the energy demand. Furthermore, the increasing water deficit of this geothermal system produces a slow velocity decrease of 0.36%/year in the surrounding medium.

References

Akaike, H. (1974), A New Look at the Statistical Model Identification, *IEEE Transactions on Automatic Control*, 19, 716723.

Aki, K. (1957), Space and time spectra of stationary stochastic waves, with special reference to microtremors, *Bull. Earthq. Res. Inst.*, 35, 415456.

Ardhuin, F., L. Gualtieri, and E. Stutzmann (2015), How ocean waves rock the earth: Two mechanisms explain microseisms with periods 3 to 300 s, *Geophys. Res. Lett.*, 42(3), 765772, doi:10.1002/2014GL062782.

Auger, I. E., & Lawrence, C. E. (1989). Algorithms for the Optimal Identification of Segment Neighborhoods. *Bulletin of Mathematical Biology*, 51, 39-54.

Backus, M., Burg, J., Baldwin, D., and Bryan, E. (1964). Wide band extraction of mantle p waves from ambient noise. *Geophysics*, 29:672692.

Bakulin, A., & Calvert, R. (2004). Virtual source: New method for imaging and 4D below complex overburden: 74th Annual International Meeting, SEG, Expanded Abstracts, 24772480.

Bakulin, A., & Calvert, R. (2006). The virtual source method: Theory and case study. *Geophysics*, 71, 4, SI139SI150.

Bensen, G. D., M. H. Ritzwoller, M. P. Barmin, A. L. Levshin, F. Lin, M. P. Moschetti, N. M. Shapiro, & Y. Yang (2007), Processing seismic ambient noise data to obtain reliable broad-band surface wave dispersion measurements, *Geophysical Journal International*, 169, 12391260.

Beroza, G. C., Cole, A. T., & Ellsworth, W. L. (1995). Stability of coda wave attenuation during the Loma Prieta, California, earthquake sequence. *Journal of Geophysical Research: Solid Earth*, 100(B3), 3977-3987.

Bertelli, T. (1872). Osservazoni sui piccoli movimenti dei pendoli in relazione ad alucuni fenomeni meteorologiche, *Bullettino Meteorologico dell'Osservatorio del Collegio Romano*, XI, 11

Blanco, M. J., Fraile-Nuez, E., Felpeto, A., Santana-Casiano, J. M., Abella, R., Fernández-Salas, L. M., et al. (2015). Comment on Evidence from acoustic imaging for submarine volcanic activity in 2012 off the west coast of El Hierro (Canary Islands, Spain) by Pérez, N. M., Somoza, L., Hernández, P. A., González de Vallejo, L., León, R., Sagiya, T., et al. [Bulletin of Volcanology (2014) 76: 882-896]. *Bulletin of Volcanology*, 77(7), 62. https://doi.org/10.1007/s00445-015-0947-6

Brenguier, F., Campillo, M., Takeda, T., Aoki, Y., Shapiro, N. M., Briand, X., Emoto, K. & Miyake, H. (2014). Mapping pressurized volcanic fluids from induced crustal seismic velocity drops, *Science*, 345, 8082.

Carracedo, J. C. (1994). The Canary IslandsAn example of structural control on the growth of large oceanic-island volcanoes. *Journal of Volcanology and Geothermal Research*, 60(3-4), 225241. https://doi.org/10.1016/0377-0273(94)90053-1

Carracedo, J. C., PerezTorrado, F. J., RodriguezGonzalez, A., FernandezTuriel, J. L., Klügel, A., Troll, V. R., & Wiesmaier, S. (2012). The ongoing volcanic eruption of El Hierro, Canary Islands. *Eos, Transactions American Geophysical Union*, 93(9), 89-90.

D'Hour, V., Schimmel, M., Do Nascimento, A. F., Ferreira, J. M., & Lima Neto, H. C. (2016). Detection of subtle hydromechanical medium changes caused by a small-magnitude earthquake swarm in NE Brazil. *Pure and Applied Geophysics*, 173(4), 10971113. https://doi.org/ 10.1007/s00024-015-1156-0

De Plaen, R. S. M., T. Lecocq, C. Caudron, V. Ferrazzini, & O. Francis (2016), Single-station monitoring of volcanoes using seismic ambient noise, *Geophysical Research Letters*, 43, doi:10.1002/ 2016GL070078.

Derode, A., Larose, E., Tanter, M., de Rosny, J., Tourin, A., Campillo, M., and Fink, M. (2003b). Recovering the Greens function from field-field correlations in an open scattering medium (L). *Journal of the Acoustical Society of America*, 113 :2973. 10, 11, 12, 114

Díaz-Moreno, A., Ibáñez, J. M., De Angelis, S., García-Yeguas, A., Prudencio, J., Morales, J., et al. (2015). Seismic hydraulic fracture migration originated by successive deep magma pulses: The 2011-2013 seismic series associated to the volcanic activity of El Hierro Island. *Journal of Geophysical Research: Solid Earth*, 120, 77497770. https://doi.org/10.1002/2015JB012249

Dewey, J., & Byerly, P. (1969). The early history of seismometry (to 1900). *Bulletin of the Seismological Society of America*, 59(1), 183-227.

Duputel, Z., Ferrazzini, V., Brenguier, F., Shapiro, N., Campillo, M., & Nercessian, A. (2009). Real time monitoring of relative velocity changes using ambient seismic noise at the Piton de la Fournaise volcano (La Réunion) from January 2006 to June 2007. *Journal of Volcanology and Geothermal Research*, 184, 164173.

Duvall, T. L., Jefferies, S. M., Harvey, J. W. and Pomerantz, M. A. (1993). Time-distance helioseismology. Nature, 362(6419), 430432. Fichtner, A. (2014), Source and processing effects on noise correlations, *Geophysical Journal International*, 197, 15271531.

Ermert, L. (2017). Ambient seismic noise inversion. PhD manuscript, ETH Zürich

Fink, M. (1992). Time reversal of ultrasonic fields Part I: Basic principles. *IEEE Transactions on Ultrasonics, Ferroelectrics and Frequency Control*, 39(5), 555566. 12

Fink, M., Prada, C., Wu, F. & Cassereau, D. (1989). Self focusing with time reversal mirror in inhomogeneous media. *IEEE Ultrasonics Symposium*, Montreal, PQ, Canada, 2, 681-686

Forbes, J. D. (1844). XIII. On the Theory and Construction of a Seismometer, or Instrument for Measuring Earthquake Shocks, and other Concussions. *Earth and Environmental Science Transactions of The Royal Society of Edinburgh*, 15(1), 219-228.

Frechet, J., Martel, L., Nikolla, L., and Poupinet, G. (1989). Application of the Cross-Spectral Moving-Window Technique (CSMWT) to the Seismic Monitoring of Forced Fluid Migration in a Rock Mass. *International Journal of Rock Mechanics and Mining Sciences*, 26(3- 4), 221233. 44, 80

Fricke, J. T., Evers, L. G., Smets, P. S. M., Wapenaar, K. and Simons, D. G. (2014). Infrasonic interferometry applied to microbaroms observed at the Large Aperture

Infrasound Array in the Netherlands. *Journal of Geophysical Research: Atmospheres*, 119(16), 96549665.

García, A., Fernandez-Ros, A., Berrocoso, M., Marrero, J. M., Prates, G., De la Cruz-Reyna, S., & et al. (2014). Magma displacements under insular volcanic fields, applications to eruption forecasting: El Hierro, Canary Islands, 20112013. *Geophysical Journal International*, 197(1), 322334. https://doi.org/10.1093/gji/ggt505

Gaudot, I., Beucler, ., Mocquet, A., Schimmel, M., & Le Feuvre, M. (2015). Statistical redundancy of instantaneous phases: theory and application to the seismic ambient wavefield. *Geophysical Journal International*, 204(2), 1159-1163.

Gerstoft, P., Fehler, M.C.., and Sabra, K.G.. (2006). When Katrina hit California. *Geophysical Research Letters*, 33(L1730).

Gerstoft, P., Shearer, P.M.., Harmon, N., and Zhang, J. (2008). Global P, PP, and PKP wave microseisms observed from distant storms. *Geophysical Research Letters*, 35(L23306).

Gibson, P., Lamoureux, M. & Margrave, G. (2006). Stockwell and Wavelet Transforms. *The Journal of Fourier Analysis and Applications*, 12, 6, 713-721, doi:10.1007/s00041-006-6087-9

González, P. J., Samsonov, S. V., Pepe, S., Tiampo, K. F., Tizzani, P., Casu, F., et al. (2013). Magma storage and migration associated with the 20112012 El Hierro eruption: Implications for crustal magmatic systems at oceanic island volcanoes. *Journal of Geophysical Research: Solid Earth*, 118, 43614377. https://doi.org/10.1002/jgrb.50289

Gutenberg, B. (1936). On microseisms. *Bulletin of the Seismological Society of America*, 26(2).

Hadziioannou, C., Larose, E., Coutant, O., Roux, P., and Campillo, M. (2009). Stability of monitoring weak changes in multiply scattering media with ambient noise correlation: Laboratory experiments. *Journal of the Acoustical Society of America*, 125(6):36883695.

Haney, M. M. (2009). Infrasonic ambient noise interferometry from correlations of microbaroms. *Geophysical Research Letters*, 36(19), L19808.

Hasselmann, K. (1963), A statistical analysis of the generation of microseisms, *Reviews of Geophysics*, 1, 177209.

Hennino, R., Tregoures, N., Shapiro, N. M., Margerin, L., Cam- pillo, M., van Tiggelen, B. A., et al. (2001). Observation of equipartition of seismic waves. *Physical Review Letters*, 86(15), 34473450.

Hennino, R., Tregoures, N., Shapiro, N.M.., Margerin, L., Campillo, M., van Tiggelen, B.A.., & Weaver, R.L.. (2001). Observation of equipartition of seismic waves. *Physical Review Letters*, 86(15):34473450.

Herraiz, M. and Espinoza, A.F.. (1997). Coda waves: A review. *Pure and Applied Geophysics*, 125(4):499577.

Hillers, G., Husen, S., Obermann, A., Plan s, T., Larose, E. and Campillo, M. (2015). Noise-based monitoring and imaging of aseismic transient deformation induced by the 2006 Basel reservoir stimulation. *Geophysics*, 80(4), KS51KS68.

Hobiger, M., U. Wegler, K. Shiomi, and H. Nakahara (2014), Single-station cross-correlation analysis of ambient seismic noise: Application to stations in the surroundings of the 2008 Iwate-Miyagi Nairiku earthquake, *Geophysical Journal International*, 198(1), 90109, doi:10.1093/gji/ggu115.

IGME (2008). Plan GEODE de cartografía geolgica continua. Instituto Geológico y Minero de España. Cartografía digital. Available online at: `http://cuarzo.igme.es/sigeco/`

Iyer, H.M.. and Healy, J.H.. (1972). Evidence for the existence of locally generated body waves in the short!period noise at the large aperture seismic array. *Bulletin of the Seismological Society of America*, 62:1329.

Jackson, B., Sargle, J. D., Barnes, D., Arabhi, S., Alt, A., Gioumousis, P., Tsai, T. (2005). An Algorithm for Optimal Partitioning of Data on an Interval. *IEEE Signal Processing Letters*, 12, 105-108.

Kanu, C., & Snieder, R. (2015). Numerical computation of the sensitivity kernel for monitoring weak changes with multiply scattered acoustic waves. *Geophysical Journal International*, 203(3), 19231936.

Killick, R., Fearnhead, P., & Eckley, I. A. (2012). Optimal Detection of Changepoints With a Linear Computational Cost. *Journal of the American Statistical Association*, 107(500), 1590-1598. doi:10.1080/01621459.2012.737745

Klügel, A., Longpré, M. A., García-Cañada, L., & Stix, J. (2015). Deep intrusions, lateral magma transport and related uplift at ocean island volcanoes. *Earth and Planetary Science Letters*, 431, 140149. https://doi.org/10.1016/j.epsl.2015.09.031

Kohler, M. D., Heaton, T. H. and Bradford, S. C. (2007). Propagating Waves in the Steel, Moment-Frame Factor Building Recorded during Earthquakes. *Bulletin of the Seismological Society of America*, 97(4), 13341345.

Landés, M., Hubans, F., Shapiro, N.M.., Paul, A., & Campillo, M. (2010). Origin of deep ocean microseisms by using teleseismic body waves. *Journal of Geophysical Research*, 115(B05302):114.

Lavielle, M. (2005). Using penalized contrasts for the change-point problem. *Signal Processing*, 85(8), 1501-1510. doi:10.1016/j.sigpro.2005.01.012

Lecocq, T., Caudron, C. & Brenguier, F. (2014). MSNoise, a Python Package for Monitoring seismic velocity changes using ambient seismic noise. *Seismological Research Letters*, 85(3), 715-736. https://doi.org/10.1785/0220130073

Lehmann, I. (1936). P'. Bureau Central Sismologique International Strasbourg: *Publications du Bureau Central Scientifiques*, 14, 87-115.

Lehujeur, M., Vergne, J., Schmittbuhl, J. & Maggi, A. (2015). Characterization of ambient seismic noise near a deep geothermal reservoir and implications for interferometric methods: a case study in northern Alsace, France. *Geothermal Energy*, 3.

Liu, Z., Huang, J. & Li, J. (2010). Comparison of four techniques for estimating temporal change of seismic velocity with passive image interferometry. *Earthquake Science*, 23, 511518. https://doi.org/10.1007/s11589-010-0749-z

LonguetHiggins, M. S. (1950), A theory of the origin of microseisms. *Philosophical Transactions of the Royal Society A*, 243, 135.

López, C., Benito-Saz, M. A., Martí, J., del-Fresno, C., García-Cañada, L., Albert, H., & et al. (2017b). Driving magma to the surface: The 20112012 El Hierro volcanic eruption. *Geochemistry, Geophysics, Geosystems*, 18, 31653184. https://doi.org/10.1002/2017gc007023

López, C., Blanco, M. J., Abella, R., Brenes, B., Cabrera Rodríguez, V. M., Casas, B., et al. (2012). Monitoring the volcanic unrest of El Hierro (Canary Islands) before the onset of the 20112012 submarine eruption. *Geophysical Research Letters*, 39, L13303. https://doi.org/10.1029/ 2012GL051846

López, C., García-Cañada, L.Martí, J., & Domínguez Cerdeña, I.(2017a). Early signs of geodynamic activity before the 2011-2012 El Hierro eruption. *Journal of Geodynamics*, 104, 114. https://doi.org/10.1016/j.jog.2016.12.005

López, C., Martí, J., Abella, R., & Tarraga, M. (2014). Applying fractal dimensions and energy-budget analysis to characterize fracturing processes during magma migration and eruption: 20112012 El Hierro (Canary Islands) submarine eruption. *Surveys in Geophysics*, 35(4), 10231044. https://doi.org/10.1007/s10712-014-9290-2

Margerin, L., Campillo, M., Shapiro, N. M., & van Tiggelen, B. (1999). Residence time of diffuse waves in the crust and the physical interpretation of coda Q. Application to seismograms recorded in Mexico. *Geophysical Journal International*, 138, 343352.

Martí, J., Castro, A., Rodriguez, C., Costa, F., Carrasquilla, S., Pedreira, R., & et al. (2013). Correlation of magma evolution and geophysical monitoring during the 20112012 El Hierro (Canary Islands) submarine eruption. *Journal of Petrology*, 54(7), 13491373. https://doi.org/ 10.1093/petrology/egt014

Martí, J., Pinel, V., López, C., Geyer, A., Abella, R., Tárraga, M., & et al. (2013). Causes and mechanisms of the 20112012 El Hierro (Canary Islands) submarine eruption. *Journal of Geophysical Research: Solid Earth*, 118, 823839. https://doi.org/10.1002/jgrb.50087

Martí, J., Villasenor, A., Geyer, A., López, C., & Tryggvason, A. (2017). Stress barriers controlling lateral migration of magma revealed by seismic tomography. *Scientific Reports*, 7(1), 40757. https://doi.org/10.1038/srep40757

McNutt, S. R. (1996). Seismic monitoring and eruption forecasting of volcanoes: a review of the state-of-the-art and case histories. In Monitoring and mitigation of volcano hazards (pp. 99146). Berlin, Heidelberg: Springer.

Meier, U., Shapiro, N. M., & Brenguier, F. (2010). Detecting seasonal variations in seismic velocities within Los Angeles basin from correlations of ambient seismic noise. *Geophysical Journal International*. https://doi.org/10.1111/j.1365-246X.2010.04550.x

Meletlidis, S., Di Roberto, A., Cerdeña, I. D., Pompilio, M., Garca-Caada, L., Bertagnini, A., et al. (2015). New insight into the 2011-2012 unrest and eruption of El Hierro Island (Canary Islands) based on integrated geophysical, geodetical and petrological data. *Annals of Geophysics*, 58(5), S0546. https://doi.org/10.4401/ag-6754

Minato, S., Tsuji, T., Ohmi, S. & Matsuoka, T. (2012), Monitoring seismic velocity change caused by the 2011 Tohoku-oki earthquake using ambient noise records. *Geophysical Research Letters*, 39, L09309, doi:10.1029/2012GL051405.

Mordret, A., Mikesell, T. D., Harig, C., Lipovsky, B. P., & Prieto, G. A. (2016). Monitoring southwest Greenlands ice sheet melt with ambient seismic noise. *Science advances*, 2(5), e1501538.

Nakahara, H. (2014), Auto correlation analysis of coda waves from local earthquakes for detecting temporal changes in shallow subsurface structures: The 2011 Tohoku-Oki, Japan earthquake, *Pure and Applied Geophysics*, 172(2), 213224, doi:10.1007/s00024-014-0849-0.

Nishida, K., N. Kobayashi, & Y. Fukao (2000). Resonant oscillations between the solid earth and the atmosphere. *Science*, 287(5461), 22442246, doi:10.1126/science.287.5461.2244.

Obermann, A. (2013b). Monitoring the elastic properties of the crust: numerical analysis and applications using ambient seismic noise. PhD manuscript, Universitè de Grenoble

Obermann, A., Kraft, T., Larose, E., & Wiemer, S. (2015). Potential of ambient seismic noise techniques to monitor the St. Gallen geothermal site (Switzerland). *Journal of Geophysical Research: Solid Earth*, 120(6), 4301- 4316.

Obermann, A., Planès, T., Hadziioannou, C., & Campillo, M. (2016). Lapse-time-dependent coda-wave depth sensitivity to local velocity perturbations in 3-D heterogeneous elastic media. *Geophysical Journal International*, 207(1), 5966.

Obermann, A., Planès, T., Larose, E., Sens-Schönfelder, C., & Campillo, M. (2013a). Depth sensitivity of seismic coda waves to velocity perturbations in an elastic heterogeneous medium. *Geophysical Journal International*, 194(1), 372-382. https://doi.org/10.1093/gji/ggt043

Paasschens, J. C. J. (1997). Solution of the time-dependent Boltzmann equation, *Physical Review E*, 56(1), 11351141.

Pacheco, C., & Snieder, R. (2005). Time-lapse travel time change of multiply scattered acoustic waves. *The Journal of the Acoustical Society of America*, 118(3), 1300-1310.

Page, J., Schriemer, H., Bailey, A. & Weitz, D. (1995). Experimental test of the diffusion approximation for multiply scattered waves. *Physical Review E*, 52(3), 3106-3114.

Pérez N. M., Somoza L., Hernández, P. A., González de Vallejo, L., León, R., Sagiya, T., et al. (2014). Evidence from acoustic imaging for submarine volcanic activity in 2012 off the west coast of El Hierro (Canary Islands, Spain). *Bulletin of Volcanology*, 76(12):882896. doi:10.1007/s00445-014-0882-y

Pérez N. M., Somoza L., Hernández, P. A., González de Vallejo, L., León, R., Sagiya, T., et al. (2015). Reply to comment from Blanco et al. (2015) on "Evidence from acoustic imaging for submarine volcanic activity in 2012 off the west coast of El Hierro (Canary Islands, Spain)" by Pérez et al. [Bull. Volcanol.(2014), 76: 882896]. *Bulletin of Volcanology*, 77(7), 63.

Peterson, J. (1993), Observations and modeling of seismic background noise, USGS Open File Report, 93-322, 94 pp.

Picard, F., Robin, S., Lavielle, M., Vaisse, C., & Daudin, J. J. (2005), A Statistical Approach for Array cgh Data Analysis, *Bioinformatics*, 6. doi:10.1186/1471-2105-6-27.

Planès, T. (2013), Imaging local changes in the multiple scattering regime, PhD manuscript, Universitè de Grenoble

Poupinet, G., Ellsworth, W. & Frechet, J. (1984). Monitoring velocity varia- tions in the crust using earthquake doublets: an application to the Calaveras faults, California. *Journal of Geophysical Research.*, 89, 57195731.

Ratdomopurbo, A. & Poupinet, G. Monitoring a temporal change of seismic velocity in a volcano: Application to the 1992 eruption of Mt. Merapi (Indonesia). *Geophysical Research Letters* 22, 775778 (1995).

Roux, P., Song, H. C. & Kuperman, W. A. (2003), Time-reversal using ambient noise as a probe source, *Journal of the Acoustical Society of America*, 113, 2218.

Roux, P., Sabra, K. G., Gerstoft, P., Kuperman, W. A., & Fehler, M. C. (2005). Pwaves from crosscorrelation of seismic noise. *Geophysical Research Letters*, 32(19).

Saito, T. (2010), Love-wave excitation due to the interaction between a propagating ocean wave and the sea-bottom topography, *Geophysical Journal International*, 182(3), 1515, doi:10.1111/j.1365-246X. 2010.04695.x.

Sato, H. (1977). Energy propagation including scattering effects, single isotropic scattering approximation. *Journal of Physics of the Earth*, 25:2741.

Sato, H. (1993). Energy transportation in one- and two-dimensional scatter- ing media: Analytic solutions of the multiple isotropic scattering model, *Geophysical Journal International*, 112, 141146.

Schimmel, M. (1999). Phase cross correlations: Design, comparisons, and applications. *Bulletin of the Seismological Society of America*, 89(5), 13661378.

Schimmel, M., & Paulssen, H. (1997). Noise reduction and detection of weak, coherent signals through phase-weighted stacks. *Geophysical Journal International*, 130(2), 497-505.

Schimmel, M., Stutzmann, E., & Gallart, J. (2011). Using instantaneous phase coherence for signal extraction from ambient noise data at a local to a global scale. *Geophysical Journal International*, 184(1), 494506. https://doi.org/10.1111/j.1365-246X.2010.04861.x

Schimmel, M., Stutzmann, E., & Ventosa, S. (2018). Low-frequency ambient noise autocorrelations: Waveforms and Normal modes. *Seismological Research Letters*, 89, 14881496. https://doi.org/10.1785/0220180027

Schriemer, H., Cowan, M., Page, J., Liu, Z. & Weitz, D. (1997). Energy velocity of diffusing waves in strongly scattering media. *Physical Review Letters*, 79(17), 73166-3191.

Schuster, G. T., 2001, Theory of daylight/interferometric imaging: Tutorial: 63rd Conference & Technical Exhibition, EAGE, Extended Abstracts, A32.

Schwarz, G. (1978), Estimating the Dimension of a Model. *The Annals of Statistics*, 6, 461464.

Scott, A. J., & Knott, M. (1974). A Cluster Analysis Method for Grouping Means in the Analysis of Variance. *International Biometric Society*, 30(3), 507-512.

Seats, K. J., J. F. Lawrence, & G. A. Prieto (2012), Improved ambient noise correlation func- tions using welchs method, *Geophysical Journal International*, 188(2), 513, doi:10.1111/j.1365-246X.2011.05263. x.

Sens–Schönfelder, C., & Wegler, U. (2006), Passive image interferemetry and seasonal variations of seismic velocities at Merapi Volcano, Indonesia, *Geophysical Research Letters*, 33, L21302, doi:10.1029/2006GL027797.

Shang, T., & Gao, L. (1988). Transportation theory of multiple scattering and its application to seismic coda waves of impulsive source, *Scientia Sinica*, 31, 15031514.

Shapiro, N. M., & M. Campillo (2004), Emergence of broadband Rayleigh waves from cor- relations of the ambient seismic noise, *Geophysical Research Letters*, 31, L07614, doi:10.1029/ 2004GL019491.

Shapiro, N.M., Ritzwoller, M.H. & Bensen, G.D., 2006. Source location of the 26 sec microseism from cross correlations of ambient seismic noise, *Geophysical Research Letters*, 33, L18310, doi:10.1029/2006GL027010.

Snieder, R. (2004), Extracting Green's function from correlation of coda waves: A derivation based on stationary phase, *Physical Review E*, 69. doi:10.1103/PhyRevE. 69.046,610

Snieder, R., Gret, A., Douma, H. ,&d Scales, J. (2002). Coda wave interferometry for estimating nonlinear behavior in seismic velocity. *Science*, 295(5563), 22532255.

Snieder, R., & Hagerty, M. (2004). Monitoring change in volcanic interiors using coda wave interferometry: Application to Arenal Volcano, Costa Rica, *Geophysical Research Letters*, 31, L09608, doi:10.1029/2004GL019670.

Snieder,R. & Safak, E. (2006). Extracting the Building Response Using Seismic Interferometry: Theory and Application to the Millikan Library in Pasadena, California. *Bulletin of the Seismological Society of America*, 96(2), 586598.

Stehly, L., Campillo, M., & Shapiro, N. M. (2007). Traveltime measurements from noise correlation: stability and detection of instrumental time-shifts. Geophysical Journal International, 171, 223230

Stehly, L., Campillo, M., & Shapiro, N.M.. (2006). A study of the seismic noise from its long-range correlation properties. *Journal of Geophysical Research*, 111.

Stockwell, R. G., L. Mansinha, & R. P. Lowe (1996). Localization of the complex spectrum: The S transform, IEEE Trans. *Signal Processing*, 44(4), 9981001.

Stutzmann, E. Schimmel, M. & Ardhuin, F. (2011). Observing and modelling seismic noise. *Geophysical Journal International*.

Suda, N., K. Nawa, & Y. Fukao (1998), Earths background free oscillations, *Science*, 279, 20892091.

Tanimoto, T. (2005), The oceanic excitation hypothesis for the continuous oscillations of the earth, *Geophysical Journal International*, 160(1), 276, doi:10.1111/j.1365-246X.2004.02484.x.

Tanimoto, T., S. Ishimaru, & C. Alvizuri (2006), Seasonality in particle motion of microseisms, *Geophysical Journal International*, 166, 253266.

Tarantola, A. (2005). Inverse problem theory and methods for model parameter estimation. Society for Industrial Mathematics, Philadelphia, PA, pp. 1342.

Tarantola, A., & Valette, B. (1982). Generalized non-linear inverse prob- lems solved using the least-squares criterion, *Reviews of Geophysics*, 20(2), 219232

Taylor, W. A. (2000). Change-point analysis: a powerful new tool for detecting changes.

Telesca, L., Lovallo, M., Lpez, C., & Marti Molist, J. (2016). Multiparametric statistical investigation of seismicity occurred at El Hierro (Canary Islands) from 2011 to 2014. *Tectonophysics*, 672-673, 121128. https://doi.org/10.1016/j.tecto.2016.01.045

Tromp, J., Y. Luo, S. Hanasoge, & D. Peter (2010), Noise cross-correlation sensitivity kernels, *Geophysical Journal International*, 183, 791819.

Weaver, R. L., & Lobkis, O. I. (2001a). Ultrasonics without a source: Thermal fluctuation correlation at MHz frequencies, *Physical Review Letters*, 87, 134301.

Weaver, R. L., & Lobkis, O. I. (2001b). On the emergence of the Greens function in the correlations of a diffuse field, *Journal of the Acoustical Society of America*, 110, 3011 3017.

Wegler, U., & Sens–Schönfelder, C. (2007), Fault zone monitoring with passive image interferometry, *Geophysical Journal International*, 168(3), 1029-1033, doi:10.1111/j.1365-246X.2006.03284.x

Wiechert, E. (1899). Experimentelle Untersuchungen ber die Geschwindigkeit und die magnetische Ablenkbarkeit der Kathodenstrahlen. *Annalen der Physik*, 305(12), 739-766.

Annexes

A. Sánchez-Pastor, P., Obermann, A., & Schimmel, M. (2018). Detecting and locating precursory signals during the 2011 El Hierro, Canary Islands, submarine eruption. *Geophysical Research Letters*, 45. https://doi.org/10.1029/2018GL079550

Geophysical Research Letters

RESEARCH LETTER
10.1029/2018GL079550

Detecting and Locating Precursory Signals During the 2011 El Hierro, Canary Islands, Submarine Eruption

Pilar Sánchez-Pastor[1], Anne Obermann[2], and Martin Schimmel[1]

[1]Institute of Earth Sciences Jaume Almera-CSIC, Barcelona, Spain, [2]Swiss Seismological Service, ETH Zürich, Zurich, Switzerland

Key Points:
- Noise correlations to detect subsurface changes prior to their surface manifestation
- Spatial and temporal eruption precursors of a submarine volcano
- Potential of change point analysis of waveform similarity for real-time volcanic hazard assessment

Supporting Information:
- Supporting InformationS1
- Movie S1

Correspondence to:
P. Sánchez-Pastor,
psanchezsp@gmail.com

Citation:
Sánchez-Pastor, P., Obermann, A., & Schimmel, M. (2018). Detecting and locating precursory signals during the 2011 El Hierro, Canary Islands, submarine eruption. *Geophysical Research Letters*, *45*. https://doi.org/10.1029/2018GL079550

Received 17 JUL 2018
Accepted 13 SEP 2018
Accepted article online 17 SEP 2018

Abstract Forecasting and monitoring submarine volcanic eruptions represent a particular challenge due to the lack of direct surface observations. In the present study, we investigate the dynamics of the 2011 El Hierro submarine eruption using phase autocorrelation and cross-correlation from 2 years of continuous seismic records. Time evolution analysis of the waveform similarity allows us to clearly identify different preeruptive phases of this new volcano, as well as three magmatic intrusions that occurred in 2012. We use probabilistic sensitivity kernels to locate the places of the highest dynamics within the magmatic accumulation zone and the extinct volcanic area of Tiñor that might have acted as stress barriers, guiding the magma from the North of El Hierro Island to the final eruption site at the South. Our results highlight the potential of ambient noise methods to monitor volcanic hazard and unrest even with sparse data sets and limited knowledge of the region.

Plain Language Summary In 2011, a new volcano in the Canary Archipelago emerged at the southern edge of El Hierro Island after the archipelago had shown 40 years of quiescence. The volcanic eruption was submarine and unexpected, which impeded setting up instruments around the volcanic edifice and far in advance. This limited spatial distribution of instruments and the scarce data set of observables represent a particular challenge in forecasting and monitoring submarine volcanoes and motivated our research. We analyze the volcanic activity using 2 years of continuous seismic records from El Hierro Island. Our approaches involve methods from seismic interferometry as autocorrelation and cross correlation to determine waveform changes related to the different phases of volcanic activity and probabilistic sensitivity kernels of wave propagation to locate the places of the highest dynamics within the magmatic accumulation zone. Our results highlight the potential of ambient noise methods to forecast and monitor volcanic hazard and unrest even with sparse data sets in less known regions.

1. Introduction

Accurate volcanic hazard monitoring is an important step to mitigate the associated risk at local and regional scale. Standard equipment to deliver near-real-time observables includes GPS, tiltmeters, gas monitoring, cameras, and seismometers. While most before-mentioned methods are limited to surface observations, the analysis of seismic data provides a look at the processes occurring in the volcano interior. A standard tool is the study of the presence, quantity, and migration of microseismicity, which can yield important information about forthcoming and ongoing eruptions (e.g., Armbruster et al., 2014; Peng & Rubin, 2016; Roman, 2017). In the last decade, the study of waveform changes in the coda of seismic ambient noise correlations emerged as a complementary tool to gain information about ongoing deformations in the subsurface due to the movement of pressurized volcanic fluids that alter the elastic and scattering properties of the surrounding medium (e.g., Brenguier et al., 2008; De Plaen et al., 2016; Obermann, Planès, Larose, & Campillo, 2013). Studying the interior dynamics is of particular importance for submarine volcanoes, where direct surface measurements are not available.

In 2011, a new volcano in the Canary Archipelago emerged at the Southern edge of El Hierro Island after the Canary archipelago had shown 40 years of quiescence. The volcanic eruption was preceded by an intense seismic unrest with a characteristic migration over time from the Northern El Golfo region toward the final eruption site at the southern tip of the island (Figure 1). Over the past years, this eruption has been studied in depth to elucidate the associated processes with different approaches: tomographic studies (García-Yeguas et al., 2014; Martí et al., 2017), modeling of the geodetic pressure sources (López, Benito-Saz, et al., 2017), microseismic sounding methods (Gorbatikov et al., 2013), and fractal dimension analysis (López

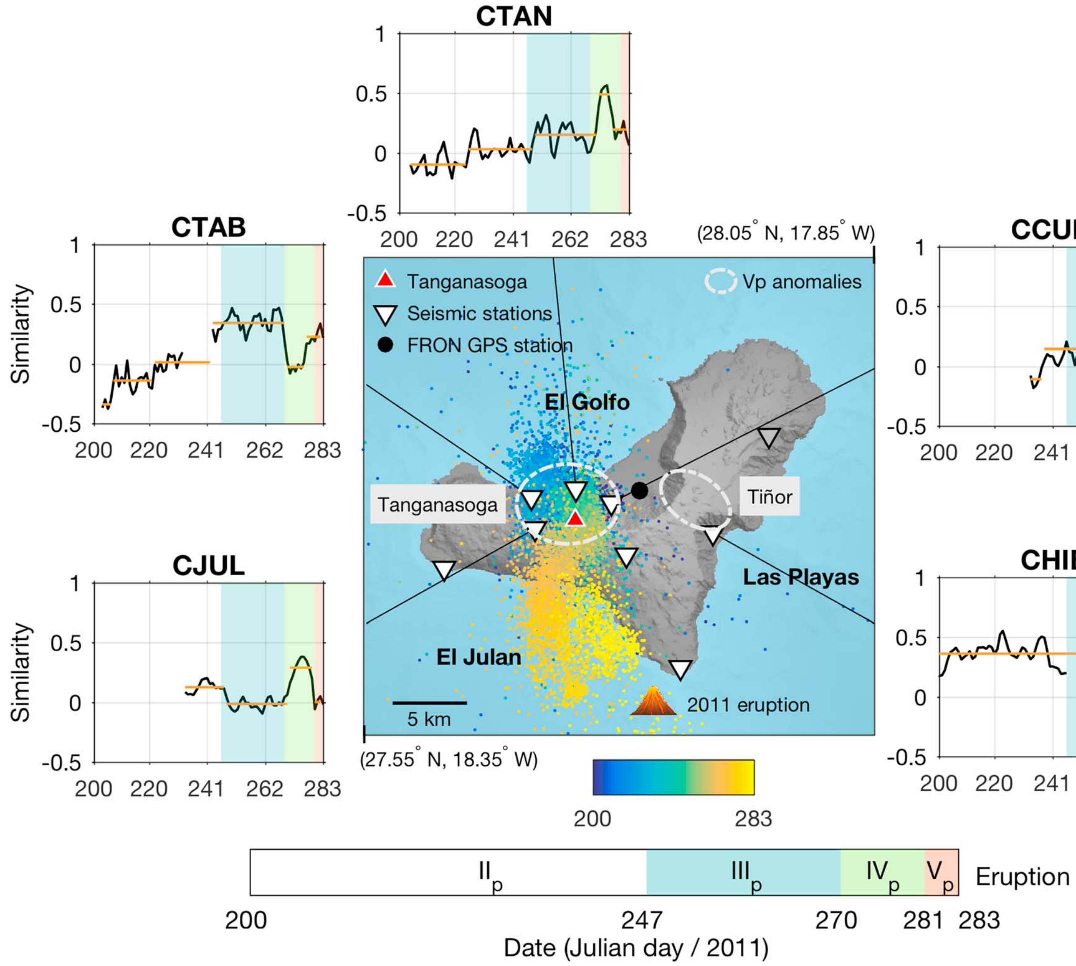

Figure 1. Inner part: Map of El Hierro Island. Inverted triangles mark the location of the seismic stations. The station in gray has been discarded due to problems with its frequency content. The black dot marks the GPS station FRON. The time evolution of the seismicity prior to the eruption in 2011 is marked with colored dots. The gray dashed circles highlight the Tanganasoga and Tiñor volcanic areas that are marked by high V_p anomalies (Martí et al., 2017). Outer part: Similarity curves at 16–22 s of lag time for various autocorrelations. Orange, horizontal lines mark time periods delimited by abrupt changes in the average of the waveform similarity, as obtained from the change point analysis. Background colors indicate the preeruptive phases of López et al. (2012) and are labeled with the subscript *p*.

et al., 2014). Precursory unrest indicators have been suggested from on-land GPS and seismicity data (e.g., López et al., 2012; López, García-Cañada, et al., 2017).

In our study, we investigate the potential of ambient noise correlation combined with coda wave interferometry to shed light on the dynamic evolution of the El Hierro submarine volcano, with a special focus on the preeruptive period in 2011 and three intrusions throughout 2012. Working with a sparse data set, we put emphasis on the accuracy, sensitivity, and statistical relevance of our findings. We use phase autocorrelation (AC) and phase cross correlation (CC, Schimmel, 1999) to increase the temporal accuracy of the correlations and study the time evolution of waveform similarity at various coda lag time windows. The statistically relevant changes of the different phases of the 2011 preeruptive and changes related to the 2012 intrusive periods are mapped in 2-D using probabilistic sensitivity kernels. We then discuss and interpret our results in comparison with other geophysical studies.

2. Framework of the El Hierro Eruption

The new submarine El Hierro volcano is situated on the southern flank of the homonymous island that forms part of the Canary Archipelago (Figure 1) at 900 m below sea level (Martí, Castro, et al., 2013) and about 5-km distance from the town of La Restinga. The El Hierro Island, with the oldest subaerial rocks of 1.2 Ma, is the youngest island of the volcanically active Canary Archipelago, located at its southwestern corner (Guillou et al., 1996). Over the past few thousand years, the most important eruptions in El Hierro are related to Tanganasoga, a volcano inside the El Golfo depression (Figure 1) and the extinct volcanic area of Tiñor in the east/northeast of the island (Figure 1). Both regions are clearly noticeable as high velocity zones in tomography and microseismic sounding studies that show feeding channels down to 10 km (García-Yeguas et al., 2014; Gorbatikov et al., 2013; Martí et al., 2017). Both studies could also highlight a significant magmatic accumulation at depth below the central part of El Hierro Island.

The Canary archipelago has been volcanically active with several eruptions in the last five centuries (Carracedo, 1994). After the 1971 eruption of Teneguia in La Palma (Martí, Pinel, et al., 2013), the archipelago remained in quiescence for four decades.

In July 2011, a sudden onset of microseismic activity was observed at the north of El Hierro Island in the El Golfo depression (Figure 1, phase II_p). The microseismic activity was produced by a magmatic intrusion that manifested itself in terms of surface deformation (López et al., 2012). More than 11,000 seismic events were detected, migrating southward crossing the island (phase III_p). After a short period of acceleration of the volcanic processes (phase IV_p), the unrest culminated after a few days of system stabilization (phase V_p) in the volcanic eruption of El Hierro submarine volcano. The eruption started on 10 October 2011 on a north-south trending fissure in the southern flank of the island (Martí, Pinel, et al., 2013), with the onset of strong volcanic tremor. However, the first surface observations in terms of strong bubbling due to degassing appeared a few days later (López et al., 2012). For comparison with our results, the phases of unrest as defined in López et al., 2012 are marked in color in Figure 1. The dominant frequency of the tremor oscillates from 0.5 to 1.9 Hz during the eruption period (Tárraga et al., 2014). The tremor lasted until late February 2012 (Figures 2a and 2b), but a clear end of the eruption could not be defined by previous studies. The regional government emergency committee (PEVOLCA) announced the end of the eruption on 5 March 2012. This was the first eruption on the Canary Islands to be monitored in real time by various geophysical instruments from the Spanish National Geographic Institute.

From 2012 to 2014, several magmatic intrusions have been inferred at different parts of the island, which, however, did not culminate in eruptions (Díaz-Moreno et al., 2015; Garcia et al., 2014; González et al., 2013; Klügel et al., 2015; Meletlidis et al., 2015; Telesca et al., 2016).

3. Data and Methods

3.1. Seismic Data and Preprocessing

We analyze 2 years of ambient seismic noise records from seven broadband stations and one short-period station deployed by the Spanish National Geographic Institute in 2011 (white triangles, Figure 1). Two stations covered the beginning of the unrest in July 2011; a total of six stations were running by mid-August, and additional two were set up in October, including the station at the southern tip of El Hierro Island. We compare our results with surface deformation measurements from a GPS station, FRON, belonging to the Canarian Regional Government (black circle, Figure 1). There was an additional seismic station (CTIG, marked in gray in Figure 1), which was located in direct vicinity of a wind park and recorded perturbed waveforms in the frequency bands of interest.

The available data are scarce, and detectable medium changes are likely smaller than observed in volcano monitoring studies, where the stations could be located directly on the volcanic edifice (e.g., Brenguier et al., 2008; Grêt, 2005; Obermann, Planès, Larose, & Campillo, 2013; Takano et al., 2017). Therefore, we use the phase CC (Schimmel, 1999) instead of the classical correlation. Phase CC enables a quicker convergence rate since the data do not require preprocessing to reduce the amplitude bias caused by seismicity and other energetic signals, and it has an intrinsic higher sensitivity to small waveform changes in comparison to the classical correlation (Schimmel et al., 2011, 2018). The approach has been employed successfully in other noise-based monitoring and imaging studies (e.g., D'Hour et al., 2015; Romero & Schimmel, 2018).

As we want to associate observed temporal changes solely to processes in the subsurface, we have to work in frequency bands that are not subject to intense source fluctuations, which likely are not compensated by secondary scattering (Zhan et al., 2013). Different frequency bands have been tested, and the band (2.0–6.0) Hz

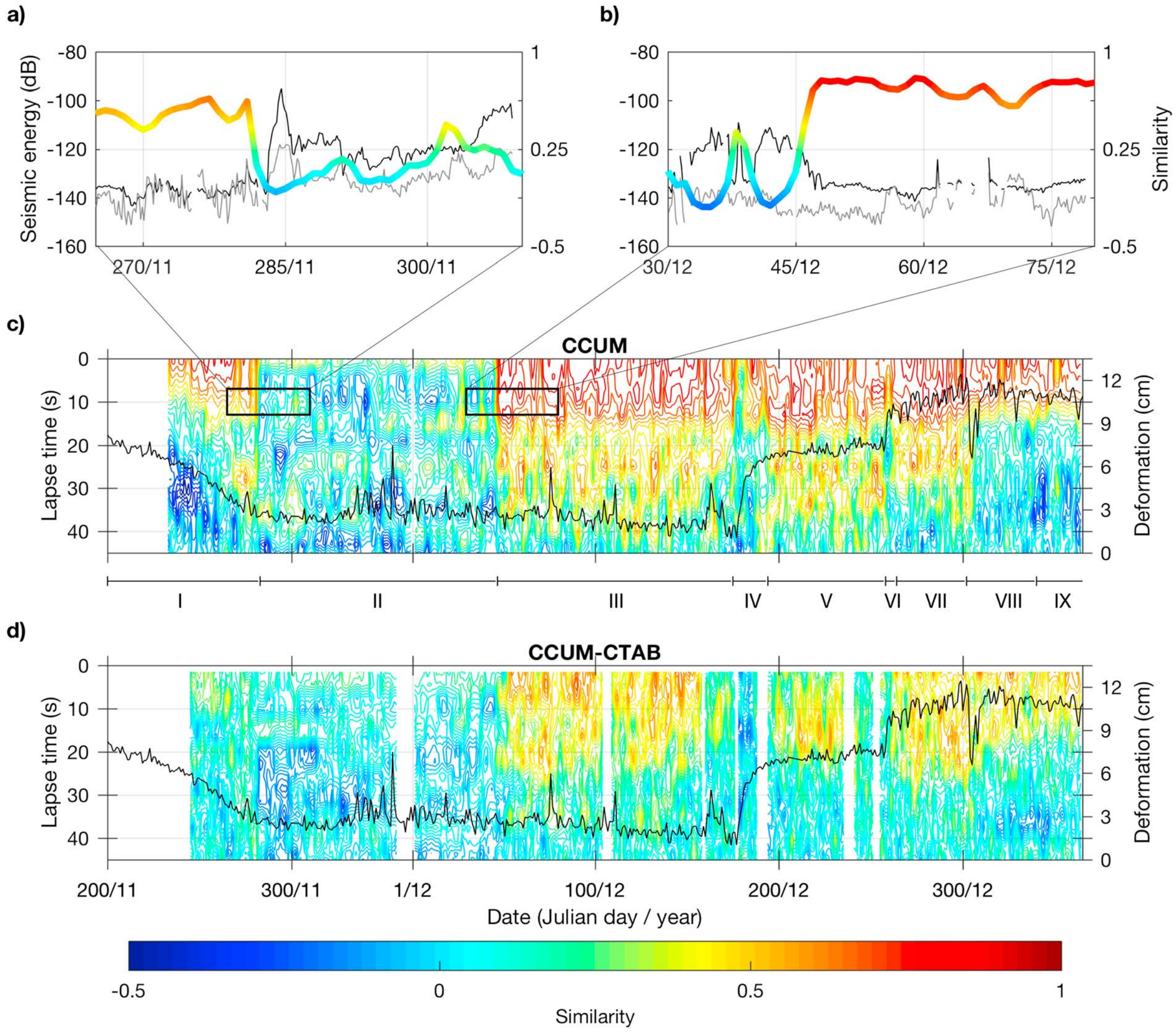

Figure 2. (c, d) Lag time-dependent waveform similarity for the 2 years of study from autocorelation (CCUM) and cross correlation (CCUM-CTAB). The black line represents the modulus of the three components of the surface deformation estimated from GPS station FRON. We mark nine periods of volcanic activity (I–IX). (a, b) Zoom into the waveform similarity around 10-s lag time for the beginning and end of the volcanic eruption. The seismic energy calculated for CCUM is shown at 1 (black) and 4 Hz (gray).

turned out to be optimal, since it provides the most stable seismic response during time intervals without volcanic activity. The chosen frequency band overlaps with the dominant tremor frequencies, which can change the wave field fluctuations significantly. We therefore restrict the study to noneruptive periods.

Our data preparation consists of the following steps: (1) Cutting and decimating the recordings into 1-hr-long segments at 50-Hz sampling frequency, discarding segments with more than 10^4 missing samples. (2) Deconvolving the instrument response function to ground velocity. (3) Applying a 2.0- to 6.0-Hz band-pass filter. (4) Computing ACs and CCs for the vertical component of all station combinations at (−50, 50) seconds lag time. (5) Stacking the correlations linearly with a 3-day sliding data window. This window length is long enough to retrieve stable noise responses during the calm periods.

3.2. Time Evolution of Waveform Similarity

Our main objective is to identify precursory signals and different phases of volcanic activity for the 2 years of interest. We determine the similarity between the daily correlations (CC^{curr}) and their corresponding reference trace (CC^{ref}) as the zero-lag cross correlation in sliding 7-s-long lag time windows with 3-s overlap within the coda. Thus, we obtain the time dependent waveform similarity as a function of the lag time window j and day of measurement i as

$$S_{ij} = PCC\left[CC_j^{\mathrm{ref}}, CC_{ij}^{\mathrm{curr}}\right]$$

CC^{ref} is calculated stacking all correlations excluding the eruption period (283/2011 to 50/2012). We average negative and positive lag time similarity values.

In Figures 2c and 2d we show the waveform similarity of a typical AC and CC with the respective reference trace at various lag times until the end of 2012. The similarity ranges from -1 (anticorrelation, blue) to 1 (identical, red). Similarity, values are higher for ACs than CCs (Figures 2c and 2d).

Throughout the 1.5 years, we can identify various patterns, which are distinguished by marked similarity changes (I–IX, Figure 2). The low similarity values (period II) correspond to the eruption with intense tremor activity. The waveform similarity allows to clearly identify the beginning (283/2011) and ending (46/2012) of the eruption (Figures 2a and 2b). We here plot the mean of the similarity around 10-s lag time (colored lines) together with the daily mean seismic energy at 1 (black) and 4 Hz (gray). One hertz is the dominant tremor frequency (Tárraga et al., 2014), and 4 Hz is the middle of the frequency band we use in this study. While the beginning of the eruption (Figure 2a) was accompanied by strong volcanic tremor and can also be distinguished through the increase of seismic energy, the end of the eruption cannot be clearly determined from the seismic energy (Figure 2b). Throughout period II, the influence of the volcanic tremor is still present in our frequency band of interest and does not allow measuring any structural change during this period.

Additionally, we compare the lag time-dependent similarity with the surface deformation (Figures 2c and 2d) measured at a nearby GPS station (black circle, Figure 1). Sudden rises of surface deformation correlate well with a decrease in similarity over a broad range of lag times (periods IV and VI). Seismic stations with sufficient preeruptive data show a subtler but significant similarity variation prior to eruption, which correlates with a small surface deformation rise within the period I (day 270/2011).

To assess the robustness of our results despite the choice of reference, five other reference traces have been tested (Figure S1 in the supporting information). The choice of reference has an influence on the absolute similarity values but does not change the main pattern.

3.3. Statistical Relevance of Changes in the Preeruptive Phases

To show the statistical relevance of the changes in similarity that we interpret as precursory signals, we use a statistical method to detect potential change points in our data (Killick et al., 2012).

The precursory signals should be related to the magma feeding, which is expected to happen at around 10 km depth, the dominant depth of the seismicity previous to the eruption (López et al., 2012). Considering an empirical apparent velocity for scattered waves of 1 km/s (Gorbatikov et al., 2013; Meier et al., 2010; Zhan et al., 2013), we analyze the similarity changes for autocorrelations in 16- to 22-s lag time windows, to be sensitive to the target depth.

For the statistical analysis, we determine the mean and standard deviation of the waveform similarity during the calm period in the above-mentioned lag time window (period III Figures 2c and 2d).

Minimizing a cost function (Killick et al., 2012), we determine the change points whether the mean of similarity changes significantly. The significance is defined as 1.5 times the characteristic standard deviation during the calm period. In Figure 1, we mark the time periods with statistically different similarity averages with horizontal lines.

We observe clear similarity changes corresponding to the eruptive phases as defined by López et al. (2012; marked with colors in Figure 1 and discussed in section 2). The advantage of the change point analysis is that it offers an automatic tool to discriminate periods without significant changes in the studied variable.

3.4. Two-Dimensional Spatial Distribution of Structural Changes

To locate medium changes, we use a linear least squares inversion procedure (Tarantola & Valette, 1982) based on probabilistic sensitivity kernels (e.g., Larose et al., 2010; Obermann, Planès, Larose, Sens-Schönfelder, et al., 2013; Pacheco & Snieder, 2005; Planès et al., 2014; Rosetto et al., 2011). These kernels describe the intensity of wave propagation with the two-dimensional radiative transfer theory, valid since surface waves are dominant (Paasschens, 1997; Sato, 1993; Shang & Gao, 1988) and can be seen as a probabilistic spatial distribution of the locations of the medium changes. What we invert is the decorrelation that we calculate as the absolute difference between the similarity curves from ACs and CCs at specific time windows, and the average from the calmest period (III). The inversion then provides 2-D scattering cross-section density maps that represent a proxy of the capacity of the medium perturbation to deviate waves that depends on the size and strength of the structural changes. For the construction of the sensitivity kernels, we use a rough approximation of the transport mean free path of 30 km, comparing with attenuation studies of other volcanoes (Del Pezzo et al., 2001; Obermann, Planès, Larose, & Campillo, 2013; Prudencio et al., 2013). Obermann, Planès, Larose, and Campillo (2013) have shown that in this type of inversion, an inaccurate transport mean free path has an influence on the size of the affected area, but not on the horizontal localization itself. At different lag times, the sampled region in the subsurface changes, as the diffusive halo of the coda waves changes. We then consider lag times from 5 to 45 s and sliding lag time windows of 10-s lengths with 50% overlap. In the supporting information (Figure S2) we show that our results barely depend on these approximated parameters.

In Figure 3, we show the scattering cross-section density maps at various lag times for the preeruptive phase (IV_p) in 2011 (a), as well as preintrusion (III, b) and intrusion phases in June 2012 (IV, c), September 2012 (V, d and VI, e), and January 2013 (IX, g). Figure 3f shows a quiet period (III) with absence of any changes. We hence conclude that the inversion does not generate significant medium changes nor artifacts, which might cause ambiguities in the interpretations.

In Figure 3a, we see that the changes due to the 2011 preeruptive phase are located in the interior of the Golfo Valley around the Tanganasoga volcano and toward the east in the extinct volcanic area Tiñor. These areas correspond to regions with strong V_p anomalies at shallow depth (Figure 3a, first panel; Martí et al., 2017). Also, the intrusions in 2012 produce subsurface perturbations in these regions with varying sizes and intensities. The location of the changes during the preintrusion phases, lasting for 20 days in June and 15 days in September 2012 (Figures 3b and 3d) correspond to the location of the final intrusions (Figures 3c and 3e) with lower intensity. For each of the dynamic phases, we added the recorded seismicity during the respective phases. Please note, that the location of seismicity does not correspond to the highlighted areas in the scattering cross-section maps.

To test the robustness of our results, we calculated the inversion systematically removing every single station at 20 s of lag time for the phase IV_p (Figure S3). Given the sparse network, the dependency on the seismic network geometry is evident. Nevertheless, the spatial distribution of the changes persists.

4. Interpretation and Discussion

In the following, we discuss our results in the context of the evolution and dynamics of this new submarine volcano.

The waveform similarity analysis allows us to detect with great detail all five preeruptive phases (Figure 1, outer part) as defined in López et al., 2012 with various methods (GPS, seismicity, gas detection, etc.). Only one station reliably recorded the beginning of the unrest (phase I_p). The second preeruptive phase (II_p) is characterized by an important increase of the seismicity, recording up to 450 events per day. We observe a change in similarity in the middle of II_p by the stations in the North (Figure 1, CTAB and CTAN) that could suggest an additional preeruptive phase, for instance, in the form of strong upwelling of the magma. López, Benito-Saz, et al. (2017) also observe a perturbation in the real-time seismic amplitude measurement for this period but leave the underlying processes uncommented.

The third phase (III_p) is characterized by a southward migration of seismicity. This migration starts after a significant change in the scattering cross section below the Tanganasoga volcano, in fact, the largest change in the cross section that we observe in our study (Movie S1). On day 270 (IV_p beginning) the released seismic energy increased drastically as well as alterations of surface deformation and gas emissions (López et al., 2012). All of our stations detect a strong change in similarity (Figure 1) that starts 2 days prior to the strong surface deformations measured by GPS (Figure 2c, I, 25- to 30-s lag time). We think that we already measure a subsurface imprint of the magma movement that causes the surface deformation. During phase V_p (Figure 1)

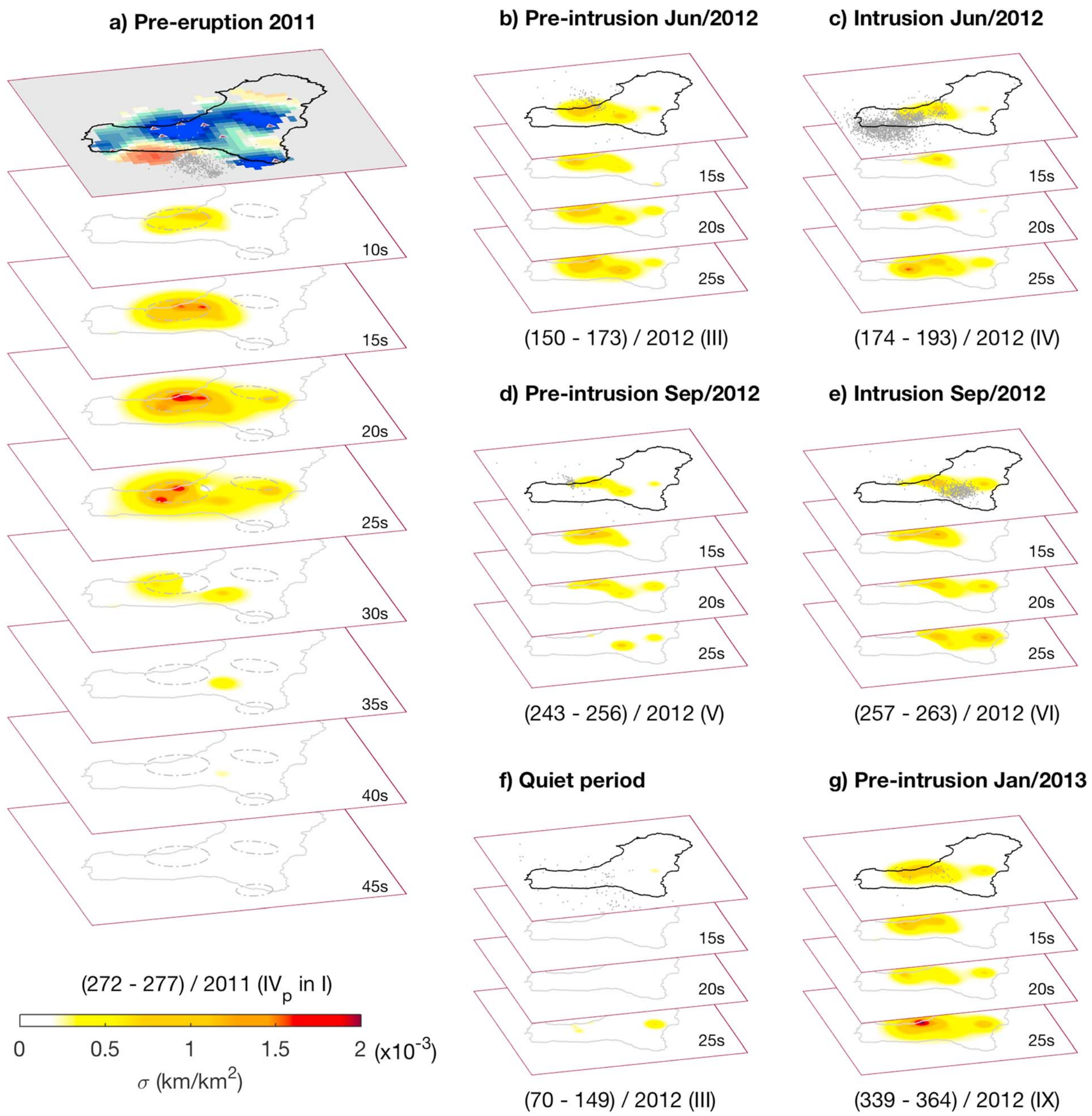

Figure 3. Scattering cross-section density maps at various lag times for different periods. (a) Prior to the eruption. (b, c) Premagmatic and comagmatic intrusion of June 2012. (d, e) Premagmatic and comagmatic intrusion of September 2012. (f) Calmest period. (g) Preintrusion of January 2013. The days averaged are indicated below every panel together with their corresponding time period. The seismicity of the corresponding time periods is marked by gray dots. First panel in (a) represent a *P* wave tomography at 4- to 5-km depth (adapted from Martí et al., 2017). The gray dashed circles in subsequent panels highlight the regions with 8% of V_p perturbations.

prior to the eruption, we observe a short recovery of the similarity values. Such a phase of system stabilization is often preceding volcanic eruptions by days or weeks (e.g., McNutt, 1996).

The El Hierro volcanic eruption initiates the period II (283/2011). This period is clearly identified through a sudden decrease in the measured similarity (Figures 2a, 2c, and 2d). While the beginning of the eruption can also be clearly identified via the volcanic tremor onset (Figure 2a), its end was a question of interpretation (5 March according to PEVOLCA), as the tremor energy decreases erratically (Figure 2b). Here the results from our waveform similarity can clearly set the end of the main magmatic emission to the 15 February (46/2012), where we observe an abrupt increase in similarity. After this day, few lava balloons were observed in the ocean (Longpre et al., 2014; Martí, Castro, et al., 2013) coinciding in time with some of the observed medium perturbations (Movie S1).

Throughout the year 2012, there were three magmatic intrusions (Figures 2c and 2d, phases IV, VI, and late IX) that, however, did not lead to magmatic eruptions (e.g., Benito-Saz et al., 2017; Lamolda et al., 2017). All three intrusions can be clearly seen in terms of surface deformation on the GPS measurements (Figures 2c and 2d). Coinciding with each change in deformation, we observe a decorrelation of the waveforms (negative or no similarity) that is observed over various lag times (Figures 2c and 2d). When studying the spatial distribution of these changes, the scattering cross-section maps (Figure 3 and Movie S1) show clear precursory perturbations at the location of the final intrusion. The precursory signals typically appear several days prior to the intrusions. The order of magnitude of the scattering cross-section density values are consistent with similar analysis in different environments (Obermann, Planès, Larose, & Campillo, 2013; Obermann et al., 2014).

On the GPS data, we see a very prominent peak on day 302, which seems to be an artifact caused by atmospherics instabilities (Spanish Meteorological Agency, http://www.aemet.es) that produce a delay in the GPS signal. This anomalous behavior coincides in time with the beginning of a similarity perturbation of later lag times in the autocorrelations, which extends until late 2012 (periods VIII–IX).

Tomography studies of El Hierro Island point to two intrusive bodies beneath the island (Figure 3a, first panel). One body is located in the North of El Hierro Island, rises from the lithospheric mantle, and reaches the surface below the Tanganasoga volcano, at the interior of El Golfo Valley (Figure 1). The other body is a vertical feeder channel, located in the eastern zone of El Golfo valley, in the extinct volcanic area of Tiñor (Figure 1). These areas correspond well with the locations of the strongest changes in our scattering cross section maps (Figure 3). The concentration of overpressure in these areas could lead to a significant impact of the scattering properties of the subsurface. We think that our observation confirms that these dense magmatic bodies could act as stress barriers, guiding the magma from the Northern El Golfo region to the Southern tip of El Hierro Island, as observed during the seismicity migration (García-Yeguas et al., 2014; Martí et al., 2017). We observe for all intrusive phases, that the locations of the preintrusion (with little to no indicative seismicity; Figure 3) correspond to the location of the final intrusion, highlighting the potential for precursory alarming. Due to the sparse dataset and limited coverage of the island, we could not follow the migration of magma from the North to South for the eruption in 2011. In 2012, varying numbers of the eight stations are running during the time of the intrusions, but in all cases, the network geometry limits our imaging resolution to the central part of El Hierro Island. We present the scattering cross section maps for different lag times (Figure 3) to get an approximate constraint on the depth of the changes (Obermann, Planès, Larose, Sens-Schönfelder, et al., 2013). The changes are most pronounced at about 20- to 25-s lag time and slowly disappear afterward. The affected region should hence be limited to the upper few kilometers.

5. Conclusions

In this study, we analyzed the waveform similarity from the phase correlations of 2 years of ambient seismic noise in El Hierro Island for a wide range of coda lag times. Marked by significant changes in waveform similarity, we can distinguish several phases of preeruptive unrest related to the appearance of the new submarine volcano El Hierro, at the southern tip of the island in October 2011. We used a change point analysis to test the robustness and significance of our measurements.

Our results allow us to pinpoint the beginning and end of the submarine eruption to exact dates (10 October 2011 to 15 February 2012). In particular the end of the eruption remained vague from previous geophysical studies. Throughout 2012, we could detect and locate subsurface changes related to three magmatic intrusions prior to their surface manifestation. The locations of the changes correspond to feeder channels determined by tomographic studies and are interpreted to act as stress barriers for the magmatic movement.

The data set we analyzed is sparse with a limited spatial coverage. However, we are very optimistic that a denser seismic network would allow us to follow magmatic movements in real time and great detail. Combined with a statistical analysis, such as the change point approach, the data analysis could be automated, providing important information for an early hazard assessment.

Acknowledgments
We would like to thank the Spanish National Geographic Institute (IGN), which participated in the monitoring of the 2011 El Hierro eruption and furnished the waveform seismic records used in this study (volcanologia@fomento.es). The earthquake catalog can be requested from their website (http://www.ign.es). The GPS station FRON belongs to the Canarian Regional Government (GRAFCAN) and can be downloaded from http://www.idecanarias.es/resources/GNSS/Resenias/FRON.pdf. Pilar Sánchez-Pastor acknowledges funding from the Spanish Ministry of Economy and Competitiveness (project MISTERIOS, CGL2013-48601-C2-2-R). The work has benefited from discussions within the EU-funded COST action ES1401 TIDES (TIme DEpendent Seismology). We also thank the Editor Rebecca Carey and two anonymous reviewers for comments that helped improve the manuscript.

References

Armbruster, J. G., Kim, W.-Y., & Rubin, A. M. (2014). Accurate tremor locations from coherent *S* and *P* waves. *Journal of Geophysical Research: Solid Earth*, *119*, 5000–5013. https://doi.org/10.1002/2014jb011133

Benito-Saz, M. A., Parks, M. M., Sigmundsson, F., Hooper, A., & García-Cañada, L. (2017). Repeated magmatic intrusions at El Hierro Island following the 2011–2012 submarine eruption. *Journal of Volcanology and Geothermal Research*, *344*, 79–91. https://doi.org/10.1016/j.jvolgeores.2017.01.020

Brenguier, F., Shapiro, N. M., Campillo, M., Ferrazzini, V., Duputel, Z., Coutant, O., & et al. (2008). Towards forecasting volcanic eruptions using seismic noise. *Nature Geoscience*, *1*(2), 126–130. https://doi.org/10.1038/ngeo104

Carracedo, J. C. (1994). The Canary Islands—An example of structural control on the growth of large oceanic-island volcanoes. *Journal of Volcanology and Geothermal Research*, *60*(3-4), 225–241. https://doi.org/10.1016/0377-0273(94)90053-1

De Plaen, R. S. M., Lecocq, T., Caudron, C., Ferrazzini, V., & Francis, O. (2016). Single station monitoring of volcanoes using seismic ambient noise. *Geophysical Research Letters*, *43*, 8511–8518. https://doi.org/10.1002/2016GL070078

Del Pezzo, E., Bianco, F., & Saccorotti, G. (2001). Separation of intrinsic and scattering Q for volcanic tremor: An application to Etna and Masaya Volcanoes. *Geophysical Research Letters*, *28*, 3083–3086. https://doi.org/10.1029/2001GL013372

D'Hour, V., Schimmel, M., Do Nascimento, A. F., Ferreira, J. M., & Lima Neto, H. C. (2015). Detection of subtle hydromechanical medium changes caused by a small-magnitude earthquake swarm in NE Brazil. *Pure and Applied Geophysics*, *173*(4), 1097–1113. https://doi.org/10.1007/s00024-015-1156-0

Díaz-Moreno, A., Ibáñez, J. M., De Angelis, S., García-Yeguas, A., Prudencio, J., Morales, J., et al. (2015). Seismic hydraulic fracture migration originated by successive deep magma pulses: The 2011–2013 seismic series associated to the volcanic activity of El Hierro Island. *Journal of Geophysical Research: Solid Earth*, *120*, 7749–7770. https://doi.org/10.1002/2015JB012249

Garcia, A., Fernandez-Ros, A., Berrocoso, M., Marrero, J. M., Prates, G., De la Cruz-Reyna, S., & et al. (2014). Magma displacements under insular volcanic fields, applications to eruption forecasting: El Hierro, Canary Islands, 2011–2013. *Geophysical Journal International*, *197*(1), 322–334. https://doi.org/10.1093/gji/ggt505

García-Yeguas, A., Ibáñez, J. M., Koulakov, I., Jakovlev, A., Romero-Ruiz, M. C., & Prudencio, J. (2014). Seismic tomography model reveals mantle magma sources of recent volcanic activity at El Hierro Island (Canary Islands, Spain). *Geophysical Journal International*, *199*(3), 1739–1750. https://doi.org/10.1093/gji/ggu339

González, P. J., Samsonov, S. V., Pepe, S., Tiampo, K. F., Tizzani, P., Casu, F., et al. (2013). Magma storage and migration associated with the 2011–2012 El Hierro eruption: Implications for crustal magmatic systems at oceanic island volcanoes. *Journal of Geophysical Research: Solid Earth*, *118*, 4361–4377. https://doi.org/10.1002/jgrb.50289

Gorbatikov, A. V., Montesinos, F. G., Arnoso, J., Stepanova, M. Y., Benavent, M., & Tsukanov, A. A. (2013). New features in the subsurface structure model of El Hierro Island (Canaries) from low-frequency microseismic sounding: An insight into the 2011 Seismo-volcanic crisis. *Surveys in Geophysics*, *34*(4), 463–489. https://doi.org/10.1007/s10712-013-9240-4

Grêt, A. (2005). Monitoring rapid temporal change in a volcano with coda wave interferometry. *Geophysical Research Letters*, *32*, L06304. https://doi.org/10.1029/2004GL021143

Guillou, H., Carracedo, J. C., Perez-Torrado, F. J., & Rodriguez Badiola, E. (1996). K-Ar ages and magnetic stratigraphy of a hotspot-induced, fast grown oceanic island—El Hierro, Canary Islands Author links open overlay panel. *Journal of Volcanology and Geothermal Research*, *73*(1-2), 141–155. https://doi.org/10.1016/0377-0273(96)00021-2

Killick, R., Fearnhead, P., & Eckley, I. A. (2012). Optimal detection of changepoints with a linear computational cost. *Journal of the American Statistical Association*, *107*(500), 1590–1598. https://doi.org/10.1080/01621459.2012.737745

Klügel, A., Longpré, M.-A., García-Cañada, L., & Stix, J. (2015). Deep intrusions, lateral magma transport and related uplift at ocean island volcanoes. *Earth and Planetary Science Letters*, *431*, 140–149. https://doi.org/10.1016/j.epsl.2015.09.031

Lamolda, H., Felpeto, A., & Bethencourt, A. (2017). Time lag between deformation and seismicity along monogenetic volcanic unrest periods: The case of El Hierro Island (Canary Islands). *Geophysical Research Letters*, *44*, 6771–6777. https://doi.org/10.1002/2017gl074494

Larose, E., Planes, T., Rossetto, V., & Margerin, L. (2010). Locating a small change in a multiple scattering environment. *Applied Physics Letters*, *96*(20). https://doi.org/10.1063/1.3431269

Longpre, M. A., Klugel, A., Diehl, A., & Stix, J. (2014). Mixing in mantle magma reservoirs prior to and during the 2011-2012 eruption at El Hierro, Canary Islands. *Geology*, *42*(4), 315–318. https://doi.org/10.1130/g35165.1

López, C., Benito-Saz, M. A., Martí, J., del-Fresno, C., García-Cañada, L., Albert, H., & et al. (2017). Driving magma to the surface: The 2011–2012 El Hierro volcanic eruption. *Geochemistry, Geophysics, Geosystems*, *18*, 3165–3184. https://doi.org/10.1002/2017gc007023

López, C., Blanco, M. J., Abella, R., Brenes, B., Cabrera Rodríguez, V. M., Casas, B., et al. (2012). Monitoring the volcanic unrest of El Hierro (Canary Islands) before the onset of the 2011–2012 submarine eruption. *Geophysical Research Letters*, *39*, L13303. https://doi.org/10.1029/2012GL051846

López, C., García-Cañada, L., Martí, J., & Domínguez Cerdeña, I. (2017). Early signs of geodynamic activity before the 2011–2012 El Hierro eruption. *Journal of Geodynamics*, *104*, 1–14. https://doi.org/10.1016/j.jog.2016.12.005

López, C., Martí, J., Abella, R., & Tarraga, M. (2014). Applying fractal dimensions and energy-budget analysis to characterize fracturing processes during magma migration and eruption: 2011–2012 El Hierro (Canary Islands) submarine eruption. *Surveys in Geophysics*, *35*(4), 1023–1044. https://doi.org/10.1007/s10712-014-9290-2

Martí, J., Castro, A., Rodriguez, C., Costa, F., Carrasquilla, S., Pedreira, R., & et al. (2013). Correlation of magma evolution and geophysical monitoring during the 2011–2012 El Hierro (Canary Islands) submarine eruption. *Journal of Petrology*, *54*(7), 1349–1373. https://doi.org/10.1093/petrology/egt014

Martí, J., Pinel, V., López, C., Geyer, A., Abella, R., Tárraga, M., & et al. (2013). Causes and mechanisms of the 2011–2012 El Hierro (Canary Islands) submarine eruption. *Journal of Geophysical Research: Solid Earth*, *118*, 823–839. https://doi.org/10.1002/jgrb.50087

Martí, J., Villasenor, A., Geyer, A., López, C., & Tryggvason, A. (2017). Stress barriers controlling lateral migration of magma revealed by seismic tomography. *Scientific Reports*, *7*(1), 40757. https://doi.org/10.1038/srep40757

McNutt, S. R. (1996). Seismic monitoring and eruption forecasting of volcanoes: a review of the state-of-the-art and case histories. In *Monitoring and mitigation of volcano hazards* (pp. 99–146). Berlin, Heidelberg: Springer.

Meier, U., Shapiro, N. M., & Brenguier, F. (2010). Detecting seasonal variations in seismic velocities within Los Angeles basin from correlations of ambient seismic noise. *Geophysical Journal International*. https://doi.org/10.1111/j.1365-246X.2010.04550.x

Meletlidis, S., Di Roberto, A., Cerdeña, I. D., Pompilio, M., García-Cañada, L., Bertagnini, A., et al. (2015). New insight into the 2011–2012 unrest and eruption of El Hierro Island (Canary Islands) based on integrated geophysical, geodetical and petrological data. *Annals of Geophysics*, *58*(5), S0546. https://doi.org/10.4401/ag-6754

Obermann, A., Froment, B., Campillo, M., Larose, E., Planès, T., Valette, B., et al. (2014). Seismic noise correlations to image structural and mechanical changes associated with the Mw7.9 2008 Wenchuan earthquake. *Journal of Geophysical Research: Solid Earth*, *119*, 3155–3168. https://doi.org/10.1002/2013JB010932

Obermann, A., Planès, T., Larose, E., & Campillo, M. (2013). Imaging preeruptive and coeruptive structural and mechanical changes of a volcano with ambient seismic noise. *Journal of Geophysical Research: Solid Earth*, *118*, 6285–6294. https://doi.org/10.1002/2013jb010399

Obermann, A., Planès, T., Larose, E., Sens-Schönfelder, C., & Campillo, M. (2013). Depth sensitivity of seismic coda waves to velocity perturbations in an elastic heterogeneous medium. *Geophysical Journal International*, *194*(1), 372–382. https://doi.org/10.1093/gji/ggt043

Paasschens, J. C. J. (1997). Solution of the time-dependent Boltzmann equation. *Physical Review E*, *56*(1), 1135–1141. https://doi.org/10.1103/PhysRevE.56.1135

Pacheco, C., & Snieder, R. (2005). Time-lapse travel time change of multiply scattered acoustic waves. *The Journal of the Acoustical Society of America*, *118*(3), 1300–1310. https://doi.org/10.1121/1.2000827

Peng, Y., & Rubin, A. M. (2016). High-resolution images of tremor migrations beneath the Olympic Peninsula from stacked array of arrays seismic data. *Geochemistry, Geophysics, Geosystems*, *17*, 587–601. https://doi.org/10.1002/2015GC006141

Planès, T., Larose, E., Margerin, L., Rossetto, V., & Sens-Schönfelder, C. (2014). Decorrelation and phase-shift of coda waves induced by local changes: Multiple scattering approach and numerical validation. *Waves in Random and Complex Media*, *24*(2), 99–125. https://doi.org/10.1080/17455030.2014.880821

Prudencio, J., Del Pezzo, E., García-Yeguas, A., & Ibáñez, J. M. (2013). Spatial distribution of intrinsic and scattering seismic attenuation in active volcanic islands, I: Model and the case of Tenerife Island. *Geophysical Journal International*, *195*(3), 1942–1956. https://doi.org/10.1093/gji/ggt361

Roman, D. C. (2017). Automated detection and characterization of harmonic tremor in continuous seismic data. *Geophysical Research Letters*, *44*, 6065–6073. https://doi.org/10.1002/2017gl073715

Romero, P., & Schimmel, M. (2018). Mapping the basement of the Ebro Basin in Spain with seismic ambient noise autocorrelations. *Journal of Geophysical Research: Solid Earth*, *123*, 5052–5067. https://doi.org/10.1029/2018jb015498

Rosetto, V., Margerin, L., Planès, T., & Larose, E. (2011). Locating a weak change using diffuse waves (LOCADIFF): Theoretical approach and inversion procedure. *Journal of Applied Physics*, *109*, 034903. https://doi.org/10.1063/1.3544503

Sato, H. (1993). Energy transportation in one- and two-dimensional scattering media-analytic solutions of the multiple isotropic scattering model. *Geophysical Journal International*, *112*(1), 141–146. https://doi.org/10.1111/j.1365-246X.1993.tb01443.x

Schimmel, M. (1999). Phase cross correlations: Design, comparisons, and applications. *Bulletin of the Seismological Society of America*, *89*(5), 1366–1378.

Schimmel, M., Stutzmann, E., & Gallart, J. (2011). Using instantaneous phase coherence for signal extraction from ambient noise data at a local to a global scale. *Geophysical Journal International*, *184*(1), 494–506. https://doi.org/10.1111/j.1365-246X.2010.04861.x

Schimmel, M., Stutzmann, E., & Ventosa, S. (2018). Low-frequency ambient noise autocorrelations: Waveforms and Normal modes. *Seismological Research Letters*, *89*, 1488–1496. https://doi.org/10.1785/0220180027

Shang, T., & Gao, L. (1988). Transportation theory of multiple scattering and its application to seismic coda waves of impulsive source. *Scientia Sinica*, *31*, 1503–1514.

Takano, T., Nishimura, T., & Nakahara, H. (2017). Seismic velocity changes concentrated at the shallow structure as inferred from correlation analyses of ambient noise during volcano deformation at Izu-Oshima, Japan. *Journal of Geophysical Research: Solid Earth*, *122*, 6721–6736. https://doi.org/10.1002/2017JB014340

Tarantola, A., & Valette, B. (1982). Generalized non-linear inverse problems solved using the least-squares criterion. *Reviews of Geophysics*, *20*(2), 219–232.

Tárraga, M., Martí, J., Abella, R., Carniel, R., & López, C. (2014). Volcanic tremors: Good indicators of change in plumbing systems during volcanic eruptions. *Journal of Volcanology and Geothermal Research*, *273*, 33–40. https://doi.org/10.1016/j.jvolgeores.2014.01.003

Telesca, L., Lovallo, M., López, C., & Marti Molist, J. (2016). Multiparametric statistical investigation of seismicity occurred at El Hierro (Canary Islands) from 2011 to 2014. *Tectonophysics*, *672-673*, 121–128. https://doi.org/10.1016/j.tecto.2016.01.045

Zhan, Z., Tsai, V. C., & Clayton, R. W. (2013). Spurious velocity changes caused by temporal variations in ambient noise frequency content. *Geophysical Journal International*, *194*(3), 1574–1581. https://doi.org/10.1093/gji/ggt170

B. Sánchez-Pastor, P., Obermann, A., Schimmel, M., Weemstra, C., Verdel, A. & Jousset, P. (2019). Detecting and locating precursory signals during the 2011 El Hierro, Canary Islands, submarine eruption. *Geophysical Research Letters*. https://doi.org/10.1029/2019GL082352. Accepted

Sánchez-Pastor Pilar (Orcid ID: 0000-0002-1163-5488)
Schimmel Martin (Orcid ID: 0000-0003-2601-4462)
Weemstra Cornelis (Orcid ID: 0000-0003-3509-8354)
Jousset Philippe (Orcid ID: 0000-0002-5628-0238)

Short- and long- term variations in the Reykjanes geothermal reservoir from seismic noise interferometry

Pilar Sánchez-Pastor[1,2], Anne Obermann[3], Martin Schimmel[1], Cornelis Weemstra[4,5], Arie Verdel[6], Philippe Jousset[7]

[1] Institute of Earth Sciences Jaume Almera - CSIC, Barcelona, Spain

[2] Departament de Dinàmica de la Terra i de l'Oceà, Universitat de Barcelona, Barcelona, Spain

[3] Swiss Seismological Service, ETH Zurich, Zurich, Switzerland

[4] Department of Geoscience and Engineering, Delft University of Technology, Delft, The Netherlands

[5] Department of Seismology & Acoustics, Royal Netherlands Meteorological Institute, De Bilt, The Netherlands

[6] Netherlands Organisation for Applied Scientific Research TNO, Utrecht, The Netherlands

[7] GFZ German Research Centre for Geosciences, Telegrafenberg, Potsdam, Germany

Corresponding author: Pilar Sánchez-Pastor (psanchezsp@gmail.com)

Key Points:

- Identification of three elastic properties changes in time-frequency associated with abrupt injection and production rate variations
- Water deficit in the reservoir leads to a gradual seismic velocity decrease
- Seasonal production-rate variations within the geothermal reservoir are observed as structural property changes

This article has been accepted for publication and undergone full peer review but has not been through the copyediting, typesetting, pagination and proofreading process which may lead to differences between this version and the Version of Record. Please cite this article as doi: 10.1029/2019GL082352

Abstract

The Reykjanes Geothermal System (RGS) is a high-temperature geothermal system located on the Reykjanes peninsula, a trans-tensional plate-boundary zone located on the southwestern tip of Iceland. The area is characterized by high seismicity, recent volcanism and high-temperature geothermal fields. We use seismic noise records from April 2014 to August 2015 to study stress changes and potential deformation of the subsurface caused by injection and production operations at RGS through seismic interferometry. We retrieve continuous time series of waveform similarity values and seismic velocity changes during this period. The S-transform of the similarity values allows us to clearly identify three variations in the mechanical properties of the Reykjanes peninsula related to rapid changes of RGS production. In addition, we observe a slow seismic velocity decrease of 0.36%/year in the reservoir due to the water deficit and seasonal variations associated with the energy production demand.

Plain Language Summary

The Mid-Atlantic Spreading Ridge divides the Reykjanes peninsula into two tectonic plates and causes the high volcanic activity that characterizes the area. The Reykjanes Geothermal System is one of the five high-temperature geothermal systems exploited in this peninsula. The energy production of RGS has been increasing, causing drastic changes in reservoir conditions, such as, a man-made subsidence of around 10 cm in the area. We employ three current methodologies to monitor changes of mechanical and structural properties in the subsurface, using 1.5 years of continuous seismic records. We identify and locate three short- term variations associated with abrupt injection and production rate changes in RGS. In addition, we observe a slow seismic velocity decrease due to the long-term water extraction, as well as variations associated with demand-driven seasonal fluctuations in the extraction rates

1. Introduction

Despite the fact that early foundations have been laid in the fifties and sixties by seismologists such as Aki (1957) and Claerbout (1968), seismic interferometry (SI) gained most of its popularity over the last decade. SI refers to the principle of generating virtual-source responses by cross-correlating existing seismic records (Bakulin & Calvert, 2006). Many applications have arisen that exploit the technique to infer characteristics of the subsurface (e.g., Draganov et at., 2007; Shapiro et al., 2005; Sens-Schönfelder and Wegler, 2011); the sun (Duvall et al., 1993), the oceans (Roux and Fink, 2003; Woolfe et al., 2015), buildings (Snieder and Safak, 2006; Kohler et al., 2007), and the atmosphere (Haney, 2009, Fricke et al., 2014).

An important application of SI involves the monitoring of tiny changes of elastic and structural properties in a medium that can be picked up as waveform dilatations or distortions in the so called ‘coda’; later-arriving multiply scattered waves (e.g., Sens-Schönfelder and Wegler, 2006; Beroza et al., 1995). The coda-waves sample the medium very densely and are more sensitive to mechanical and structural changes than the direct arrivals. The technique is often referred to as coda-wave interferometry (CWI, Snieder et al., 2002).

The ever-present ambient vibrations enable a continuous retrieval of virtual-source responses and therefore remove the need for expensive and disturbing repetitive controlled sources. The continuous nature of the virtual-source responses also implies that these do not suffer from a lack of repeatability, in contrast to the responses obtained from natural sources, such as earthquakes (e.g. Poupinet et al., 1984). The main condition required for monitoring is that the ambient vibrations are statistically robust over certain time windows. This permits repeatable virtual-source responses, which then allow for structural changes to be studied. Due to this characteristic, the condition that the medium is illuminated uniformly from all angles, which is a requirement for accurate Green’s function retrieval (Tsai, 2009; Weaver et al., 2009), can be relaxed for monitoring purposes (Hadziioannou et al., 2009).

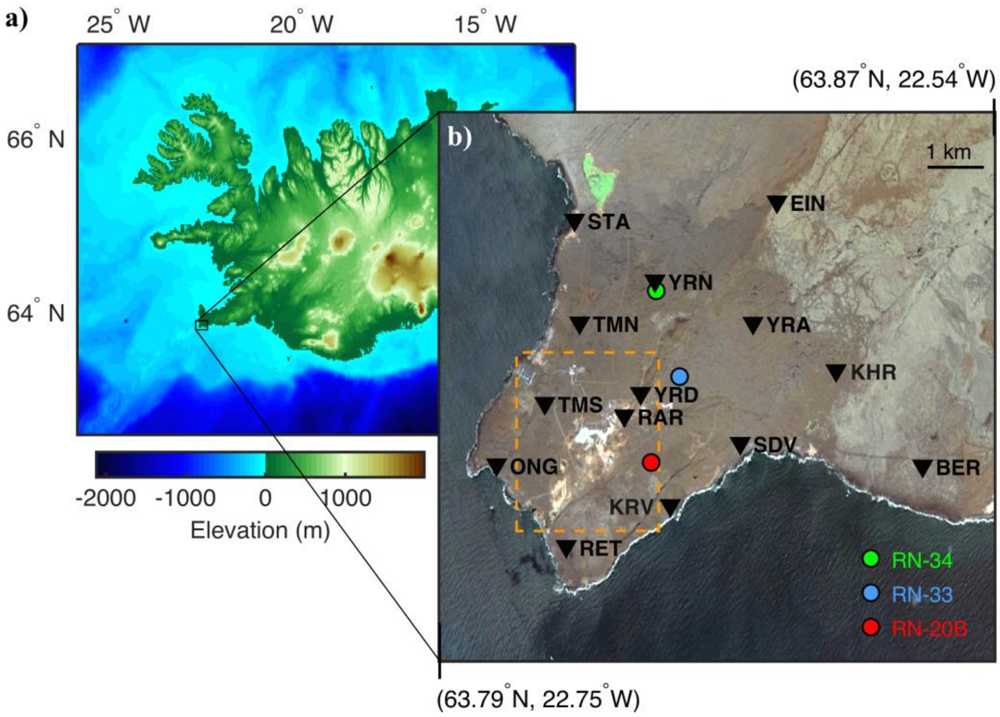

Figure 1. (a) Location and elevation map of Iceland. The black box marks the Reykjanes peninsula. (b) Map of the tip of the Reykjanes peninsula. The black triangles indicate the seismic stations used in this study. The circles show the location of three injection wells: RN-20B (red), RN-33 (blue), and RN-34 (green). The approximate location of the production area of the RGS is represented by the dashed orange square.

Seismic monitoring using coda-wave interferometry has been applied successfully on various scales (e.g., Stähler et al., 2011; Obermann et al., 2014) and in a variety of environments (Sens-Schönfelder and Wegler, 2011). Recently, the use of SI in a geothermal context has received considerable attention. In 2017, the cumulative global geothermal capacity reached over 14 GW; this figure is expected to rise to over 17 GW by 2023 (International Energy Agency (IEA), 2018, Hirschberg et al., 2015). Geothermal systems can be divided into 'hydrothermal systems', which exploit existent and naturally profitable aquifers and 'enhanced geothermal systems' (EGS) which enhance the permeability of the crystalline basement through high-pressure injection of fluids. To our knowledge, SI has only been used to probe EGSs (Hillers et al., 2015; Lehujeur et al., 2015; Obermann et al., 2015).

The Reykjanes geothermal system (RGS) is a hydrothermal system located on the southwestern tip of the Reykjanes peninsula, where the Mid-Atlantic ridge comes ashore. This system has been exploited on a small scale for decades, but in 2006 a new power plant was installed. The associated increased production rate has caused drastic changes in reservoir conditions, for instance, a considerable drop of the pressure in the reservoir (Axelsson et al., 2015) and a subsidence of around 10 cm in the area (Keiding et al., 2010).

In this study, we assess the capability of SI to detect tiny mechanical and structural changes in RGS using ambient-seismic noise recorded by thirteen stations from April 2014 till August 2015 (Figure 1). During this period, the geothermal activity of the power plant was uninterrupted in different points of the peninsula. The lack of seismic records during a 'calm period' causes a strong variability of the seismic medium response. Thus, we focus on the waveform similarity evolution (D'Hour et al., 2015; Sánchez-Pastor et al., 2018) and lapse-time changes in velocity (e.g. Brenguier et al., 2011; Hadziioannou et al., 2009; Obermann et al., 2014) using different methods to ascertain the robustness of our findings. We propose a new procedure to discriminate potential changes in time and frequency of such evolution curves through the computation of the S-transform (Stockwell et al., 1996).

2. Geothermal well operations

The Mid-Atlantic Spreading Ridge divides the Reykjanes peninsula into two tectonic plates that part at an average of 2 cm/yr. The trans-tensional plate boundary causes significant seismic and volcanic activity with NE-SW striking faults and fissures characterizing the area. The active volcanic systems derive their energy from cooling magma bodies in the crust, such as magma chambers, dykes and other intrusions (Flóvenz et al., 2015; Gudmundsson, 1995; Gudmundsson & Thórhallsson, 1986). These important heat sources reach the surface and have been exploited since the settlement of Iceland in the 9th century. Nowadays, the utilization of the geothermal sources plays a fundamental role in the energy economy of Iceland (Ragnarsson, 2013).

On Reykjanes peninsula, five high-temperature geothermal systems are exploited; RGS is one of them. The development of this system started in 1956 with a single shallow well (~160m). RGS expanded through the development of 14 deep production wells (around 2 km depth) and the construction of a geothermal plant of 100 MW in 2006 (Axelsson et al., 2015). In order to counteract the pressure drop in the reservoir and reduce the environmental effects of surface disposal, in 2009 the re-injection of sea-water into the system began (Flóvenz et al., 2015). During the time period evaluated in this study, only one injection well was operating at 1.2 km of depth (RN-20B) and two were running for tracer tests (RN-33, RN-34) at around 2 km depth (Figure 1). The extracted-water volume is shown in Figure 2a together with the injected-water volume of the three injection wells. The seismicity of the area does not show a direct correlation with the observed injection/production changes (supporting information Figure S4).

3. Data and seismic interferometry

3.1 Seismic network

We use thirteen stations from the Reykjanes seismic array (RARR) (Blanck et al., 2016; Weemstra et al., 2016) most of which were deployed in the context of the European Community's project IMAGE (Integrated Methods for Advanced Geothermal Exploration) from the beginning of April 2014 until August 2015 at the tip of the Reykjanes peninsula (Figure 1). The selected stations (Figure 1b) have been recording quasi-continuously for the 1.5 years of observation period at 100 samples/s. In the supporting information (Figure S1), we show the exemplary power spectrum density plots for the different types of sensors.

3.2 Computation of auto- and cross-correlations

We compute auto- and cross-correlations using the vertical component of all seismic stations. For the computation of the correlations, we use the classical correlation approach (CC, Bensen et al., 2007) and the phase cross-correlation (PCC; Schimmel, 1999). One-bit amplitude normalization and spectral whitening are commonly used as pre-processing for the classical approach to reduce its amplitude bias caused by seismicity and other energetic signals (Bensen et al., 2007). Here, we compute geometrically normalized CCs, with (CCN) and without (CCG) such pre-processing. It is useful to note that the PCC is not affected by large amplitudes and does not require any pre-processing that could yield a loss of information in terms of waveform distortion (Schimmel et al., 2011; Schimmel et al., 2018). PCC has been successfully employed in other noise-based monitoring and imaging studies (e.g. D'Hour et al., 2015; Romero and Schimmel, 2018; Sánchez-Pastor et al., 2018).

Restricting the frequency band of the correlations, the convergence of the virtual-source response improves significantly (Roux et al., 2005). We therefore compare the waveform convergence of the three above-mentioned approaches (CCN, CCG, PCC) in three different frequency bands (0.1-1.0 Hz, 0.5-2.0 Hz, 2.0-5.0 Hz). This comparison is made separately for different interstation distances (supporting information Figure S2). Since most of the changes in injection and production rate in the RGS happen over a very short period of time, fast convergence of the stabilization of the correlations is important. Irrespective of the method, the shorter the interstation distance and/or the lower the frequency, the faster the convergence. With higher frequency, pre-processing (CCN) results in a slower convergence compared to PCC and CCG.

Therefore, we primarily focus on the frequency band 0.1 – 1.0 Hz, and stack correlations from 72 hours of seismic recordings for a stable convergence. The method employed will be PCC, because it is more sensitive to waveform changes (Schimmel et al., 1999) and the convergence of the three methods is similar for this frequency band (Figure S2).

3.3 Determination of time-lapse changes

With ongoing production over a large area and various injection wells in the RGS, it is challenging to identify time-lapse changes in the coda associated with well operations. To ensure that our results are unbiased by the choice of the reference function, we use all three methods that are currently discussed in the literature to detect lapse-time changes: time evolution of waveform similarity (e.g. D'Hour et al., 2015; Sánchez-Pastor et al., 2018), stretching method (e.g. Brenguier et al., 2011; Hadziioannou et al., 2011; Obermann et al., 2014) and a generalized formulation of the MWCS (Brenguier et al., 2014; Gómez-García et al., 2018). The first two methods require a noise response reference of the medium to quantify changes, which is calculated by stacking days with the highest production rate (excluding the days 210-300/2014).

We selected three station couples to study coda time-lapse changes detected with the above-mentioned methods (Figure 2): RAR-RET that crosses the production area, KRV-RAR crossing the injection well RN-20B and YRN which is the closest station to the tracer-test well RN-34.

3.3.1 Waveform similarity

Changes in waveform similarity may be due to structural changes in the medium due to variations of scattering properties (e.g., altered seismic discontinuities, fracturing). To detect such distortions, we compute the waveform similarity (D'Hour et al., 2015; Sánchez-Pastor et al., 2018) between the reference and daily responses in various lag time windows of 6s length (Figure 2b). The most prominent feature is a sinusoidal variation, which finds its maximum in January and minimum in mid-July and appears between 4 and 16 seconds of lag time. The production rate also follows this low-frequency variation (Figure 2a, black line).

Besides this long-term feature, we observe short-term fluctuations that are consistent over a broad range of lag-times. While many of these fluctuations cannot be related to RGS activity, climatological data

or seismicity, we highlight three similarity changes (Figure 2b, grey shadowed rectangles and labelled I, II and III), which are accompanying the largest changes in production/injection. The changes can be seen up to 6, 8 and 14 seconds of lag time respectively in the three station couples.

3.3.2 Waveform stretching

Mechanical changes in the medium typically produce a time-shift in the later-arriving waves, when compared with a reference (e.g. Brenguier et al., 2011; Hadziioannou et al., 2009; Obermann et al., 2014). In Figure 2c, we show the velocity variation results averaged between 10 and 50 seconds of lag time. The evolution of the correlation coefficient also shows the large sinusoidal trend commented on in the previous section. We can also observe the local perturbations (I, II and III) in all three station couples, although less clearly than from the waveform similarity analysis.

The correlation coefficient is around 0.8 and the observed velocity fluctuations are quite large. The stretching technique requires high coherence between reference and daily traces, which is not achieved in this study due to the strong variability of the seismic medium response. This coherence can be increased stacking more days for comparison and/or using a larger time-shift in the coda. However, as we expect tiny changes that happen only over short periods of time, we prefer to keep our choice of parameters and remain aware of the ambiguity in the absolute values of the velocity variations.

3.3.3 Generalized MWCS formulation

The MWCS technique quantifies the velocity variation of the medium by a linear adjustment of the time-shift using several consecutive lag-time windows in the frequency domain (Clarke et al., 2011). This approach assumes a homogenously distributed velocity change, contrary to classical stretching that allows to determine the lag-time dependent effect of localized changes (Obermann, Planès, Larose, & Campillo, 2013; Obermann et al., 2016; 2018).

Brenguier et al (2014) generalized the MWCS technique to be independent of a reference function. The changes are retrieved comparing the velocity estimates from MWCS between all possible combinations of days. The characteristic correlation length (β) controls the distance between days to be correlated. Thus, we can obtain long- and short- time variations of the velocity change time series. We employ this method for β: 5, 10^3 and 10^4 and the results obtained are shown in Figure 2d. As with the previous methods, the low frequency sinusoidal tendency is clearly visible in all station couples. Moreover, a gradual negative trend is observed in the velocity variations. The small perturbations are more complicated to distinguish from others although the decrease in injection rate (I) is observed in KRV-RAR and YRN-YRN, the production volume change II in RAR-RET and KRV-RAR, and change III can be seen in all three couples. The uncertainties of the velocity change estimates for β=5 are around 0.05%, which are small in comparison to the velocity changes analysed.

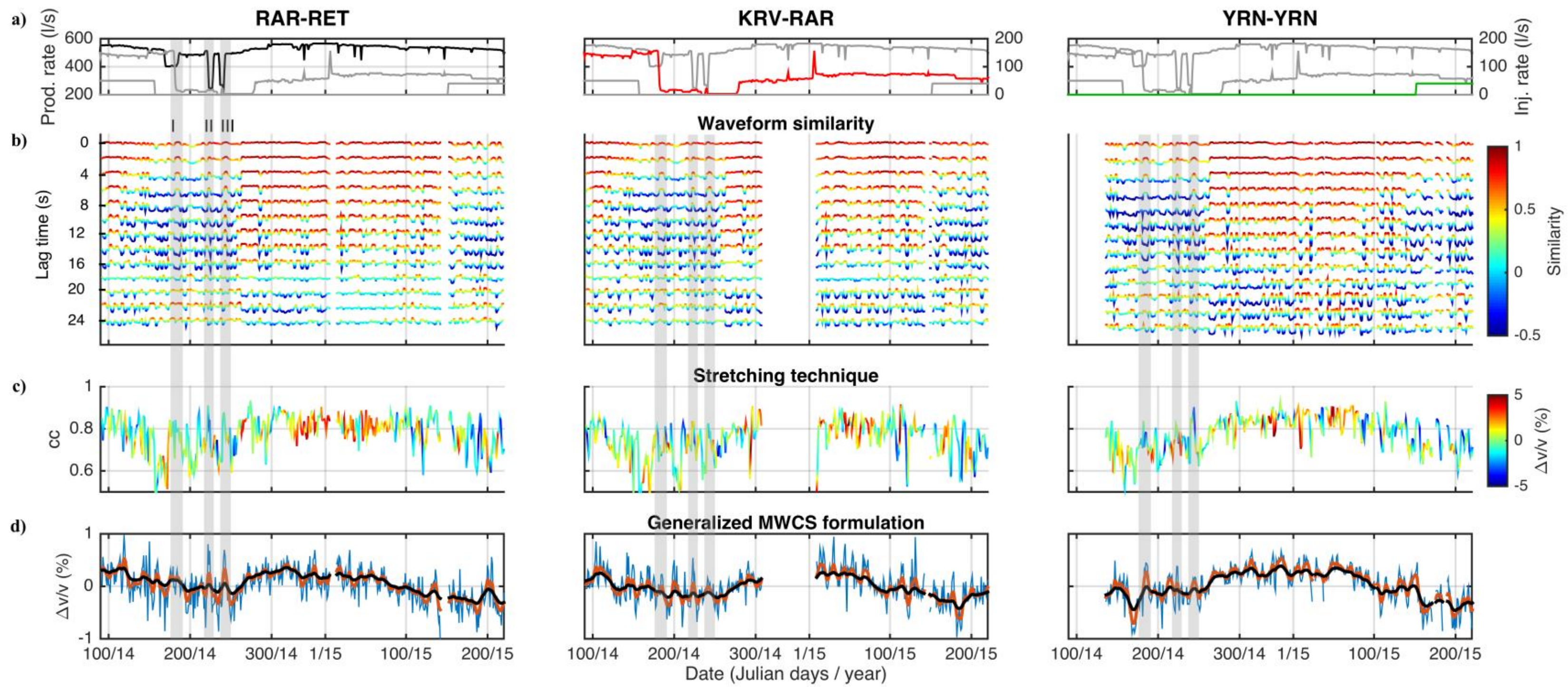

Figure 2. Results of the three different methodologies employed for the frequency band (0.1 -1) Hz for three station couples: RAR-RET (crossing the production area), KRV-RAR (crossing RN-20B well) and the autocorrelation of YRN (close to RN-34). (a) Production and injection rates of RGS are represented in grey highlighting the closest-well rate following the colors of Figure 1 and the production rate in black. (b) Averaged waveform similarity values for negative and positive lag-time windows of 6 seconds length. (c) Correlation coefficients obtained from the stretching technique, the color scale represents the computed velocity change. (d) Velocity changes computed by MWCS technique for three correlation lengths, β=5 (blue), 10^3 (orange) and 10^4 (black). Grey shading indicates the three fluctuations of interest (I, II and III).

4. Discussion

4.1 Time-frequency analysis

The time-evolution of the waveform similarity and of velocity variations gives us an idea of the influence of the operations at the RGS on the surrounding area. Due to the lack of records prior to the well operations and also the complexity of the system, such time-evolutions (in particular the seismic velocity variations) contain various fluctuations that are difficult to relate directly to natural or artificial processes.

In the following, we focus on the largest rate-variations of the power plant (I, II and III) and see if we can work out the time-lag changes more clearly by decomposing the similarity curves in the time-frequency domain through the S-transform (Stockwell et al., 1996)

$$S(\tau, f) = \int_{-\infty}^{+\infty} s(t) w(\tau - t, f) e^{i2\pi f t} dt. \quad (1)$$

s(t) is the waveform similarity curve at a specific lag time window, $w(\tau - t, f)$ is a Gaussian function centred at time τ and width proportional to 1/f. The S-transform is based on the Fourier theory and related to the wavelet transform through a matrix multiplication (Ventosa et al. 2008; Schimmel et al., 2011).

We perform the S-transform for the 1.5 years for all station couples, splitting them into two groups (crossing and not crossing the production area) to differentiate and analyze the observed waveform changes (Figure 3). Considering that the sample rate of the similarity time series is one day, the Nyquist frequency corresponds to 0.5 days^{-1}. On the other hand, the resolution at low frequencies is expected to be poor since the records are only 1.5 years long. The three changes in similarity are more prominent for the station couples that cross the production area. On the contrary, for stations outside this area the similarity changes are smaller and show more variability (Figure 3b). In Figure 3c, such fluctuations emerge around 0.5 days^{-1}. Below $6 \cdot 10^{-3}$ days^{-1}, we can observe the long seasonal variation that we discussed in section 3.3 in both station groups, although it is more intense for the couples closer to the production area.

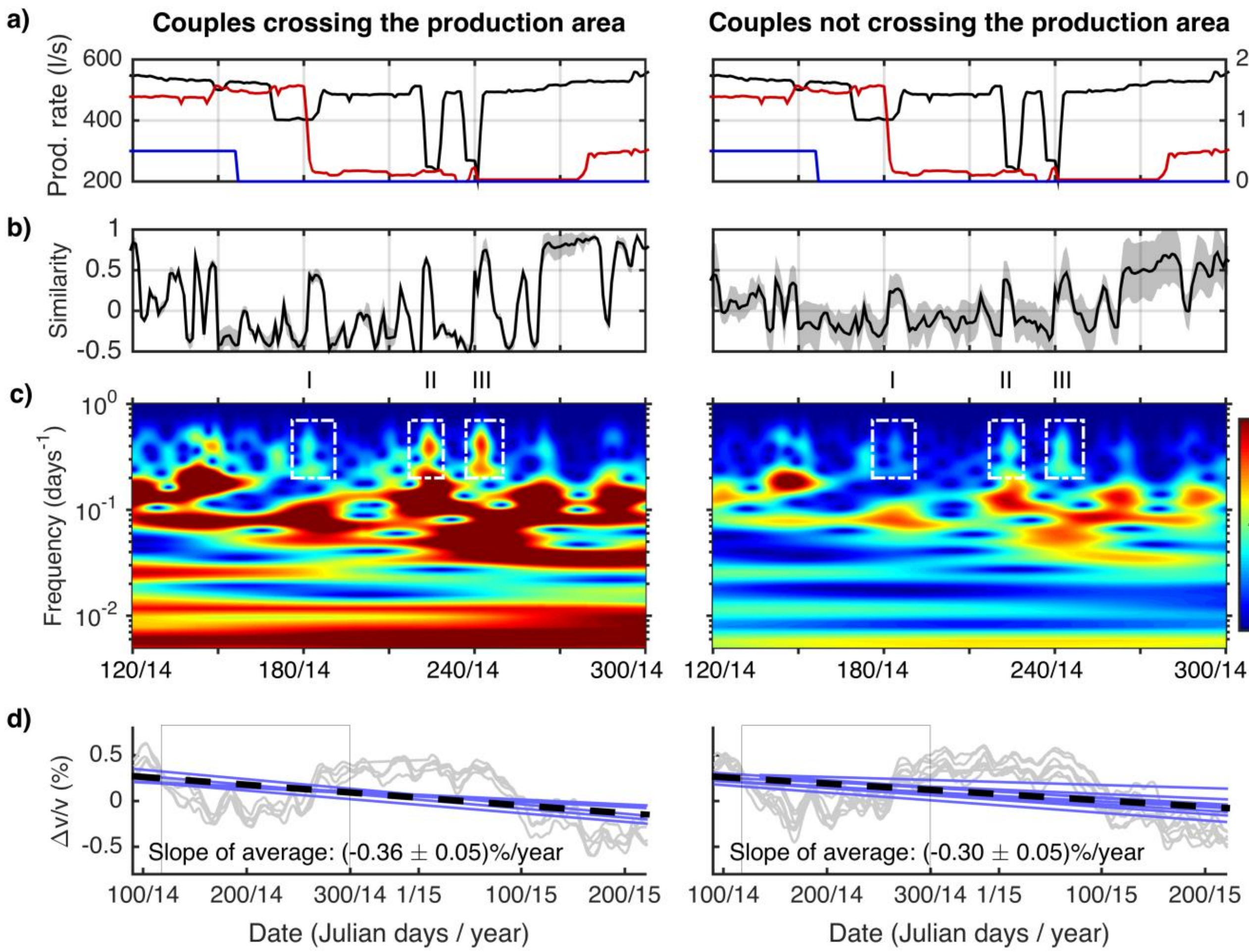

Figure 3. (a) Production and injection rate of RGS. The colors are the same as on Figure 2a. (b) Average of similarity values of station couples that cross (left) and do not cross (right) the production area at 6 seconds lag time. Standard deviation is shown as gray shading. (c) Time-frequency amplitude spectra of the above similarity curves. The white boxes highlight the fluctuations I, II and III. (d) Velocity variations measured using the generalized MWCS formulation for $\beta=10^4$ (grey lines) of auto-correlations for the 1.5 years of study. The blue lines represent their linear regressions of every curve and the dashed-black line the linear regression of the velocity variation average of the station group. The grey box marks the period of time of the upper panels.

4.2 Spatial distribution of the changes

Comparing the results between the two station groups of Figure 3, we expect the biggest structural changes within the production area. For verification and further details, we also compute the spatial distribution of the scattering cross-sections associated with the structural changes (I, II, III and seasonal) based on probabilistic sensitivity kernels (e.g., Larose et al., 2010; Obermann, Planès, Larose, Sens-Schönfelder, et al., 2013; Pacheco & Snieder, 2005). We assume surface waves dominance and use the solution of the 2D radiative transfer equation to build sensitivity kernels (Paasschens, 1997; Sato, 1993; Shang & Gao, 1988) and a scattering mean free path of 30 km. These sensitivity kernels (K), the observed similarity changes (DC) and their scattering cross-sections (σ) are related according to the following formula:

$$DC = \frac{c\sigma}{2} K, \qquad (2)$$

where c is the effective wave speed that we fix at 3km/s. We obtain the scattering cross-sections from eq. 2 by using the minimum square inversion method for linear problems (Tarantola and Valette, 1982). Since the three similarity peaks are in the seasonal variation minimum, the decorrelation is quantified as the similarity amplitude of such days whereas the seasonal change is computed as the difference between the averaged similarity in summer and winter.

Figure 4 shows the inversion results for the four similarity changes under study. Consistently, the larger the similarity change, the larger the observed scattering cross-section. All structural changes, including the seasonal changes, are located around the production area and vanish with distance. In general, the values are smaller than in other studies, where volcanic eruption volumes (Obermann, Planès, Larose, Sens-Schönfelder, et al., 2013; Sánchez-Pastor et al., 2018), or 10^5 liters of injection were studied (Hillers et al. 2015). For comparison, we compute the inversion during the 'calmest' days 200-210 (2014), when the production rate remains constant with fluid injection almost zero (Figure 4d).

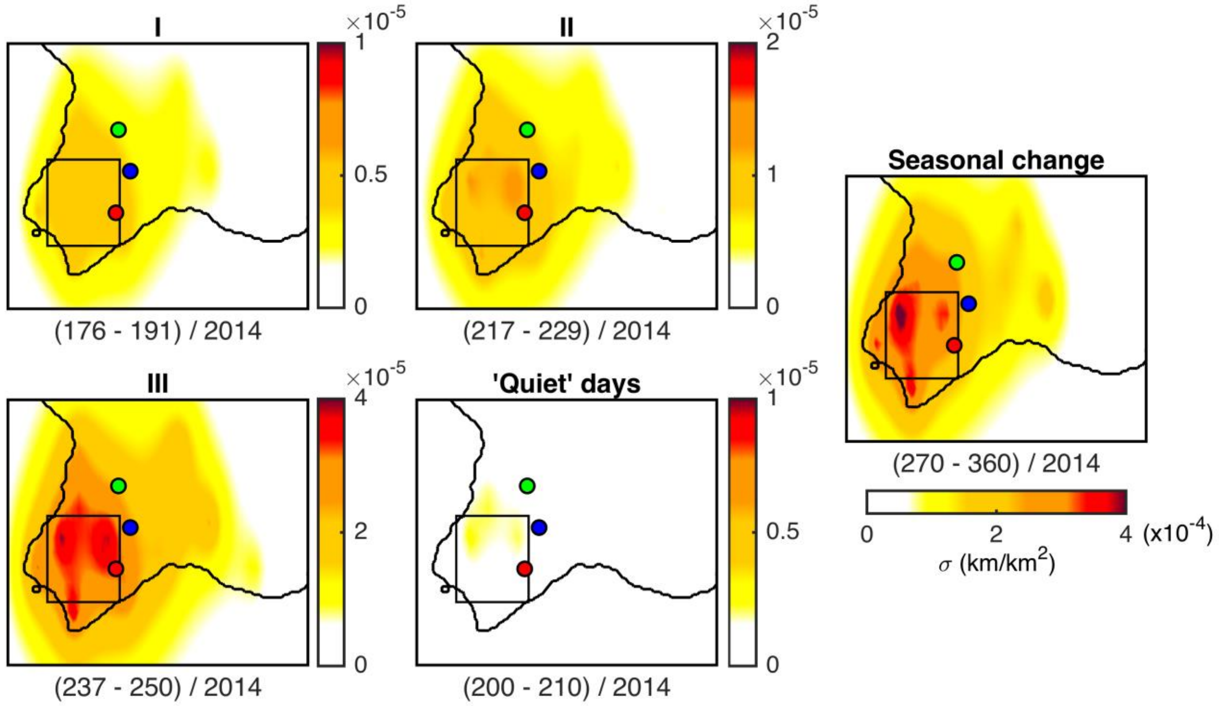

Figure 4. Scattering cross-section density maps at 6s lag time for (a, b, c) the three highlighted periods in Figure 3 (I, II, III), (d) an example of calmest days and (e) the seasonal change.

4.3 Short- and long- term effects of RGS

The short-term subsurface effects of the exploitation of the RGS are associated with sharp variations of water injection volume and energy production. These rapid fluctuations change the state of stress abruptly and distort wave propagation, which can be observed by SI. In the Reykjanes peninsula for frequencies of (0.1 – 1)Hz, the seismic velocity of surface waves is roughly 1.2 km/s (Jousset et al, 2016). The probed depth should therefore range between 0.5 and 12 km. The similarity change I, which is related to the largest injection-rate drop of RN-20B, appears at earlier lag times than the others. The associated structural changes are therefore shallower than those caused by production-rate drops, which affect likely a deeper and wider zone of the surrounding medium. The changes are expected to be constrained to the first few kilometres of the crust. This corresponds to the approximate depth of water injection into the rock mass.

In monitoring studies with long seismic records, seasonal variations are typically observed (e.g. Gomez-García et al., 2018; Sens-Schönfelder & Wegler, 2006) and typically related to seasonal variations of the ocean noise directivity (Juretzek & Hadziioannou, 2016; Stutzmann et al., 2009), which affect the ballistic waves of the cross-correlations (e.g. Froment et al., 2010; Hadziioannou et al., 2011). However, the effects of the seasonal variations are expected to be mostly homogeneous since the study area is very small. Nevertheless, we observe a more intense seasonal variation near the power plant (Figure 3c,4e). The production rate varies depending on the power demand of the Icelandic population, and that is highest in winter and decreases during summer (Figure 3a). Indeed, the Pearson coefficient between the similarity curve at 6s lag time and the smoothed production rate (without the abrupt changes) is estimated as 0.84 (supporting information Figure S3). Looking at days 120 (2014), 264 (2014) and 155 (2015), the similarity values suffer a sign-switch too abrupt to come from a noise-source distribution change and do not coincide with any production rate drop (Figure 2a, 2b). We are however inclined to believe that the production rate variations directly influence the subsurface and may be therefore in phase and overlap the variation due to changing noise sources (Figure 2). A possible interpretation is that the medium exhibits a production rate threshold, here estimated at about 520 l/s (Figure 2a). Once the production volume passes this tolerance threshold, the elastic properties of the medium change significantly. This threshold could be related to the permeability of the rock mass, which depends exponentially on the exposition time to hot water flows (Summers et al., 1978) and affects the pore pressure of the rocks (David et al., 1994).

Another long-term effect in the Reykjanes reservoir is the negative trend of the velocity variation time series (Figure 2d). As auto-correlations are more sensitive to local changes in the subsurface and probe larger depths (e.g. D'Hour et al., 2015; Sánchez-Pastor et al., 2018), we compute linear regressions of the velocity variations from the generalized MWCS formulation of all auto-correlations within and outside the production area (Figure 3d). All auto-correlations show this particular velocity decrease being slightly stronger for the station couples that cross the production area. The slope of the velocity variation average represents a regional velocity decrease rate of 0.36%/year in the production area and 0.3%/year outside. Since the water volume injected is less than the extracted volume (Figure 2a), there is a water loss which is partially compensated by natural recharge into the system (Keiding et al., 2010). However, the consequent long-term decrease in pore pressure causes a contraction of the rock matrix and man-made subsidence of the peninsula (Keiding et al., 2010). This subsidence carries a density increase of rocks yielding the observed velocity decrease. The water deficit can play a further role in the observed seismic velocity, which decreases in high-porosity pyroclastic rocks as a function of water content (e.g Kahraman et al., 2017). Note that the system seems to respond differently for short and long time-scales; whereas the velocity variations increase for abrupt decreases in water extraction, those variations decrease over a timescale of years due to the water deficit. However, here we did not further analyse the physical processes which cause this different behaviour.

5. Conclusions

The time evolution pattern of similarity and velocity changes has a rich frequency content that points to different time scale effects in the Reykjanes reservoir. We decompose the similarity time series into the time-frequency domain through the S-transform, allowing us to clearly discriminate three fluctuations associated to injection and production rate drops. The lack of seismic records during a calm period causes a strong variability of noise response reference of the medium. In these conditions, the reference unbiased MWCS analysis shows a great advantage compared to the classical stretching method. There are many fluctuations in the time series that do not match with the timing of water injection and production volume variations and could be caused by conduit collapses, water saturation or diverse instabilities in the medium. In the long term, the power plant subsurface shows a seasonal variation that might be associated with the energy demand. Furthermore, the increasing water deficit of this hydrothermal system produces a slow velocity decrease of 0.36%/year in the surrounding medium.

Acknowledgments

We warmly thank Ómar Sigurðsson from HS Orka (the owner of Reykjanes Geothermal plant) for furnished the production and injection rate data (https://www.hsorka.is). In addition, we would like to thank Hanna Blanck, Kristján Ágústsson, Gylfi Páll Hersir, all from Iceland GeoSurvey (ÍSOR, http://en.isor.is/), for their help and for providing the data of the stations with the short-period Lennartz sensors (operated on behalf of HS Orka). The climatological data can be requested from https://en.vedur.is/. The research efforts by CW has received funding from the European Community's Seventh Framework Programme under grant agreement No. 608553 (Project IMAGE, http://www.image-fp7.eu). Pilar Sánchez-Pastor acknowledges funding from the Spanish Ministry of Economy and Competitiveness (project MISTERIOS, CGL2013-48601-C2-1-R). We also thank the Editor Rebecca Carey and the two reviewers Gerrit Olivier and Clare Donaldson for comments that helped improve the manuscript.

6. References

Aki, K. (1957). Space and time spectra of stationary stochastic waves, with special reference to microtremors, *Bulletin of the Earthquake Research Institute*, 35, 415–457. doi:http://hdl.handle.net/2261/11892.

Axelsson, G., Arnaldsson, A., Berthet, J.-c. C., Bromley, C. J., Gudnason, E. Á., Hreinsdóttir, S., Karlsdóttir, R., Magnússon, I. T., Michalczewska, K. L., Sigmunds- son, F. and Sigurdsson, O. (2015). *Renewability Assessment of the Reykjanes Geothermal System, SW-Iceland*. In Proceedings World Geothermal Congress, 10.

Bakulin, A., & Calvert, R. (2006). The virtual source method: Theory and case study. *Geophysics*, 71(4), SI139-SI150. https://doi.org/10.1190/1.2216190

Bensen, G. D., Ritzwoller, M. H., Barmin, M. P., Levshin, A. L., Lin, F., Moschetti, M. P., et al. (2007). Processing seismic ambient noise data to obtain reliable broad-band surface wave dispersion measurements. *Geophysical Journal International*, 169(3), 1239–1260. https://doi.org/10.1111/j.1365-246X.2007.03374.x

Beroza, G. C., Cole, A. T., & Ellsworth, W. L. (1995). Stability of coda wave attenuation during the Loma Prieta, California, earthquake sequence. *Journal of Geophysical Research: Solid Earth*, 100(B3), 3977-3987.

Blanck H., Jousset P., Agustsson, G.P. Hersir & Flovenz, O. G. (2016). *Analysis of seismological data on Reykjanes peninsula, Iceland*. Extended abstract of the European geothermal congress, Strasbourg France.

Brenguier, F., Campillo, M., Takeda, T., Aoki, Y., Shapiro, N. M., Briand, X., Emoto, K. & Miyake, H. (2014). Mapping pressurized volcanic fluids from induced crustal seismic velocity drops, *Science*, 345, 80–82.

Brenguier, F., Clarke, D., Aoki, Y., Shapiro, N. M., Campillo, M. & Ferrazzini, V. (2011). Monitoring volcanoes using seismic noise correlations, *Comptes Rendus Geoscience*, 343, 633–638.

Claerbout, J. (1968). Synthesis of a layered medium from its acoustic transmission response, Geophysics, 33(2), 264–269.

Clarke, D., Zaccarelli, L., Shapiro, N. M., & Brenguier, F. (2011). Assessment of resolution and accuracy of the Moving Window Cross Spectral technique for monitoring crustal temporal variations using ambient seismic noise. *Geophysical Journal International*, 186(2), 867-882.

D'Hour, V., Schimmel, M., Do Nascimento, A. F., Ferreira, J. M., & Lima Neto, H. C. (2015). Detection of subtle hydromechanical medium changes caused by a small-magnitude earthquake swarm in NE Brazil. Pure and Applied Geophysics, 173(4), 1097–1113. https://doi.org/10.1007/s00024-015-1156-0

David, C., Wong, T. F., Zhu, W., & Zhang, J. (1994). Laboratory measurement of compaction-induced permeability change in porous rocks: Implications for the generation and maintenance of pore pressure excess in the crust. *Pure and Applied Geophysics*, 143(1-3), 425-456.

Draganov, D., Wapenaar, K., Mulder, W., Singer, J., & Verdel, A. (2007). Retrieval of reflections from seismic background-noise measurements. *Geophysical Research Letters*, 34(4).

Duvall, T. L., Jefferies, S. M., Harvey, J. W. and Pomerantz, M. A. (1993). Time-distance helioseismology. Nature, 362(6419), 430–432.

Flóvenz, Ó. G., Ágústsson, K., Guðnason, E. A., & Kristjánsdóttir, S. (2015). *Reinjection and Induced Seismicity in Geothermal Fields in Iceland*. Proceedings World Geothermal Congress 2015, Melbourne, Australia

Fricke, J. T., Evers, L. G., Smets, P. S. M., Wapenaar, K. and Simons, D. G. (2014). Infrasonic interferometry applied to microbaroms observed at the Large Aperture Infrasound Array in the Netherlands. *Journal of Geophysical Research: Atmospheres*, 119(16), 9654–9665.

Froment, B., Campillo, M., Roux, P., Gouédard, P., Verdel, A., & Weaver, R. (2010). Estimation of the effect of non-isotropic distributed energy on the apparent arrival time in correlations, *Geophysics*, 75(5), SA85–SA93.

Gómez-García, C., Brenguier, F., Boué, P., Shapiro, N. M., Droznin, D. V., Droznina, S. Ya., et al. (2018). Retrieving robust noise-based seismic velocity changes from sparse data sets: synthetic tests and application to Klyuchevskoy volcanic group (Kamchatka). *Geophysical Journal International*, 214(2), 1218-1236.

Gudmundsson, A. (1995). Ocean-ridge discontinuities in Iceland. *J. Geol. Soc.*, 152:1011–1015.

Gudmundsson, J. and Thórhallsson, S. (1986). The Svartsengi Reservoir in Iceland. Geothermics, 15:3–16.

Hadziioannou, C., Larose, E., Coutant, O., Roux, P. & Campillo, M., (2009). Stability of monitoring weak changes in multiply scattering media with ambient noise correlation: laboratory experiments, *J. acoust. Soc. Am.*, 125(6), 3688–3695.

Hadziioannou, C., Larose, E., Baig, A., Roux, P. & Campillo, M. (2011). Improving temporal resolution in ambient noise monitoring of seismic wave speed, *Journal of Geophysical Research*, 116, B07304, doi:10.1029/2011JB008200.

Haney, M. M. (2009). Infrasonic ambient noise interferometry from correlations of microbaroms. *Geophysical Research Letters*, 36(19), L19808.

Hillers, G., Husen, S., Obermann, A., Planès, T., Larose, E. and Campillo, M. (2015). Noise-based monitoring and imaging of aseismic transient deformation induced by the 2006 Basel reservoir stimulation. *Geophysics*, 80(4), KS51–KS68.

Hirschberg, S., Wiemer, S. & Burgherr, P. (2015). Energy from the Earth, in Deep Geothermal as a Resource for the Future?, edited by S. Hirschberg, S. Wiemer, and P. Burgherr, vdf Hochschulverlag, Zürich., doi:10.3218/3655-8.

International Energy Agency (IEA). Medium-Term Renewable Energy Market Report 2018. Technical report, Paris (2018).

Jousset, P., Blanck, H., Franke, S., Metz, M., Ágústsson, K., Verdel, A., et al. (2016). *Seismic tomography in Reykjanes, SW Iceland*. Paper presented at European Geothermal Congress 2016, Strasbourg, France.

Juretzek, C., & Hadziioannou, C. (2016). Where do ocean microseisms come from? A study of Love-to-Rayleigh wave ratios. *Journal of Geophysical Research: Solid Earth*, 121(9), 6741–6756, doi:10.1002/2016JB013017, 2016JB013017.

Kahraman, S., Fener, M., & Kilic, C. O. (2017). Estimating the Wet-Rock P-Wave Velocity from the Dry-Rock P-Wave Velocity for Pyroclastic Rocks. *Pure and Applied Geophysics*, 174(7), 2621-2629.

Kohler, M. D., Heaton, T. H. and Bradford, S. C. (2007). Propagating Waves in the Steel, Moment-Frame Factor Building Recorded during Earthquakes. *Bulletin of the Seismological Society of America*, 97(4), 1334–1345.

Keiding, M., Arnadóttir, T., Jónsson, S., Decriem, J., & Hooper, A., (2010). Plate boundary deformation and man-made subsidence around geothermal fields on the Reykjanes Peninsula, Iceland. *Journal of Volcanology and Geothermal Research*, 194, 139–149. doi:10.1016/j.jvolgeores.2010.04.011

Larose, E., Planes, T., Rossetto, V., & Margerin, L. (2010). Locating a small change in a multiple scattering environment. *Applied Physics Letters*, 96(20). https://doi.org/10.1063/1.3431269

Lehujeur, M., Vergne, J., Schmittbuhl, J. and Maggi, A. (2015). Characterization of ambient seismic noise near a deep geothermal reservoir and implications for interferometric methods: a case study in northern Alsace, France. Geothermal Energy, 3.

Obermann, A., Froment, B., Campillo, M., Larose, E., Planès, T., Valette, B., et al. (2014). Seismic noise correlations to image structural and mechanical changes associated with the Mw7.9

2008 Wenchuan earthquake. *Journal of Geophysical Research: Solid Earth*, 119, 3155–3168. https://doi.org/10.1002/2013JB010932

Obermann, A., Kraft, T., Larose, E., & Wiemer, S. (2015). Potential of ambient seismic noise techniques to monitor the St. Gallen geothermal site (Switzerland). *Journal of Geophysical Research: Solid Earth*, 120(6), 4301-4316.

Obermann, A., Planès, T., Hadziioannou, C., & Campillo, M. (2016). Lapse-time-dependent coda-wave depth sensitivity to local velocity perturbations in 3-D heterogeneous elastic media. *Geophysical Journal International*, 207(1), 59–66.

Obermann, A., Planès, T., Larose, E., & Campillo, M. (2013). Imaging preeruptive and coeruptive structural and mechanical changes of a volcano with ambient seismic noise. *Journal of Geophysical Research: Solid Earth*, 118, 6285–6294. https://doi.org/10.1002/2013jb010399

Obermann, A., Planès, T., Larose, E., & Campillo, M. (2018). 4-D Imaging of Subsurface Changes with Coda Waves: Numerical Studies of 3-D Combined Sensitivity Kernels and Applications to the Mw 7.9, 2008 Wenchuan Earthquake. *Pure and Applied Geophysics*. https://doi.org/10.1007/s00024-018-2014-7

Obermann, A., Planès, T., Larose, E., Sens-Schönfelder, C., & Campillo, M. (2013). Depth sensitivity of seismic coda waves to velocity pertur-bations in an elastic heterogeneous medium. *Geophysical Journal International*, 194(1), 372–382. https://doi.org/10.1093/gji/ggt043

Paasschens, J. C. J. (1997). Solution of the time-dependent Boltzmann equation. *Physical Review E*, 56(1), 1135–1141. https://doi.org/10.1103/PhysRevE.56.1135

Pacheco, C., & Snieder, R. (2005). Time-lapse travel time change of multiply scattered acoustic waves. The *Journal of the Acoustical Society of America*, 118(3), 1300–1310. https://doi.org/10.1121/1.2000827

Poupinet, G., Ellsworth, W.L. & Frechet, J. (1984). Monitoring velocity vari- ations in the crust using earthquake doublets: an application to the Calaveras fault, California, *Journal of geophysic Research*, 89(B7), 5719–5731.

Ragnarsson, Á. (2013). *Geothermal energy use, country update for Iceland*. Paper presented at European Geothermal Congress 2013, Pisa, Italy, 11.

Romero, P., & Schimmel, M. (2018). Mapping the basement of the Ebro Basin in Spain with seismic ambient noise autocorrelations. *Journal of Geophysical Research: Solid Earth*, 123. https://doi.org/10.1029/2018JB015498

Roux, P. and Fink, M. (2003). Green's function estimation using secondary sources in a shallow water environment. *The Journal of the Acoustical Society of America*, 113(3), 1406–1416.

Roux, P., Sabra, K. G., Gerstoft, P., Kuperman, W. A., & Fehler, M. C. (2005). P-waves from cross-correlation of seismic noise. *Geophysical Research Letters*, 32(19).

Sánchez-Pastor, P., Obermann, A., & Schimmel, M. (2018). Detecting and locating precursory signals during the 2011 El Hierro, Canary Islands, submarine eruption. *Geophysical Research Letters*, 45. https://doi.org/ 10.1029/2018GL079550

Sato, H. (1993). Energy transportation in one- and two-dimensional scattering media-analytic solutions of the multiple isotropic scattering model. *Geophysical Journal International*, 112(1), 141–146. https://doi.org/10.1111/j.1365-246X.1993.tb01443.x

Schimmel, M. (1999). Phase cross correlations: Design, comparisons, and applications. *Bulletin of the Seismological Society of America*, 89(5), 1366–1378.

Schimmel, M., Stutzmann, E., & Gallart, J. (2011). Using instantaneous phase coherence for signal extraction from ambient noise data at a local to a global scale. *Geophysical Journal International*, 184(1), 494–506. https://doi.org/10.1111/j.1365-246X.2010.04861.x

Schimmel, M., Stutzmann, E., & Ventosa, S. (2018). Low-frequency ambient noise autocorrelations: Waveforms and Normal modes. *Seismological Research Letters*, 89, 1488–1496. https://doi.org/10.1785/0220180027

Sens-Schönfelder, C. & Wegler, U. (2006). Passive image interferometry and seasonal variations of seismic velocities at Merapi Volcano, Indonesia. *Geophysical Research Lett*ers, 33(21), L21302, doi:10.1029/2006GL027797.

Sens-Schönfelder, C. & Wegler, U. (2011). Passive image interferometry for monitoring crustal changes with ambient seismic noise, C. R. *Geosciences*, 343(8), 639–651.

Shang, T., & Gao, L. (1988). Transportation theory of multiple scattering and its application to seismic coda waves of impulsive source. *Scientia Sinica*, 31, 1503–1514.

Shapiro, Nikolai & Campillo, Michel & Stehly, Laurent & Ritzwoller, Michael. (2005). High-Resolution Surface-Wave Tomography from Ambient Seismic Noise. *Science* (New York, N.Y.). 307. 1615-8. 10.1126/science.1108339.

Snieder, R., Grêt, A., Douma, H. & Scales, J. (2002). Coda wave interferometry for estimating nonlinear behaviour in seismic velocity, *Science*, 295(5563), 2253–2255.

Snieder,R. & Safak, E. (2006). Extracting the Building Response Using Seismic Interferometry: Theory and Application to the Millikan Library in Pasadena, California. *Bulletin of the Seismological Society of America*, 96(2), 586–598.

Stähler, S. C., Sens-Schönfelder, C., & Niederleithinger, E. (2011). Monitoring stress changes in a concrete bridge with coda wave interferometry. *The Journal of the Acoustical Society of America*, 129(4), 1945-1952.

Stockwell, R. G., L. Mansinha, and R. P. Lowe (1996). Localization of the complex spectrum: The S transform, IEEE Trans. Signal Processing, 44(4), 998–1001.

Stutzmann, E., Schimmel, M., Patau, G., & Maggi, A. (2009). Global climate imprint on seismic noise. *Geochemistry, Geophysics, Geosystems*, 10(11), https://doi.org/10.1029/2009GC002619

Summers, R., Winkler, K., & Byerlee, J. (1978). Permeability changes during the flow of water through Westerly Granite at temperatures of 100–400 C. *Journal of Geophysical Research: Solid Earth*, 83(B1), 339-344.

Tarantola, A., & Valette, B. (1982). Generalized non-linear inverse problems solved using the least-squares criterion. *Reviews of Geophysics*, 20(2), 219–232.

Tsai, V.C. (2009). On establishing the accuracy of noise tomography traveltime measurements in a realistic medium, *Geophysical Journal International,* 178, 1555– 1564.

Ventosa, S., Simon, C., Schimmel, M., Dañobeitia, J.J. & Manuel, A. (2008). S-transform from a wavelets point of view, *IEEE Transactions on Signal Processing*, 56, 2771–2780.

Weaver, R., Froment, B., & Campillo, M. (2009). On the correlation of non-isotropically distributed ballistic scalar diffuse waves. *The Journal of the Acoustical Society of America*, 126(4), 1817-1826.

Weemstra, C., Obermann, A., Verdel, A., Paap, B., Blanck, H., Guðnason, E. Á., et al. (2016). *Time-lapse seismic imaging of the Reykjanes geothermal reservoir*. In Proceedings of the European Geothermal Congress. Strassbourg: European Geothermal Energy Council (EGEC).

Woolfe, K. F., Lani, S., Sabra, K. G. and Kuperman, W. (2015). Monitoring deep-ocean temperatures using acoustic ambient noise. *Geophysical Research Letters*, 42, 2878–2884.